Seismic Imaging of the Global Asthenosphere Using SS Precursors

Shuyang Sun

Dissertation submitted to the Faculty of the
Virginia Polytechnic Institute and State University
in partial fulfillment of the requirements for the degree of

Doctor of Philosophy
in
Geosciences

Ying Zhou, Chair
Martin Chapman
Sarah Stamps
John Hole

August 22 , 2023
Blacksburg, Virginia

Keywords: Asthenosphere, Low Velocity Zone, Partial Melt, Lithosphere Asthenosphere Boundary (LAB), 220-km Discontinuity, SS Precursors

Seismic Imaging of the Global Asthenosphere Using SS Precursors

Shuyang Sun

(ABSTRACT)

The asthenosphere, a weak layer beneath the rigid lithosphere, plays a fundamental role in the operation of plate tectonics and mantle convection. While this layer is often characterized by low seismic velocity and high seismic attenuation, the global structure of the asthenosphere remains poorly understood. In this dissertation, twelve years of SS precursors reflected off the top and bottom of the asthenosphere, namely, the LAB and the 220-km discontinuity, are processed to investigate the boundaries of the asthenosphere at a global scale. Finite-frequency sensitivities are used in tomography to account for wave diffraction effects that cannot be modeled in global ray-theoretical tomography.

Strong SS precursors reflected off the LAB and the 220-km discontinuity are observed across the global oceans and continents. In oceanic regions, the LAB is characterized by a large velocity drop of about 12.5%, which can be explained by 1.5%-2% partial melt in the oceanic asthenosphere. The depth of the Lithosphere Asthenosphere Boundary is about 120 km, and its average depth is independent of seafloor age. This observation supports the existence of a constant-thickness plate in the global oceans. The base of the asthenosphere is imaged at a depth of about 250 km in both oceanic and continental areas, with a velocity jump of about $\sim 7\%$ across the interface. This finding suggests that the asthenosphere in oceanic and continental regions share the same defining mechanism.

The depth perturbations of the oceanic 220-km discontinuity roughly follow the seafloor age contours. The 220-km topography is smoother beneath slower-spreading seafloors while it becomes rougher beneath faster-spreading seafloors. In addition, the roughness of the 220-km

discontinuity increases rapidly with spreading rate at slow spreading seafloors, whereas the increase in roughness is much slower at fast spreading seafloors. This observation indicates that the thermal and compositional structures of seafloors formed at spreading centers may have a long-lasting impact on asthenospheric convections.

In continental regions, a broad correlation is observed between the 220-km discontinuity depth structure and surface tectonics. For example, the 220-km discontinuity depth is shallower along the southern border of the Eurasian plate as well as the Pacific subduction zones. However, there is no apparent correlation between 3-D seismic wavespeed in the upper mantle and the depths of the 220-km discontinuity, indicating that secular cooling has minimum impact on the base of the asthenosphere.

Seismic Imaging of the Global Asthenosphere Using SS Precursors

Shuyang Sun

(GENERAL AUDIENCE ABSTRACT)

In classic plate tectonic theory, the outermost shell of the Earth consists of a small number of rigid plates (lithosphere) moving horizontally on the mechanically weak asthenosphere. In the classic half space cooling (HSC) model, the lithosphere is formed by gradual cooling of the hot mantle. Therefore, the thickness of the plate depends on the age of the seafloor. The problem with the HSC model is that bathymetry and heat flow measurements at old seafloors do not follow its predicted age dependence. A modified theory, called plate cooling model, can better explain those geophysical observations by assuming additional heat at the base of an oceanic plate with a constant thickness of about 125 km. However, such a constant-thickness plate has not been observed in seismology. In this thesis, the asthenosphere boundaries are imaged using a global dataset of seismic waves reflected off the Earth's internal boundaries. Strong reflections from the top of the asthenosphere are observed across all major oceans. The amplitudes of the SS precursors can be explained by 1.5%-2% of partial melt in the asthenosphere. The average boundary depths are independent of seafloor age, and this observation supports the existence of a constant-thickness plate in the global oceans with a complex origin.

The 220-km discontinuity, also called the Lehmann Discontinuity, was incorporated in the Preliminary Reference Earth Model in the 1980's to represent the base of the asthenosphere. However, the presence and nature of this boundary have remained controversial, particularly in the oceanic regions. In contrast to many studies which suggest the 220-km discontinuity does not exist in the global oceans, SS precursors reflected from this interface are observed

across the oceanic regions in this thesis. Furthermore, there is a positive correlation between the topography of the 220-km discontinuity and seafloor spreading rate. Specifically, the 220-km discontinuity is smoother beneath slower-spreading seafloors and much rougher beneath faster-spreading seafloors. In addition, the roughness increases faster at slower-spreading seafloors while much more gradual at faster-spreading seafloors. This indicates a close connection between seafloor spreading and mantle convections in the asthenosphere, and seafloors have permanent memories of their birth places. Different melting processes at slow and fast spreading centers produce seafloors with different physical and chemical properties, modulating convections in the asthenosphere and ultimately shaping the topography of the 220-km discontinuity.

Reflections from the 220-km discontinuity are also observed across the global continental regions. In addition, the 220-km discontinuity beneath the continents is comparable to that under oceanic regions in terms of their average depth ($\sim$ 250 km) and velocity contrast across the discontinuity ($\sim$ 7%). In continental regions, there is a general connection between the 220-km depth structure and plate tectonics. For example, the boundary is shallower along the southern border of the Eurasian plate from the Mediterranean region to East Asia where mountain belts were formed as a result of collision between the Eurasian plate and the Nubian, Arabian and Indian plates. Depth perturbations of the 220-km discontinuity are also observed along the Pacific subduction zones including the Cascadia Subduction Zone, Peru-Chile Trench and Japan-Kuril Kamchatka Trench. In addition, depth anomalies are mapped in the interior of continents, for example, along the foothills of high topography in the interior of the Eurasian plate, which may be controlled by far-field convection associated with the convergent processes at the plate boundaries.

Acknowledgments

I am deeply grateful and humbled as I approach the completion of this significant PhD journey. This PhD thesis would not have been possible without the invaluable support, guidance, and encouragement from a lot of people. I would like to express my sincere appreciation to all of them for their contributions to my research and personal growth.

First and foremost, I would like to express my deepest gratitude to my advisor, Dr. Ying Zhou, for her constant guidance and mentoring throughout this research endeavor. I have been deeply impressed by her strong background in seismology, geodynamics and mathematics, as well as remarkable capacity for creativity and original thinking. She has tried to afford me all sorts of opportunities to participate in workshops, conferences and expeditions, which have greatly broadened my horizons. She always replies my email within a minute whenever I ask research questions. I am truly fortunate to have had her as my advisor. I am also thankful to the committee members, Dr. Martin Chapman, Dr. John Hole and Dr. Sarah Stamps, for their valuable support and constructive feedback on my research.

Many thanks to Dr. Garrett Apuzen-Ito, Dr. Emilie Hooft and Dr. Yang Shen for offering me an opportunity to attend the research expedition in Galapagos areas and to Dr. Frederik Simons for his support in my academic visit to Princeton University.

I wish to acknowledge to other faculty members Dr. Scott King, Dr. Robert Bodnar, Dr. Megan Duncan, Dr. Steven Holbrook for their informative classes and discussions. I also want to thank staff of Geosciences Department, including April Newcomer, Mary Jane, Mark Lemon, Gary Glesener, Bera Cuskovic, James R. Dunson and Lacie Kmetz for their help and support. I also want to thank my Geosciences colleague Asenath Kwagalakwe, Alexander Ankamah, Sonia Zehsaz, Mohammad Khorrami, Alina Valop, Grant Euen, Tahiry

Rajaonarison, Ali Namayandeh, Shangxin Liu, Josh Murphy, Morrison Nolan, Priyanka Bose, Jessica DePaolis, Lowell Moore, etc. It is truly enjoyable to spend time with them.

I also would like to express my thank to my close friends Jiaxin Liang, Tian Gan, Zhen Guo and Qi Song for their help and care. Finally, I am deeply grateful to my parents and my sister for their unconditional encouragement, support and patience.

Contents

List of Figures xi

1 Introduction 1

Bibliography . . . 3

2 Age-Independent Oceanic Plate Thickness and Asthenosphere Melting from SS Precursor Imaging 5

2.1 Introduction . . . 5

2.2 Data & Methods . . . 7

2.3 Results . . . 12

2.3.1 Large Amplitudes of the LAB *SS* Precursors . . . 12

2.3.2 Depths of the LAB and the 220-km Discontinuity . . . 14

2.4 Discussions . . . 16

2.4.1 Melt Spots in the Oceanic Asthenosphere . . . 16

2.4.2 Age-Independent Thickness of the Oceanic Plate . . . 18

2.5 Conclusions . . . 21

Bibliography . . . 33

3 SS Precursor Imaging Reveals A Global Oceanic Asthenosphere Modu-

lated by Sea-Floor Spreading **42**

3.1 Introduction . . . 42

3.2 Topography of the 220-km Discontinuity . . . 45

3.3 Boundary Roughness and Seafloor Spreading Rate . . . 46

3.4 Seafloor Spreading and Asthenosphere Convection . . . 48

3.5 Conclusions . . . 50

3.6 Data & Methods . . . 51

3.6.1 2-D Finite-Frequency Tomography . . . 54

3.6.2 Amplitudes of SS Precursors . . . 56

Bibliography . . . 64

4 Finite-Frequency Imaging of the 220-km Discontinuity beneath the Global Continents **69**

4.1 Introduction . . . 69

4.2 Data and Methods . . . 71

4.2.1 Identification of Phase Interference Using Finite-Frequency Sensitivities 72

4.2.2 Finite Frequency Tomography . . . 73

4.3 Results . . . 76

4.3.1 Finite-frequency Tomography of the Continental 220 . . . 76

4.3.2 Global Tomography (Oceans and Continents) . . . 77

4.3.3 $S_{220}S$ Amplitude Measurements . . . 78

4.4 Discussions 79

4.4.1 Global Presence of the 220-km Discontinuity 79

4.4.2 Correlation between the 220-km Discontinuity and Surface Tectonics 80

4.4.3 The Absence of $S_{220}S$ on Global Stacks 81

4.5 Conclusions 82

Bibliography 97

Appendices **105**

Appendix A Supplementary Figures Used in Chapter 2 **106**

Appendix B Supplementary Figures Used in Chapter 3 **122**

Appendix C Supplementary Figures Used in Chapter 4 **136**

List of Figures

2.1 (a) example transverse-component seismograms with large-amplitude $S_{\mathrm{LAB}}S$ and $S_{220}S$ phases. The black seismograms are data, the red seismograms are synthetics calculated in a reference 1-D model (Model I) with 12.5% of the velocity jump across the LAB, and the blue synthetics are calculated in PREM in which there is no discontinuity at the LAB depth. The reference models are plotted in Figure 2.3. The seismograms have been band-pass filtered between 10 and 80 mHz and aligned using their SS arrivals for better illustration. The precursor closest to the main SS wave is labeled as $S_{\mathrm{LAB}}S$ as we investigate possible reflections from the top of the asthenosphere. The arrivals of the $S_{220}S$, $S_{410}S$ and $S_{660}S$ waves are also labeled. The earthquake event date/time and station name as well as depth and epicentral distance are denoted on each seismogram. The corresponding geographic ray paths (black lines) and bounce points (red circles) of the $S_{\mathrm{LAB}}S$ waves are plotted in (b). Ray paths and bounce points of the 1,380 $S_{\mathrm{LAB}}S$ waves with anomalously large amplitudes are plotted in (c). Seafloor age contours are plotted at 20, 60, 100 and 140 Ma. 23

2.2 Geographic distribution of subsets of the data plotted at SS bounce points. (a) clear $S_{\mathrm{LAB}}S$ observed, (b) clear $S_{220}S$ observed, (c) $S_{\mathrm{LAB}}S$ observed but not $S_{220}S$, (d) $S_{220}S$ observed but not $S_{\mathrm{LAB}}S$, (e) both $S_{\mathrm{LAB}}S$ and $S_{220}S$ observed, (f) no $S_{\mathrm{LAB}}S$ or $S_{220}S$ observed. There is no apparent geographic pattern associated with either the presence or absence of the $S_{\mathrm{LAB}}S$ and $S_{220}S$. 24

2.3 (a) Three 1-D reference earth models Model I, Model II and Model III used in this study and their corresponding example synthetic seismograms are plotted in (b). Model PREM is also plotted in (a) for reference. The synthetic seismograms are calculated using the three reference models for a magnitude 6.9 Indonesia earthquake occurred in August 2018 recorded at a GSN station SDDR (https://doi.org/10.7914/SN/CU). The observed seismogram is plotted in Figure 2.1. The seismograms have been band-pass filtered between 10 and 80 mHz and have been aligned using the main SS wave arrivals for better illustration. The velocity contrast across the LAB at a depth of 130 km is 12.5% in Model I, 6% in Model II and 11% in Model III. The corresponding $S_{\mathrm{LAB}}S$ wave amplitude in Model I is much larger than that in Model II and slightly larger than that in Model III, as expected. 25

2.4 (a) shows example measurement windows used for LAB amplitude ratio measurements $A_{S_{\mathrm{LAB}}S}/A_{S_{410}S}$ and $A_{S_{\mathrm{LAB}}S}/A_{S_{660}S}$. The seismograms are for a magnitude 6.6 Mexico earthquake occurred in January 2016 recorded at a GSN station MSEY (https://doi.org/10.7914/SN/II), and the epicentral distance is 158°. The synthetic seismogram is calculated for Model I as in Figure 2.3 and both seismograms have been band-pass filtered between 10 and 80 mHz. (b) and (c) are finite-frequency traveltime boundary sensitivity kernels for the $S_{\mathrm{LAB}}S$ and $S_{220}S$ waves, respectively. The sensitivity kernels are plotted in map view in the ray coordinates, centered at the bounce point which is about 79° away from the source and the receiver. 26

2.5 Synthetic amplitude measurement experiment using the same 40-second time window as applied in data. (a) The black seismogram is the LAB phase from the observed seismogram in Figure 2.4, and we multiply the seismogram by a constant factor of two (frequency-independent) to obtain the red seismogram. (b) Theoretical amplitude spectral ratio (black line) and measurements made at periods of 15, 20, 25, 30 and 35 seconds (circles). (c) The black seismogram is the same as in (a) and the red seismogram is obtained by multiplying the amplitude spectrum of the black seismogram with a frequency-dependent function. The corresponding theoretical amplitude ratios and measurements made at 15, 20, 25, 30 and 35 seconds period are plotted in (d). The experiment confirms that amplitude ratios at the measurement frequency (25 seconds) can be determined using a 40-second time window. 27

2.6 $S_{\rm LAB}S$ amplitude measurements γ= minimum [log ($A_{S_{\rm LAB}S}$ /$A_{S_{410}S}$), log ($A_{S_{\rm LAB}S}$ /$A_{S_{660}S}$)] obtained using observed seismograms (top) as well as synthetic seismograms calculated for three reference models (Model I, II and III) plotted at the bounce points in mapviews and histograms. The observed $S_{\rm LAB}S$ amplitudes show a similar distribution (histogram) to the amplitude ratios calculated for Model I (12.5% velocity drop across the LAB). The amplitude ratios calculated in Model II (6% velocity drop across the LAB) are overall much smaller than the observations, and the amplitude ratios calculated in Model III (11% velocity drop across the LAB) are slightly smaller than the observed amplitude ratios. We conclude that the observed large amplitude of the $S_{\rm LAB}S$ waves can be explained by 12.5% of velocity drop across the LAB. 28

2.7 (a) and (b) are $S_{\mathrm{LAB}}S$ traveltime measurements plotted in histograms and mapviews at their bounce points. The measurements are made with respect to Model I synthetic seismograms. 3-D mantle wavespeed and crustal corrections have been applied. (c) and (d) are the same as (a) and (b) but for $S_{220}S$. . 29

2.8 (a) and (b) are the depths of the LAB calculated from traveltime measurements, plotted in histogram and mapview at $S_{\mathrm{LAB}}S$ bounce points. (c) and (d) are the depths of the 220-km discontinuity. (e) and (f) are the asthenosphere thicknesses calculated from the depths of the LAB and the 220. 30

2.9 **Age-independent thickness of the oceanic plate.** Green circles and red diamonds are depths of the LAB and the 220-km discontinuity obtained from this study, plotted as a function of the seafloor age. Isotherms at an interval of 200°C (starting at 300°C) from the half space cooling model (dashed line) and the plate model (solid line) are plotted for reference. The observed depths of the two discontinuities show significant local variations. The average depths of the LAB and the 220-km discontinuity are at 120 km and 255 km, independent of seafloor age. The depth uncertainties estimated from frequency-dependent measurements are plotted as error bars. 31

2.10 (a) Synthetic seismograms calculate for Model I and Model IV as in Figure 2.3. (b) Q structure in the 1-D reference models Model I and Model IV. Model IV is identical to Model I in velocity and density but has a much smaller Q value (Q=20) in the asthenosphere than in Model I (Q=80). The amplitude of the main SS wave becomes smaller in Model IV synthetics due to the overall stronger attenuation associated with the lower Q value in the asthenosphere but its impact on the amplitude of the SS precursor $S_{\rm LAB}S$ is very limited. This is because anelasticity also reduces the effective wave speed in the low Q region. Therefore, velocity contrast across the LAB increases, resulting a larger reflection coefficient which increases the amplitude of the $S_{\rm LAB}S$ wave. The observed large amplitudes of the $S_{\rm LAB}S$ waves therefore can not be fully explained by a reduction of Q values in the asthenosphere. 32

3.1 **(a)** geographic ray paths (gray lines) and bounce points (orange dots) of the SS precursors ($S_{220}S$) used in this study. **(b)** bounce points and ray paths for example seismograms plotted in **(c)**. **(c)** example transverse-component seismograms with $S_{220}S$ phases. The epicentral distance ranges from 80° to 180°. The black seismograms are data, the red seismograms are synthetics calculated in a reference 1-D model MOCE with 7% of the velocity jump across the 220-km discontinuity, and the blue synthetics are calculated in PREM in which the velocity increases is 5% across the discontinuity. Model MOCE and PREM are plotted in Figure 3.2. The seismograms have been band-pass filtered between 10 and 80 mHz and aligned using their SS arrivals for better illustration. The arrivals of the $S_{410}S$ and $S_{660}S$ waves are also labeled for reference. Station name, earthquake event date/time, depth and epicentral distance are denoted. Seafloor age contours (10, 50, 90, 130 and 170 Ma) in dashed black lines. 58

3.2 **(a)** S-wave speed profiles in model MOCE (solid black line) and model PREM (dotted black line). There is $\sim$ 5% velocity increase across the 220-km discontinuity in mode PREM. Model MOCE is revised from PREM model and it incorporates two discontinuities at 250 km and 130 km with velocity contrasts of 7% and 12%, respectively, to represent the 220-km discontinuity and the lithosphere asthenosphere boundary (LAB), respectively. **(b)** and **(c)** are $\delta t|_{S_{220}S} - \delta t|_{SS}$ traveltimes of the 2754 data calculated for model MOCE after crustal and mantle corrections plotted in mapview and histogram. Seafloor age contours are plotted in dash, black lines at 10, 50, 90, 130 and 170 Ma. **(d)** and **(e)** are the same with **(b)** and **(c)**, respectively, but for model PREM. The average of $\delta t|_{S_{220}S} - \delta t|_{SS}$ traveltimes in model MOCE is close to 0, while that in model PREM is $\sim$ -5 seconds. 59

3.3 **Amplitude measurements of $S_{220}S$ waves. (a)**, amplitude measurements of 2754 sets of observed $S_{220}S$ waves in data calculated as γ= minimum [log $(A_{S_{\rm LAB}S} / A_{S_{410}S})$, log$(A_{S_{\rm LAB}S} / A_{S_{660}S})$] plotted in mapview (top) and histogram (bottom), respectively. **(b)** and **(c)**, the same with **(a)** but for model MOCE and model PREM, respectively. The mean amplitudes of observed $S_{220}S$ waves are roughly consistent with that of the synthetic $S_{220}S$ waves in model MOCE, both of which are larger than that in model PREM. 60

3.4 **(No) correlation between the 220-km discontinuity depth and seafloor spreading rate or seafloor age. (a)**, depth of the 220-km discontinuity in oceanic regions **(b)**, depth of the 220-km discontinuity in oceanic regions with large resolution (> 0.25). **(c)** and **(d)**, seafloor spreading rate and seafloor age, respectively, in oceanic regions with large resolution (> 0.25). **(e)**, scatter plot of maximum depth of the 220-km discontinuity with respect to the seafloor spreading rate in $5^\circ \times 5^\circ$ degree cells in global oceans (Pacific Ocean in orange, Atlantic Ocean in red and Indian Ocean in purple). The earth surface is divided into certain 5° (longitude) $\times$ 5° (latitude) areas in **(b)** and then the maximum 220-km depth in each area are extracted, which are then plotted against the spreading rate at the center of the $5^\circ \times 5^\circ$ areas. Mean (maximum) depth of the 220-km discontinuity is plotted on the top in gray dots with one standard deviation. The mean (maximum) depth is obtained by averaging the maximum depth at seafloor spreading rate ranges of every 10 $mm/year$. The 220-km depth remains roughly constant at different seafloor spreading rates. **(f)**, same with **(e)** but for the scatterplots of the depth of the 220-km discontinuity against seafloor age. The 220-km depth remains roughly constant at different seafloor ages. 61

3.5 **Correlation between the 220-km discontinuity roughness and seafloor spreading rate.** **(a)**, roughness of the 220-km discontinuity in oceanic regions **(b)**, roughness of the 220-km discontinuity in oceanic regions with large resolution (> 0.25). **(c)**, scatter plot of maximum roughness of the 220-km discontinuity with respect to the seafloor spreading rate in $5^\circ \times 5^\circ$ degree cells in global oceans (Pacific Ocean in orange, Atlantic Ocean in red and Indian Ocean in purple). **(d)**, scatter plot of mean (maximum) roughness of the 220-km discontinuity against the seafloor spreading rate. The 220-km roughness generally increases with seafloor spreading rate in the global oceans. In addition, the roughness increases rapidly with spreading rate at slow-spreading seafloors while it increases slowly with spreading rate at fast-spreading seafloors. **(e)** and **(f)**, same with **(c)** and **(d)**, respectively, but for the scatterplots of the roughness of the 220-km discontinuity against seafloor age. There exists a weak positive correlation between the 220 roughness and seafloor age in global oceans. 62

3.6 **(a)** and **(b)**, roughness of the 220-km discontinuity in oceanic regions with spreading rate $<= 40$ $mm/year$ and spreading rate > 40 $mm/year$, respectively. **(c)** and **(d)** are same with **(a)** and **(b)**, respectively, but only for oceanic regions with large resolution (> 0.25). **(e)**, roughness of the 220-km discontinuity in Atlantic Ocean with spreading rate $<= 40$ $mm/year$ and large resolution (> 0.25). **(f)**, spreading rate ($<= 40$ $mm/year$) in the Atlantic Ocean with large resolution (> 0.25). 63

4.1 (a) distribution of 524 earthquakes used in the global dataset, with strong SS waves observed on 8,087 seismograms. The bouncepoints of the SS waves are all located in continental regions. The 487 red stars are events from which clear $S_{220}S$ waves are observed and the 37 blue stars are events from which no clear $S_{220}S$ waves are observed. (b) distribution of 145 GSN stations where clear SS waves are observed, with $S_{220}S$ waves also observed on 142 of the stations (red triangles). (c) gray histograms are the focal depths of all 524 earthquake events. Black histograms are focal depths of the 487 events with clear $S_{220}S$ waves. (d) epicentral distances of the corresponding earthquakes in (c). 84

4.2 **(a)** bouncepoints of the $S_{220}S$ waves in the global continental dataset, plotted on top of their ray paths (grey lines). The dataset provides a good coverage across all continental regions. **(b)** bounce points and geographic ray paths of 16 example seismograms plotted in **(c)**. **(c)** example transverse-component seismograms with clear $S_{220}S$ phases including data (black) and synthetics calculated in reference 1-D models MREF (red) and PREM (blue). The velocity jumps across the 220-km discontinuity in MREF and PREM are 7% and 5%, respectively. SS waves have been aligned and some of the polarities are reversed for illustration only. The $S_{410}S$ and $S_{660}S$ waves arrivals are also labeled. The seismograms have been band-pass filtered between 10 and 80 mHz. The earthquake event date, station name, focal depth and epicentral distance are denoted on each set of seismograms. The epicentral distances of these example seismograms range between 96° and 119° and the focal depths are all shallower than 35 km. Theoretically, $S_{220}S$ waves are not interfered by other phases including topside reflections (e.g., $S_{660}sS$ and $S_{660}sS_{diff}$), ScS reverberations (e.g., $S_{670}ScS_{670}S$ and $S_{410}ScS_{410}S$) as well as depth phases (sSS waves). 85

4.3 **(a)** S-wave speed in model MREF (solid black line) and model PREM (dashed black line). The velocity increase across the 220-km discontinuity in model PREM is 5%. Model MREF is revised from model PREM and it incorporates two discontinuities at 130 km and 250 km depths, to represent the lithosphere asthenosphere boundary (LAB) and the 220-km discontinuity, respectively, with the velocity contrasts of 12% and 7%. **(b)** $\delta t|_{S_{220}S} - \delta t|_{SS}$ traveltime measurements after crustal and mantle corrections. The global dataset includes 3,422 measurements with SS wave bouncepoints located in the global continental regions (black outlines) as well as 2,754 measurements with bouncepoints in the global oceanic regions from the study of Sun & Zhou (in submission). **(c)** histograms of traveltime measurements including the 3,422 continental measurements (red filling) and 2,754 oceanic data (black, dashed outlines). **(d)** same as **(c)** but for traveltimes without crustal and mantle corrections. The mean traveltime of the continental $\delta t|_{S_{220}S} - \delta t|_{SS}$ measurements after and before corrections are -5.2 seconds and -5.1 seconds, respectively. The mean oceanic measurements after and before corrections are -4.5 seconds and -5.3 seconds. 86

4.4 **(a)** depth perturbations of the 220-km discontinuity obtained from finite-frequency inversion of the continental data (Fig. 3). The resolution of the model is plotted in **(b)**. **(c)** and **(d)** are shear wavespeed perturbations from model S40RTS at 200 km and 250 km depths, respectively. **(e)** and **(f)** are gravity anomalies [61] and topography [62] in continental regions, respectively. 87

4.5 Depth perturbations of the 220-km discontinuity in continental regions obtained from finite-frequency inversion using only the continental data in **(a)** and joint inversion of both oceanic and continental data in **(b)**. Only structures in the continental regions are plotted for comparison. **(c)** and **(d)** are the model resolutions of **(a)** and **(b)**, respectively. 88

4.6 (a) histograms of the 220-km discontinuity depth in continental (red filling) and oceanic regions (dashed, black outlines). The 220-km discontinuity depth in continental and oceanic regions are inverted independently. (b) same as (a) but for depths from joint global inversion of both the oceanic and continental data. The average continental 220-km discontinuity depth is about 251 km, which is close to the average depth of the oceanic 220-km discontinuity in both independent and joint inversions. 89

4.7 (a) and (b) are the 220-km discontinuity depth perturbations in oceanic and continental regions, respectively, obtained from joint inversion of both the continental and the oceanic data. 90

4.8 **(a)** is same as Fig. 3b but for $\delta t|_{S_{220}S} - \delta t|_{SS}$ traveltimes without crustal and mantle corrections. **(b)** same as Fig. 7, but for depth perturbation of the 220-km discontinuity without corrections. 91

4.9 **(No) correlation between S wavespeed perturbations and the 220-km discontinuity depth perturbations. (a)** (weak) correlation between S wavespeed perturbations and the 220-km depth perturbations. The average S-wave speed perturbations are calculated from model S40RTS, averaged between perturbations in the upper mantle from 100 to 300 km depth. **(b)** same as **(a)** but for the mean discontinuity depth perturbations averaged over regions with the same S-wave speed perturbations. **(c)** and **(d)** are same as **(a)** and **(b)** but for the 220-km discontinuity depth perturbations obtained without crustal and mantle wavespeed corrections. There is no apparent correlations between S wavespeed perturbations in the upper mantle and the depths of the 220-km discontinuity. 92

4.10 **Amplitude measurements of $S_{220}S$ waves.** Panel **(a)**, amplitude measurements γ = minimum [$\log(A_{S_{\rm LAB}S}/A_{S_{410}S})$, $\log(A_{S_{\rm LAB}S}/A_{S_{660}S})$] plotted in mapview (top) and histogram (bottom), respectively. In the top mapview, amplitude measurements of the continental data are plotted with black outlines while the oceanic measurements are plotted with gray outlines. In the bottom histograms, amplitude measurements of the continental data are plotted in red while the oceanic data are plotted as back, dashed lines. **(b)** and **(c)** are same as **(a)** but for synthetic SS precursors in model MREF and PREM, respectively. The mean amplitudes of the observed $S_{220}S$ waves in **(a)** are close to the MREF synthetics in **(b)** while PREM synthetics underpredict the amplitudes of the observed $S_{220}S$ waves. 93

4.11 (a) stacks of observed (left) and synthetic (right) seismograms with SS bounce points in continental regions. The synthetic seismograms are calculated in model MREF. Seismograms in every 10-degree epicentral distance intervals in the global dataset are included to build the stacks. The bottom panel is the same but for the stacks using oceanic data. Unlike the $S_{410}S$ and the $S_{660}S$ waves, the $S_{220}S$ phase is weak or absent on the majority of the global stacks. 94

4.12 Example regional stacks in which strong $S_{220}S$ waves are observed on the stacked seismograms. Panel (a) shows example geographic stacks at grid points shown in (b) where standard deviations of the 220-km discontinuity depth are small. Observed and synthetic seismograms within a 10° circle distance around each grid points have been used to calculate the observed (left) and synthetic (right) stacks, respectively. (b) shows the location of the grid points plotted on top of the standard deviations of the 220-km discontinuity depths obtained from finite frequency tomography. 95

4.13 Similar to Figure 10, but for weak stacks in regions where large 220-km depth variations are observed. Panel (a) shows example stacks of observed and synthetic seismograms, respectively. (b) locations of the grid points where stacks are calculated. These grid points are located in regions with large lateral depth variations in the 220-km discontinuity. 96

A.1 (a) and (b) are distributions of the 543 earthquakes and 151 GSN stations used in this study. (c) and (d) are distributions of the 395 earthquakes and 144 GSN stations in the subset in which large $S_{\mathrm{LAB}}S$ waves were observed. (e) and (f) are histograms of the focal depths and epicentral distances of the same subset. 107

A.2 Example SS seismograms with simple source time functions recorded at a GSN station DWPF (https://doi.org/10.7914/SN/IU) for earthquakes with different magnitudes ranging from 6.5 to 7.9. The event magnitude, date/time, depth and epicentral distance are denoted. The SS waves have been aligned with polarities corrected for better illustration. The dataset used in this study includes 6,143 high-quality SS seismograms with bounce points in oceanic regions. 108

A.3 (a) and (b) are example seismograms with SS waves significantly different from the synthetics. SS precursors on those seismograms are not used in this study. (c) example seismograms with noisy SS waves and precursors, SS precursors on those seismograms are not used in this study. (d) example seismograms with clear SS precursors but weak (or absent) $S_{\mathrm{LAB}}S$ waves, their bounce points are plotted in Figure 2.2. 109

A.4 1-D reference earth models used in this study: PREM, Models I, II, III and IV. (a) S-wave speed profiles. The velocity contrast across the LAB is 12.5% in Model I, 6% in Model II and 11% in Model III. (b) density profiles of the models. The density is scaled with velocity in the uppermost 250 km in Models I-IV , with a scaling parameter of $\sim$0.77, similar to that in PREM, which varies between 0.75 and 0.78. (c) Seismic Q profiles of the models. $Q = 80$ in Model I at depths between 130 and 250 km and $Q = 20$ in Model IV at those depths. PREM Q values are plotted as the dashed line for reference. 110

A.5 (a) example seismograms with (top) and without (bottom) an interfering depth phase. The measurement windows (shaded) are centered at the expected arrival of the $S_{220}S$ waves. The epicentral distance is 96° and the depths of the earthquakes are denoted on each seismogram. The SS waves have been aligned and a strong depth phase sSS arrives after the main SS wave for the deep earthquake (depth=160 km). The precursor of the depth phase $sS_{410}S$ arrives about the same time as the the SS precursor $S_{220}S$. The calculated sensitivity kernel is abnormal when there is $sS_{410}S$ interference – the sensitivity is about 10 times smaller than values expected for an $S_{220}S$ wave. This is because the $sS_{410}S$ wave is not reflected at the 220-km discontinuity and therefore it has no sensitivity to depth perturbations of the 220-km discontinuity at the bounce point. 111

A.6 Example traveltime sensitivity kernels with (top) and without (bottom) phase interference. (a) and (c) are synthetic seismograms with measurement windows (shaded) centered at the expected arrival of the $S_{\rm LAB}S$ waves, and (b) and (d) are the corresponding traveltime sensitivity kernels. (c) and (d) are the same as in Figure 2.4 (a) and (b). The interferences between the $S_{\rm LAB}S$ and $sScS$ coda waves (shallow multiples) in the measurement window in (a) result in a polarity change in the traveltime sensitivity in (b). The sensitivity kernels are always associated with measurement time windows not any particular seismic phases, and the kernels are used to identify possible phase interferences in measurement windows. 112

A.7 (a) histogram of amplitude ratios between the observed and the synthetic SS waves for the entire dataset (6143 seismograms). (b) the same as (a) but for the subset (1380 seismograms) in which anomalously large $S_{\rm LAB}S$ were observed. The distribution of the SS amplitude measurements is very similar in (a) and (b), indicating that the observed large amplitudes of the $S_{\rm LAB}S$ waves in the subset are not a result of focusing caused by mantle heterogeneities because the focusing effects (anomalously large amplitudes) are not observed on the SS waves which travel through the same regions in the mantle sampled by the $S_{\rm LAB}S$ waves. 113

A.8 Scatter plots of the LAB amplitude measurements made in the frequency domain versus those obtained in the time domain using envelope functions of the observed seismograms. (b) is the same as (a) but for measurements made on synthetic seismograms calculated for Model I. It is worth noting that the frequency-domain measurements are made at a period of 25 seconds while the envelope functions include much broader frequency content. In this paper, we focus on measurements at a period of 25 seconds, and the envelope function results are plotted for reference only. The 45° line with a slope of 1.0 is also plotted for reference only, it is not expected to be the best fitting line for the scatter plots. 114

A.9 The same as Figure 2.7 but for traveltime measurements made without 3-D crustal and mantle corrections. 115

A.10 The same as Figure 2.8 but for depths of the LAB and the 220-km discontinuity obtained using traveltime measurements without 3-D crust and mantle corrections. 116

A.11 The same as Figure 2.9 but for depths of the LAB and the 220-km discontinuity obtained using traveltime measurements without 3-D crust and mantle corrections. 117

A.12 (a), example radial-component seismograms with large-amplitude SS precursors. The corresponding geographic ray paths are plotted in (b). 118

A.13 (a) velocity models with a 12.5% of velocity change across the LAB at a depth of 130 km over a first-order discontinuity (Model I) as well as a gradient zone of 5 km, 10 km and 20 km. (b), (c), (d) and (e) are the corresponding histograms of the amplitude measurements γ= minimum [log ($A_{S_{\rm LAB}S}$ /$A_{S_{410}S}$), log($A_{S_{\rm LAB}S}$ /$A_{S_{660}S}$)] made on the synthetic seismograms calculated for the four reference models as in Figure 2.6. The $S_{\rm LAB}S$ amplitudes become smaller when the velocity change occurs over a gradient zone. The average amplitude difference between a first-order discontinuity and a 5-km gradient zone for this dataset is about 2%, and it is about 6% if the velocity change occurs over a 10-km gradient zone. For a gradient zone over a depth range of 20 km, the mean $S_{\rm LAB}S$ amplitude is about 17% smaller than that for a first-order discontinuity, and the overall amplitude distribution also becomes significantly different. The calculations suggest that a 12.5% velocity change over a gradient zone of 5 km or less can explain the observed amplitude data in Figure 2.6. 119

A.14 (a) standard deviation at different length scales calculated for the LAB depths obtained in this study. The LAB depths are plotted in histogram and mapview in Figure 2.8 (a) and (b). The average standard deviations of the LAB depth are calculated for moving square cells over the global surface, plotted as a function of the length of the cell. The center of the cell moves at a one degree interval in latitude and longitude directions. Only cells that contain more than 30 data points are used in the calculation. (b) same as (a) but calculated for moving cells that are not overlapping. 120

A.15 A simple example illustrating the concept the large amplitudes of SS precursors may not be picked up in stacking results when large variations in SS precursor amplitudes and arrival times are present. The black seismograms are observed data with close epicentral distances between 129° and 130°. In a 1-D earth model, the SS precursors arrive at about the same time when the SS waves are aligned (with arrival time differences less than 0.2 seconds). We align the SS waves and produce a stack using only the top seven seismograms (blue) and a second stack using all ten seismograms (red). The SS precursors on the two stacked seismograms are significantly different. 121

B.1 (a) distribution of the bouncepoints of all 32,369 sets of SS data (orange dots) in the global oceans. Seafloor age countours are plotted in dash, black lines at 10, 50, 90, 130 and 170 Ma. (b) distribution of 6506 sets of data (orange dots) with good SS waves. (c) distribution of 2754 sets of data (orange dots) with good $S_{220}S$ waves plotted on top of the traveling paths (grey lines), same with Figure 3.1(a). The data set has a good coverage on all oceanic regions. (d) distribution of 459 earthquakes (gray stars) and 144 stations (orange triangles) for the 2754 sets of good $S_{220}S$ data used in this study. 123

B.2 **1-D reference earth model MOCE used in this study.** (a), S-wave speed profiles in model MOCE (solid black line) and model PREM (dotted black line). The velocity contrasts across the 220-km discontinuity and the LAB are 7% and 12%, respectively, in model MOCE. (b), density profiles of model MOCE and model PREM. (c), seismic Q profiles of model MOCE and model PREM. 124

B.3 (a) and (b), similar to Figure 3.2b and 3.2c, respectively, but are $\delta t|_{S_{220}S} - \delta t|_{SS}$ traveltimes of the 2754 data calculated for model MOCE before crustal and mantle wavespeed corrections plotted in mapview and histogram. (c) and (d), similar to Figure 3.2d and 3.2e, respectively, but are $\delta t|_{S_{220}S} - \delta t|_{SS}$ traveltimes of the 2754 data calculated for model PREM before crustal and mantle corrections. (e), similar to Figure 3.4a, but is 220-km depth before crustal and mantle corrections. (f), similar to Figure 3.5a, but is 220-km roughness before crustal and mantle wavespeed corrections. 125

B.4 **a**, example traveltime measurement of $\delta t|_{S_{220}S} - \delta t|_{SS}$ and the SS waves have been aligned. The shaded area indicates the measurement window of $\delta t|_{S_{220}S} - \delta t|_{SS}$. The observed seismogram was recorded at a GSN station CPUP (https://doi.org/10.7914/SN/GT) for a magnitude 6.8 earthquake in Japan in October 2009. The seismograms have been band-pass filtered between 10 and 80 mHz. The seismic event data/time, station, depth and epicentral distance is denoted above. **b**, finite-frequency traveltime boundary sensitivity kernel for the shaded measurement window in **a**. 126

B.5 (a), trade-off curve of TSVD solution to the inverse problem $\boldsymbol{Ax} = \boldsymbol{b}$ truncated to varying parameters k. The horizontal axis is $\|\boldsymbol{x}\|$ and the vertical axis is $\|\boldsymbol{A}^T\boldsymbol{Ax} - \boldsymbol{A}^T\boldsymbol{b}\|$. The optimal Model A plotted in (b) is obtained by using truncation parameter of 500, which is indicated by the star. TSVD solutions truncated to 100, 300, 700 and 900 are denoted by the black dots from left to right on the curve. Models truncated to 300 and 700 are labelled as Models B (c) and C (d), respectively. Insufficient eigenvectors are used in Model B which could not fully recover the 220-km depth structure, while excess eigenvectors are used in Model C which contains additional noise. Model A calculated using 500 eigenvectors best represents the depth structure of the 220-km discontinuity in the global oceans. 127

B.6 **Correlation of 220-km depth filtered at different length scales with respect to seafloor spreading rate and seafloor age.** In top row, the left figure shows the 220-km depth filtered at degrees of 0-5. The middle figure, similar to Figure 4.4e, is the scatter plot of 220-km depth with respect to the seafloor spreading rate in all oceans (Pacific Ocean in orange, Atlantic Ocean in red and Indian Ocean in purple). Mean 220-km depth is plotted on the top in gray dots with one standard deviation. The right figure, similar to Figure 4.4f, is the scatter plot of 220-km depth and mean 220-km depth against the seafloor age in all oceans. The second, third and fourth rows are the same but for 220-km depth filtered at degrees of 0-15, 0-30 and 0-40, respectively. The 220-km depth at all length scales remains roughly constant at different seafloor spreading rates and seafloor ages. 128

B.7 (a), 220-km depth model in global oceans. (b), resolution of the 220-km depth model (a). The 220-km depth is well recovered in regions where the resolution is large. (c), 220-km depth model with resolution > 0.1. (c), 220-km depth model with resolution > 0.25. 129

B.8 (a), 220-km roughness in the Atlantic Ocean with spreading rate <= 40 mm/year and resolution > 0.1. (b) spreading rate <= 40 mm/year in the Atlantic Ocean with resolution > 0.1. There is a strong correlation between the 220-km roughness and spreading rate in the Atlantic Ocean. Specifically, roughness is generally small in North Atlantic where spreading rate is slow in general. In the middle Atlantic, roughness becomes large and the spreading rate turns fast. 130

B.9 **Correlation between 220-km roughness filtered at different length scales and seafloor spreading rate.** In top row, the left figure shows the 220-km roughness filtered at degrees of 0-5. The middle figure is the scatter plot of maximum 220-km roughness with respect to the seafloor spreading rate in $5^\circ \times 5^\circ$ degree cells in all oceans (Pacific Ocean in orange, Atlantic Ocean in red and Indian Ocean in purple), similar to Figure 5.5c. The right figure presents the scatter plot of mean (maximum) 220-km roughness against the seafloor spreading rate, similar to Figure 5.5d. The second, third, and fourth rows are the same but for 220-km roughness filtered at degrees of 0-15, 0-30 and 0-40, respectively. The positive correlation between 220-km roughness and seafloor spreading rate holds at different length scales. 131

B.10 **Correlation between seafloor spreading rate and seafloor age.** (a), seafloor spreading rate in oceanic regions with large resolution (> 0.25). (b), seafloor age in oceanic regions with large resolution (> 0.25). (c) and (d), scatter plot of maximum and mean (maximum) seafloor spreading rate with respect to the seafloor age in $5^\circ \times 5^\circ$ degree cells in global oceans. The mean (maximum) seafloor spreading rate is obtained by averaging the maximum seafloor spreading rate at seafloor age ranges of every 10 Ma. The seafloor spreading rate generally remains constant at different seafloor ages except at 120 - 150 Ma at which there are abnormally fast rates. This sharp increase in rate may reflect potential timescale miscalibration. 132

B.11 **Stacking of observed seismograms shows weak 220-km signal.** **a** and **b**, example observed and synthetic seismograms with epicentral distance of 124-125 degrees. The synthetic seismograms are calculated in the reference model MOCE. The event date/time, station and depth are denoted above. 10 observed seismograms where clear 220-km waves can be observed in **a**. But they present large variations in arrival time and polarities. The corresponding synthetic seismograms calculated using Model MOCE are in **b**. **c**, stacking result of the observed seismograms in **a** (top, red seismogram) and the synthetic seismograms in **b** (bottom, black seismogram). The main SS waves are aligned and the polarities are corrected to be the same.The arrivals of SS precursors are labeled. 133

B.12 Example traveltime sensitivity kernels of $S_{220}S$ with and without phase interference of $S_{660}sS$. (a) SS wavefield at epicentral distance 80° - 120° for a earthquake event source of 0 km. The SS waves are aligned. The arrivals of the SS precursors $S_{660}S$, $S_{410}S$ and $S_{220}S$ as well as two large-amplitude phases $S410sS$ and $S660sS$ are labeled. $S660sS$ wave strongly interfere with $S_{220}S$ when epicentral distance is smaller than $\sim$ 90°. (b) and (c) are the zoom in views of the seismogram at 115° and 82°, respectively , from (a). The kernel measurement windows (shaded) are centered at the expected arrival of the $S_{220}S$ waves. There is no phase interference for $S_{220}S$ wave at epicentral distance of 115° while a strong $S660sS$ wave arrives about the same time as the $S_{220}S$ wave at 82°. As a result, the calculated sensitivity kernel values under the impact of $S660sS$ wave for 82° (e) are abnormal which are an order of magnitude smaller than that for 115° (d). The strong $S660sS$ wave is dominating in the expected arrival time window of $S_{220}S$. This phase is not reflected at the 220-km discontinuity and therefore it has no sensitivity to depth perturbations of the 220-km discontinuity at the reflection point. . 134

B.13 **Amplitude measurements of $S_{LAB}S$ waves.** Similar to Figure 3.3, but for the amplitude measurements of 1021 sets of $S_{LAB}S$ waves in data, model MOCE and model PREM calculated as γ= minimum [log ($A_{S_{\rm LAB}S}$ /$A_{S_{410}S}$), log($A_{S_{\rm LAB}S}$ /$A_{S_{660}S}$)] plotted in mapviews and histograms. 135

C.1 (a) trade-off curve of finite-frequency tomography using continental $S_{220}S$ measurements only. The horizontal axis is model norm $\|\boldsymbol{m}\|$ and the vertical axis is data misfit $\|\boldsymbol{G}^T\boldsymbol{G}\boldsymbol{m} - \boldsymbol{G}^T\boldsymbol{d}\|$. Dots are models obtained using different regularization parameter N and the red star denotes the optimal solution. (b) trade-off curve of finite-frequency global tomography using both the continental and oceanic $S_{220}S$ measurements. 137

Chapter 1

Introduction

The asthenosphere is a mechanically weak layer beneath the strong lithosphere and is of great importance to plate tectonics and mantle convection. Seismic observations [1, 2, 3, 4, 5, 6] as well as geodynamic studies based on geoid and post-glacial rebound measurements [7, 8] have long confirmed the existence of this low-velocity, low-viscosity layer in the uppermost sublithospheric mantle although its origin remains debated. This layer plays an important role in the operation of plate tectonics as its ductile nature allows it to provide crucial lubrication for the movement of the overlying tectonic plates. The low-viscosity asthenosphere also promotes long-wavelength thermal convection to efficiently cool the mantle [9, 10].

The Lithosphere Asthenosphere Boundary (LAB) and the 220-km discontinuity are the top and bottom interfaces of the asthenosphere. In this dissertation, twelve years of seismic data recorded at the global seismological network (GSN) stations are processed to investigate SS precursors reflected at the upper and lower boundaries of the asthenosphere in the global continents and oceans. Clear SS precursors bounced off the LAB and the 220-km discontinuity are observed globally despite the fact that the signals are largely absent on global stacks of SS seismograms. This might be caused by large depth variations of the 220-km discontinuity which result in destructive stacking of the seismograms. Finite-frequency tomography is applied to investigate the LAB and the 220-km interfaces and the nature of the asthenosphere.

In Chapter 2, the LAB and the 220-km discontinuity beneath the oceanic regions are investigated based on a small global dataset of SS precursors. Strong reflections from both the top and the bottom of the asthenosphere are observed across all major oceans. The average depths of the two discontinuities are $\sim$ 120 km and $\sim$ 250 km, respectively. The SS waves reflected at the lithosphere and asthenosphere boundary are characterized by anomalously large amplitudes, which require $\sim$12.5% reduction in seismic velocity across the interface. This large velocity drop cannot be explained by a thermal cooling model but indicates 1.5%-2% localized melt in the oceanic asthenosphere. The depths of the two discontinuities show large variations, indicating that the asthenosphere is far from a homogeneous layer but likely associated with strong and heterogeneous small-scale convections in the oceanic mantle. The average depths of the two boundaries are largely constant across different age bands. In contrast to the half space cooling model, this observation supports the existence of a constant-thickness plate in oceanic regions with a complex and heterogeneous origin.

In Chapter 3, Finite-Frequency tomography is applied to explore the spacial characteristics of the 220-km discontinuity in the global oceans. A larger data set of SS precursors with bouncepoints in the global oceans are analyzed. The global model obtained from Finite-Frequency tomography shows that the 220-km depth perturbations roughly follow the age contours, however, the average depth of the 220-km discontinuity is independent of seafloor age. We compute the surface Laplacian (roughness) of the 220-km discontinuity depth to characterize the lateral depth perturbatioins of the discontinuity. The most interesting observation on the topography of the 220-km discontinuity is that the roughness of the discontinuity increases with seafloor spreading rate. The geodynamic processes responsible for this positive correlation is unclear, but it indicates small-scale convections in the oceanic

asthenosphere may be controlled by seafloor thermal structures formed during the initial melting and deformational processes at spreading centers.

SS precursors with bounce points in continental regions are analyzed in Chapter 4. SS precursors reflected off this discontinuity are observed across all tectonic regions, from orogeny belts to stable cratons, confirming the global existence of the 220-km discontinuity. However, the 220-km discontinuity may become weak or absent when stacking is applied in regions where large lateral perturbations are present as confirmed by the analysis based on the global map of the 220-km discontinuity obtained from finite-frequency tomography. The average depth of this discontinuity beneath the continents is about 250 km, with an average velocity increase of 7% across the interface. The average depth and lateral perturbations of the discontinuity in continental regions are comparable to what was observed for oceanic regions in Chapter 3. In continental regions, there is a broad correlation between surface tectonics and the depths of the 220-km discontinuity. For example, depth anomalies are observed at the southern border of the Eurasian plate along the mountain belts from the Mediterranean region to East Asia. Depth anomalies are also observed along the Pacific subduction zone, as well as in more stable continental interiors. The correlation between S-wave speed perturbations and the depth of the 220-km discontinuity is weak to non-existent. This indicates that secular cooling does not have a significant impact on the base of the asthenosphere.

Bibliography

[1] Anderson, D. L. Lithosphere, asthenosphere, and perisphere. *Reviews of Geophysics* **33**, 125–149 (1995).

[2] Van der Lee, S. & Nolet, G. Upper mantle s velocity structure of north america. *Journal*

of Geophysical Research: Solid Earth **102**, 22815–22838 (1997).

[3] Karato, S.-i. & Jung, H. Water, partial melting and the origin of the seismic low velocity and high attenuation zone in the upper mantle. *Earth and Planetary Science Letters* **157**, 193–207 (1998).

[4] Thybo, H. The heterogeneous upper mantle low velocity zone. *Tectonophysics* **416**, 53–79 (2006).

[5] Fischer, K. M., Ford, H. A., Abt, D. L. & Rychert, C. A. The lithosphere-asthenosphere boundary. *Annual Review of Earth and Planetary Sciences* **38**, 551–575 (2010).

[6] Karato, S.-i. On the origin of the asthenosphere. *Earth and Planetary Science Letters* **321**, 95–103 (2012).

[7] Barrell, J. The strength of the earth's crust. *The Journal of Geology* **22**, 655–683 (1914).

[8] Richards, M. A. & Lenardic, A. The cathles parameter (ct): a geodynamic definition of the asthenosphere and implications for the nature of plate tectonics. *Geochemistry, Geophysics, Geosystems* **19**, 4858–4875 (2018).

[9] Höink, T. & Lenardic, A. Long wavelength convection, poiseuille–couette flow in the low-viscosity asthenosphere and the strength of plate margins. *Geophysical Journal International* **180**, 23–33 (2010).

[10] Höink, T. & Lenardic, A. Three-dimensional mantle convection simulations with a low-viscosity asthenosphere and the relationship between heat flow and the horizontal length scale of convection. *Geophysical Research Letters* **35** (2008).

Chapter 2

Age-Independent Oceanic Plate Thickness and Asthenosphere Melting from SS Precursor Imaging

This chapter has been modified from a published article by Sun and Zhou (2023) [1].

2.1 Introduction

In the plate tectonic theory, the outermost shell of the Earth consists of a small number of rigid plates (lithosphere) moving horizontally on the mechanically weak asthenosphere. The origin of the asthenosphere as well as the defining mechanism of its top and bottom rheological interfaces have been highly controversial [2, 3, 4, 5, 6, 7, 8]. The oceanic plates make up ∼70% of the Earth's surface and they have a relatively simple geological and tectonic history and therefore they are ideal for resolving these fundamental questions. The classic half-space cooling model predicts that the thickness of the thermal boundary layer as well as the depth of the ocean increase proportionally with the square root of the sea-floor age. While this simple conductive cooling model successfully explains the first-order observations in the oceans, bathymetry and heat flow measurements at seafloor older than ∼70 million years do not follow the age dependence predicted by the half space cooling model. The

plate model, which assumes additional heat at the base of an oceanic plate with a constant thickness, successfully explains the flattening of sea floor depth and heat flow observations [9]. However, such a constant-thickness plate has not been observed in seismology at a global scale, and the exact source of the additional heat remains unclear, probably associated with small-scale convections [9, 10, 11, 12] or oceanic hotspots [13].

It is a general feature in global seismic surface wave studies that the high-velocity lid in oceanic regions becomes thicker with sea-floor age [14, 15, 16, 17]. It has also been suggested that a plate model with additional heat at a constant depth of about 125 km fits surface wave observations [18]. Recent surface-wave studies suggest a small amount of melt is trapped within the entire low-velocity oceanic asthenosphere [19], which might provide the additional heat required by the plate model. The depths of the lithosphere-asthenosphere boundary (LAB hereinafter) have also been studied using secondary seismic phases reflected or converted at the interface, including SS precursors [20, 21, 22], receiver functions [23, 24, 25, 26] and active source studies [27, 28]. Those studies suggest large variations as well as an origin of the asthenosphere much more complex than gradual thermal variations with depth as predicted in the half space cooling model [29]. A variety of rheological mechanisms have been proposed, including a change in grain size [30], seismic anisotropy [31, 32, 33], elastically accommodated grain boundary sliding [34] and near melting [35]. The large velocity drop and high attenuation also make partial melt a dominant mechanism in many studies [3, 8, 19, 21, 22, 23, 24, 25, 27, 28]. For example, a thin sublithosphere melt channel beneath the normal oceanic seafloor has been proposed for the equatorial Atlantic Ocean [27].

The velocity increase at the base of the asthenosphere has been incorporated in the widely used 1-D global reference earth model, PREM, with about $\sim$7% of velocity increase across

the 220-km discontinuity [36]. A discontinuity at about this depth was first observed in Europe and North America [37, 38, 39] and later confirmed by studies using surface-wave dispersion measurements, underside seismic reflections, ScS reverberations and receiver functions [40, 41, 42, 43]. This discontinuity has been reported in continental regions and is also called the Lehmann discontinuity. However, many studies have concluded that the 220-km discontinuity is not global in nature and a reflection from this depth is missing in the global long-period stacks [44, 45, 46, 47, 48], which indicates that the existence of the discontinuity is either absent in oceanic regions, or there are large variations in the depth of this discontinuity.

In this paper, we analyze twelve years of long-period transverse component seismograms recorded at 151 GSN stations (Figure A.1) to investigate SS waves reflected at the top and the bottom of the asthenosphere in oceanic regions, namely, the $S_{\mathrm{LAB}}S$ wave reflected at the LAB and the $S_{220}S$ reflected at the bottom of the asthenosphere. We will interpret the low velocity zone (LVZ) between the two discontinuities observed in oceanic regions as the asthenosphere ("weak layer") as it roughly corresponds to the depth range of the global LVZ in model PREM. This is the depth range where the geotherm may exceed mantle solidus and partial melt occurs [49].

2.2 Data & Methods

SS precursors are underside reflections from internal discontinuities and they arrive before the main SS waves which are reflected at the surface of the Earth. SS precursors are very sensitive to the structures of the interfaces at the reflection midpoints, about halfway between the earthquake and the station. They provide good data coverage in the global

oceanic areas where seismic stations are sparse. In this study, we examine 32,369 broadband seismograms at 151 GSN station from 543 earthquakes occurred between January 2009 and December 2020 with SS-wave reflection points in oceanic regions (Figures 2.1 & 2.2). The moment magnitude of the earthquakes ranges from 6.0 to 8.0 such that SS precursors are excited by potentially sufficient seismic energy [21]. We download seismograms from the Data Management Center at the Incorporated Research Institutions for Seismology (IRIS). The instrument responses are removed and the East-West and North-South component displacement seismograms are rotated to obtain the radial and transverse component seismograms.

The seismograms are band-pass filtered between 10 and 80 mHz and decimated to 0.1 second sampling interval. Seismograms with weak or complex SS waves due to source processes are discarded (Figures A.2 & A.3). Seismograms with noisy SS waves and precursors are also discarded (Figure A.3). This leaves 6,143 sets of transverse-component seismograms with epicentral distances greater than 80°. We visually inspect seismograms for SS precursors, including $S_{\rm LAB}S$, $S_{220}S$, $S_{410}S$ and $S_{660}S$. Clear $S_{\rm LAB}S$ arrivals are identified on 1,380 seismograms (about 22.5% of the entire dataset) from 144 stations and 395 earthquakes (Figures 2.1 & 2.2). The majority of the data with strong $S_{\rm LAB}S$ waves (981 out of 1380) have focal depths shallower than 45 km, and the epicentral distance varies between 80.1° and 176.3° with the majority larger than 100° (Figure A.1).

SS precursors from the 220-km discontinuity ($S_{220}S$) are observed on 2,756 seismograms. We are able to pick more $S_{220}S$ phases than $S_{\rm LAB}S$ phases from seismograms partly because many $S_{\rm LAB}S$ arrivals are too close to the main SS wave arrivals and they are not used in this study to avoid strong phase interferences. The $S_{\rm LAB}S$ and $S_{220}S$ signals can be both clearly observed on 1,021 of seismograms. There is no apparent geographic pattern associated with

the presence (or absence) of the SS precursors (Figure 2.2). The amplitudes of the secondary reflected waves are expected to be small, and the SS precursors are often below the noise level due to weak source radiation, small reflection coefficient and/or defocusing caused by mantle heterogeneities. For example, only about 30% of the recorded SS waves have clear SS precursors from the 410-km and the 660-km discontinuities in recent global studies [50, 51].

The observed SS precursors from the LAB ($S_{\mathrm{LAB}}S$) are characterized by large amplitudes that are comparable to the amplitudes of the mantle transition zone SS precursors $S_{410}S$ and $S_{660}S$ (Figure 2.1). To investigate the velocity reduction across the LAB discontinuity, we construct 1-D reference models modified from PREM to include a large velocity drop in the asthenosphere (Figure 2.3 & Figure A.4). We calculate synthetic seismograms based on traveling-wave mode summation [52]. The global centroid-moment-tensor (CMT) solutions [53, 54] and the USGS Preliminary Determination of Epicenters (PDE) [55] source locations and origin times are used in the calculations of the 1-D synthetic seismograms. The synthetic seismograms are complete, including all seismic phases with exact amplitudes for earthquakes in 1-D earth models. The effects of incident angles on seismic amplitudes have been automatically accounted for. The synthetic seismograms are then processed using the same bandpass filter as applied to the observed seismograms. The differences in SS precursors between different models facilitate the identification of the $S_{\mathrm{LAB}}S$ and $S_{220}S$ waves on the observed seismograms (Figure 2.3).

We measure the amplitudes of the SS precursors $S_{\mathrm{LAB}}S$, $S_{410}S$ and $S_{660}S$ at a period of 25 seconds. The measurements are made in the frequency domain using a 40-second window centered at the arrival time of the SS precursors (Figure 2.4). We use a short time window to limit the interference between the $S_{\mathrm{LAB}}S$ wave and the main SS wave. Example

amplitude measurement experiments using synthetic data show that amplitude ratios at the measurement frequency as well as their frequency-dependent variations can be well captured using a 40-second time window (Figure 2.5). We will focus on measurements at a period of 25 seconds in this study. The longest half duration of the earthquakes used in this study is about 25 seconds and seismic energy often decreases rapidly at frequencies higher than the earthquake corner frequency. In addition, SS precursors at higher frequencies can be heavily contaminated by noises (meteorological and multiple scattering). At periods much longer than 25 seconds, seismograms are not suitable for SS precursor studies as the precursors are not well separated and surface-wave overtone dispersion also becomes a problem. The frequency dependence of the measurements and their corresponding finite-frequency sensitivities will be documented in a separate paper. Amplitude ratios $S_{\rm LAB}S/S_{410}S$ and $S_{\rm LAB}S/S_{660}S$ are calculated for the observed datasets as well as synthetic seismograms in 1-D reference models (Figure 2.6).

We measure the differential arrival times between the SS waves and their precursors in the dataset. The observed and synthetic seismograms are aligned using the SS traveltime measurements, and the residue arrival times of the SS precursors are then calculated in the frequency domain at a period of 25 seconds [56] (Figure 2.7). The time shifts due to uncertainties in source origin times do not affect the final measurements as only $\delta t|_{S_{\rm LAB}S} - \delta t|_{SS}$ and $\delta t|_{S_{220}S} - \delta t|_{SS}$ differential traveltimes are used to determine the depths of the discontinuities. The length of the measurement windows ranges from 42 to 117 seconds for SS waves, 37 to 69 seconds for $S_{\rm LAB}S$ waves and 38 to 75 seconds for $S_{220}S$ waves. The length of a measurement window depends on the arrivals of the neighboring phases, and the measurement windows are chosen to minimize possible phase interferences. The relation between time delays and depth perturbations of the discontinuities depends on their finite-frequency sensitivity kernels. We

calculate finite-frequency traveltime sensitivities to boundary depth perturbations in the framework of travelling-wave mode coupling, which fully account for source radiation patterns, phase interactions as well as time-domain windowing and tapering applied in making frequency-dependent measurements [57, 58, 59]. Example finite-frequency boundary sensitivity kernels for traveltime measurements are plotted in Figure 2.4. The finite-frequency sensitivities display a typical X shape due to the minimax-time nature of the reflected waves [60]. Unlike direct body waves which have minimum-time ray paths, surface-reflected phases are minimax waves in that the reflection point is a stationary maximum for perturbations in the source-receiver ray plane and a minimum for perturbations perpendicular to the plane.

Seismic waves at different frequencies are sensitive to different regions (Fresnel zones) and this introduces frequency-dependent time shifts when lateral variations exist in discontinuity topography, as a result, SS precursors do not always have the same polarities as expected for 1-D earth models [50]. The interferences between different waves within the measurement window are accounted for in the calculation of the finite-frequency sensitivities, including the travel time curves of the interference phases as well as their amplitudes. We use traveltime sensitivity kernels to identify possible phase interferences in the measurement windows, including interferences with the main SS waves and other phases such as the precursors of depth phases (Figure A.5), precursors and/or multiples of ScS waves (Figure A.6). Sensitivity kernels with abnormal values indicate strong interferences and those measurements are excluded (Figures A.5 & A.6). In addition, we exclude measurements out of the two standard deviations. This leaves 1274 and 929 sets of measurements for $S_{\mathrm{LAB}}S$ and $S_{220}S$, respectively. The thicknesses of the asthenosphere at the 921 locations are calculated as the depth difference between the 220-km discontinuity and the LAB.

2.3 Results

We process a total number of 32,369 transverse component seismograms that have reflection points in oceanic regions and observe clear SS waves on 6,143 seismograms with simple source time functions. SS precursors are secondary reflected waves, their amplitudes are much smaller than the main SS waves and they are often heavily influenced by scattered waves and phase interactions. As expected, the majority of the seismograms with clear SS waves do not show strong SS precursors from the LAB and the 220-km discontinuity. The most striking observation from this dataset is the anomalously large amplitudes of the $S_{\mathrm{LAB}}S$ phases on 1,380 seismograms, with the majority (1,021 out of 1,380) accompanied by strong $S_{220}S$ phases. The SS precursors are well separated from the main SS waves, and their amplitudes are comparable to the amplitudes of the mantle transition zone phases, $S_{410}S$ and $S_{660}S$ (Figure 2.1). The geographic distribution of the reflection points is dispersive across major oceans, including the Pacific, the Atlantic and the Indian ocean, with seafloor age spanning from 10 to 170 million years old (Figure 2.1).

2.3.1 Large Amplitudes of the LAB SS Precursors

To quantify the observed large amplitudes of the SS precursors associated with the LAB discontinuity, we calculate the amplitude ratios between the $S_{\mathrm{LAB}}S$ phase and two reference phases, $S_{410}S$ and $S_{660}S$. The amplitude measurements are made in the frequency domain based on spectra division at a period of 25 seconds [50, 56], In Figure 2.6, we plot the histograms of the minimum amplitude ratios, defined as $\gamma = \mathrm{minimum}[\log(A_{S_{\mathrm{LAB}}S}/A_{S_{410}S}), \log(A_{S_{\mathrm{LAB}}S}/A_{S_{660}S})]$ (Table S1). We have used the minimum values to avoid over amplification when the amplitude of $S_{410}S$ or $S_{660}S$ is small due to scattering or defocusing. The

precursors $S_{\mathrm{LAB}}S$ and $S_{410}S$ (or $S_{660}S$) have similar ray paths in the bulk mantle, the use of amplitude ratios minimizes the impact of possible focusing and defocusing effects. In addition, the main SS waves travel through the same regions sampled by the SS precursors, and the distribution the SS amplitude measurements for the entire dataset is very similar to that for the subset in which anomalously large $S_{\mathrm{LAB}}S$ were observed, indicating that the observed large amplitudes of the $S_{\mathrm{LAB}}S$ waves are not a result of focusing caused by mantle heterogeneities (Figure A.7). To investigate possible interference from the main SS waves and other phases on the frequency-domain $S_{\mathrm{LAB}}S$ amplitude measurements, we make additional time-domain amplitude measurements using the maximum value of the envelope function for each $S_{\mathrm{LAB}}S$ measurement window. The measurements made in the frequency domain based on spectra division and those made in the time domain using envelope functions in general agree well (Figure A.8). The observed mean value of the minimum amplitude ratio γ is close to zero (Figure 2.6), indicating that the reflection coefficients at the LAB are about the same as those at the 410 and the 660. The corresponding velocity contrasts across the LAB are expected to be larger than the contrasts across the 410 and the 660 due to their smaller incident angles at shallower depths. The geographic distribution of the amplitude ratios do not show dependence on the age of the sea floor (Figure 2.6).

To estimate the velocity change across the LAB, we construct a 1-D reference model with the depths of the LAB and the 220-km discontinuity at 130 km and 250 km, respectively (Figure 2.3). The velocity jump across the LAB is 12.5% in the reference model (Model I). SS precursors from all upper mantle discontinuities can be clearly identified on the observed seismograms when the observed and synthetic seismograms are filtered to the same frequency band (Figure 2.1). We make amplitude measurements and calculate the relative amplitude ratios $\gamma = \mathrm{minimum}[\log(A_{S_{\mathrm{LAB}}S}/A_{S_{410}S}), \log(A_{S_{\mathrm{LAB}}S}/A_{S_{660}S})]$ using the synthetic

seismograms following the same process as applied on the observed seismograms. The amplitude ratios between $S_{\mathrm{LAB}}S$ and $S_{410}S$ (or $S_{660}S$) calculated for Model I are very close to the observations (Figure 2.6). To better constrain the velocity drop across the LAB required to produce the large amplitudes of $S_{\mathrm{LAB}}S$, we introduce two additional models, Model II with 6% of velocity drop and Model III with 11% of velocity drop across the LAB. Example synthetic seismograms are plotted in Figure 2.3 and the amplitude measurements are plotted in Figure 2.6. The mean logarithm amplitude ratio γ calculated using Model II as a reference model is -0.3, meaning that the corresponding average amplitudes of the LAB precursors are about 50% of the amplitudes of the 410 (or the 660) precursors, much smaller than the observations. The mean logarithm amplitude ratio γ calculated using Model III as a reference model is slightly smaller than the observed value. Based on the calculations, we conclude that 12.5% of velocity drop across the LAB is necessary in our model to explain the observed large amplitude of the $S_{\mathrm{LAB}}S$ waves (Figure 2.6).

2.3.2 Depths of the LAB and the 220-km Discontinuity

To constrain the depths of the LAB and the 220-km discontinuity, we measure the differential traveltimes $\delta t|_{S_{\mathrm{LAB}}S} - \delta t|_{SS}$ and $\delta t|_{S_{220}S} - \delta t|_{SS}$ with respect to synthetic seismograms calculated in Model I (Figure 2.7), similar to the studies of [50, 51] in which $S_{410}S$ and $S_{660}S$ traveltime measurements were used to investigate the depths of the 410-km and the 660-km discontinuities at a global scale. The time shifts due to uncertainties in source origin times do not affect the final measurements as we use differential traveltimes. We apply 3-D crust and mantle wave speed corrections using global models CRUST1.0 [61] and S40RTS [62]. Model I is constructed as the reference model for the oceanic regions where large-amplitude SS precursors have been observed. As it is not a global reference model, there is overall

about 5 seconds of traveltime shifts in $\delta t|_{S_{\mathrm{LAB}}S}$-$\delta t|_{SS}$ after 3-D wavespeed and crustal corrections (Figure 2.7 & Figure A.9). The mean $\delta t|_{S_{220}S}$-$\delta t|_{SS}$ traveltime delay before and after the corrections remains approximately the same, with an average value close to zero. This indicate that the average velocity in the uppermost mantle in the reference model is close to the global average.

To obtain depth perturbations of the LAB and the 220-km discontinuity, we calculate the sensitivities of the differential traveltimes to depth perturbations of the interfaces by integrating the finite-frequency sensitivity kernels over the surface of the boundary (Figure 2.4). The LAB depths obtained from this study varies between ∼70 and ∼160 km (Figure 2.8) and the mean LAB depths obtained using the same data with and without the corrections are 120 km and 125 km, respectively (Figures 2.8 & A.10). The depth of the 220-km discontinuity varies between 180 and 340 km with a mean value of ∼255 km, and it does not change with wavespeed and crustal corrections. We calculate the thickness of the asthenosphere in regions where both the LAB and the 220-km discontinuities are well defined by strong SS precursors from both discontinuities. The thickness of the asthenosphere ranges from 50 km to 220 km with an average of 140 km. Large depth variations of the LAB and the 220-km discontinuity are observed across the global oceanic regions and the depth can change abruptly over small geographic distances.

The depths of the LAB and the 220-km discontinuity are plotted as a function of seafloor age [63] in Figure 2.9. The depths of the two discontinuities obtained using the same dataset but without the 3-D crustal and mantle wave speed corrections are plotted in Figure A.11. The average depth of the two discontinuities are independent of seafloor age, regardless of the corrections applied. To quantify uncertainties in traveltime measurements and discontinu-

ity depth perturbations, we calculate frequency-dependent traveltime measurements at five different periods ranging from 23 to 27 seconds. The standard deviation of those traveltime measurements are then converted to uncertainties in discontinuity depth using the corresponding finite-frequency sensitivities. The depth uncertainties are plotted as error bars in Figure 2.9, they are generally small, with an average of 1.1 km for the LAB and 1.2 km for the 220-km discontinuity.

2.4 Discussions

2.4.1 Melt Spots in the Oceanic Asthenosphere

The observed large amplitudes of the SS precursors require a large velocity change across the LAB. The presence of a small amount of melt may significantly reduce seismic velocity. It has been suggested that S-wave velocity reduction is about 7.9% for every percent of melt in realistically shaped melt in the upper mantle based on finite element calculations for shear modulus reduction (produced by the presence of a connected network of realistically shaped and naturally organized melt inclusions), with the geometries of the inclusions taken directly from laboratory calculations [64]. The finite element model predictions are also in general agreement with recent experimental results [65]. The large amplitudes of the SS precursors observed in this study can be explained by 1.5%-2% of melt in the asthenosphere. This melt concentration is comparable to observations at mid-ocean ridges, for example, the East Pacific Rise [66]. In a recent surface-wave study [19], a large melt fraction of up to 1% beneath the entire oceanic lithosphere has been suggested, in general agreement with the overall estimation of melt (0.3-2%) from electrical conductivity study [67].

A sharp increase in the water content across the LAB has been proposed as a possible candidate for significant wave speed reduction through enhanced anelasticity [34, 68]. To explore the effect of anelasticity (seismic quality factor Q) on the amplitudes of SS precursors, we calculate synthetic seismograms in models with and without strong anelasticity in the asthenosphere and compare the amplitudes of the SS precursors. In Figure 2.10, the velocity and density structures in Model I and Model IV are identical but their Q values in the asthenosphere are different, Q=80 in Model I and Q=20 in Model IV. The low Q value in the asthenosphere in Model IV results in a much smaller SS amplitude but the amplitude reduction on the $S_{\mathrm{LAB}}S$ wave is very limited. This is because while both the SS wave and the $S_{\mathrm{LAB}}S$ wave experience more attenuation due to enhanced anelasticity, anelasticity also reduces the effective wave speed in the low Q region. Therefore, the effective velocity contrast across the LAB increases, resulting a larger reflection coefficient and increased amplitude of the $S_{\mathrm{LAB}}S$ wave. The amplitude ratios calculated in Model I (Figure 2.6) and Model IV (Figure 2.10) do not show significant differences in their histograms. We conclude that the large amplitudes of $S_{\mathrm{LAB}}S$ waves therefore can not be explained by a change in anelasticity.

The observed large amplitudes of the SS precursors can not be explained by seismic anisotropy. Strong radial anisotropy (up to 10%) has been observed in the oceanic asthenosphere with SH waves travelling faster than SV waves [32, 36, 69, 70, 71]. This radial anisotropy would lead to larger SH wave velocity beneath the LAB, and therefore reduced velocity contrast across the LAB and smaller precursor amplitudes, while the observed large amplitudes of the SS precursors require anomalously large velocity drop (12.5%) across the boundary. Frozen-in radial anisotropy in the oceanic lithosphere from petrological fabrics or melt ponding has been suggested [31]. In this case, the SH wave speed would become faster in the oceanic lithosphere, which may cause a larger SH velocity contrast across the LAB but a reduced

velocity contrast in SV velocity. In this study, strong $S_{\mathrm{LAB}}S$ phases are also observed on the radial component seismograms (Figure A.12). The observed SS precursors with large amplitudes also display a good azimuth coverage (Figure 2.1), indicating that the observed large amplitudes of the $S_{\mathrm{LAB}}S$ waves are unlikely a result of azimuth anisotropy in the lithosphere [32].

It is important to emphasize that we have interpreted the low velocity zone (LVZ) between the two discontinuities observed in oceanic regions as the asthenosphere, and we have modeled the wavespeed structure associated with reflected waves as first-order discontinuities. In 1-D earth models (e.g., PREM), a first-order discontinuity is an equivalent mathematical representation of the earth structure. The same applies to other discontinuities in the Earth including the Moho, the 410 and the 660. Synthetic seismograms calculated based on the equivalent first-order discontinuities can explain the observed seismograms. The large amplitude of the LAB phase observed in this study requires about 12.5% of velocity jump across a first-order discontinuity. The same velocity change over a gradient zone of 5 km or less may also explain the observed $S_{\mathrm{LAB}}S$ amplitudes, with less than 2% of difference in their average amplitudes (Figure A.13). If the velocity change occurs over a much larger gradient zone of 20 km, the average $S_{\mathrm{LAB}}S$ amplitude will decrease by $\sim$17%, and the required velocity increase would be larger in order to produce the same peak amplitude [57].

2.4.2 Age-Independent Thickness of the Oceanic Plate

The observed LAB SS precursors characterized by large amplitudes can be modeled as waves reflected off a first-order discontinuity with a large velocity contrast. The strong SS precur-

sors from the LAB are observed across the global oceanic regions, with an average depth of 120 km that is independent of seafloor age (Figure 2.9). This observation supports the plate model for the oceanic bathymetry and heat flow measurements, in which a reheating process is required at the base of the oceanic plate with a constant thickness of about 100-125 km. The reheating process is probably caused by small-scale mantle convection beneath the large oceanic plate [10].

The observed depths of the LAB in this study are characterized by substantial local variations. The standard deviation of the LAB depths calculated for the entire dataset is at ∼15 km. We calculate the standard deviation of the LAB depths at different length scales (Figure A.14). The standard deviation can be up to ∼17 km at small length scales and it becomes consistent with the standard deviation of the entire dataset when the length scale exceeds ∼1000 km. Reflectors at depths between 120 and 180 km have been detected across the Pacific ocean in a SS precursor stacking study, though they were found in only 16% of the stacks [21]. LAB reflectors at depths of about 100-140 km have been reported in Hawaii where high-resolution receiver function studies are available with the deployment of local stations [24, 25]. The large variation of the LAB depths is also consistent with surface waves studies in which individual transects often display considerable depth variability in age-averaged profiles [8, 14].

In seismic studies, age-dependent reflectors have been reported in several oceanic regions, especially under the young seafloors [20, 22, 72, 73]. For example, a recent receiver function study from ocean bottom seismometers in the equatorial Mid Atlantic Ocean discovered that the LAB depth increases from about 30 km at the mid-ocean ridge to about 80 km beneath 30 million years old seafloors in some locations [72]. The relation between the crust age and

the LAB depth is much less clear across the Pacific Ocean and it has been suggested that regional dynamical processes may play an important role in asthenospheric melt production [21]. SS precursors reflected off the LAB is observed beneath all oceans in this dataset regardless of seafloor age. It is important to point out that the horizontal grid spacing in our model is about 4.3 degrees, and variations smaller than a couple of hundred kilometers may not be imaged in our model. For example, if the LAB becomes shallower in a small region near mid-ocean ridges, it may not be imaged in the model. In this study, we use long period SS waves, as a result, signals from a very shallow reflector (<40 km) will interfere with the main SS waves and will not be picked up. It is also possible that there may be multiple reflectors in the lithosphere in some regions and what we observe in this study represents a strong deep reflector associated with melting not secular cooling. In general, velocity change associated with a thermal lithosphere is expected to be smaller and much more gradual than the reflectors associated with the chemical differentiation (melting) process. Double reflectors have been observed beneath mid-ocean ridges in some regional studies [74], the connection between the LAB we observe and the shallower reflector associated with decompression melting is still unclear.

Similar to the LAB, the depths of the 220-km discontinuity also do not depend on the age of the seafloor and are characterized with large local variations. It is understood that the smoothness (roughness) of a same discontinuity in different studies often depends on the regions of study as well as smoothing applied in some of the inversions. Reflectors at depths of 250-300 km (the X discontinuity) have been observed in many oceanic regions, including the South Pacific and the Indian Ocean [44, 45]. Large depth variations up to ∼100 kilometers on the 220-km discontinuity have been report over length scales of several hundred kilometers beneath the northwestern Pacific in a short-period array study [75]. The large local

variations in the depths of the discontinuities are expected to generate significant variability in both the waveforms and travel times of the SS precursors. When stacking is applied to SS precursors with reflection points in regions where large depth variations occur over very short distances, it may be possible that the large amplitudes of SS precursors could be effectively averaged out in stacking results due to phase equalization [46]. In Figure A.15, we show a simple example to illustrate the concept that, in some cases, the large amplitudes of SS precursors may not be picked up in stacking results when large variations in SS precursor amplitudes and arrival times are present.

2.5 Conclusions

The thermal boundary as predicted by the half space cooling model is not observed in SS precursors in this study. Instead, we observe anomalously large amplitudes of SS precursors reflected off the lithosphere-asthenosphere boundary (LAB), which can be explained by ~12.5% of velocity drop across the boundary. This result indicates 1.5%-2% of localized melt across the global oceanic regions. The large variability in the depths and amplitudes of the SS precursors observed across the global oceanic region suggests a heterogeneous melting process in the oceanic asthenosphere. The majority of the LAB SS precursors are accompanied by strong reflections from the 220-km discontinuity. This indicates that the 220-km discontinuity may define the lower boundary of the local asthenosphere where melting occurs.

The plate model, which requires additional heat at the base of a constant-thickness oceanic plate, explains the bathymetry and heat flow observations that do not follow half space cooling predictions. While such a constant-thickness plate has not been reported in seismic

studies, the oceanic plate as defined by the strong LAB reflector in this study does not thicken with age but show an average depth of 120 km across different age bands. This observation supports the existence of a constant-thickness plate in oceanic regions. The localized melt spots distributed over the global oceanic regions may be essential to decouple the oceanic plates from the underlying mantle by dramatically reducing the mantle viscosity [19, 76].

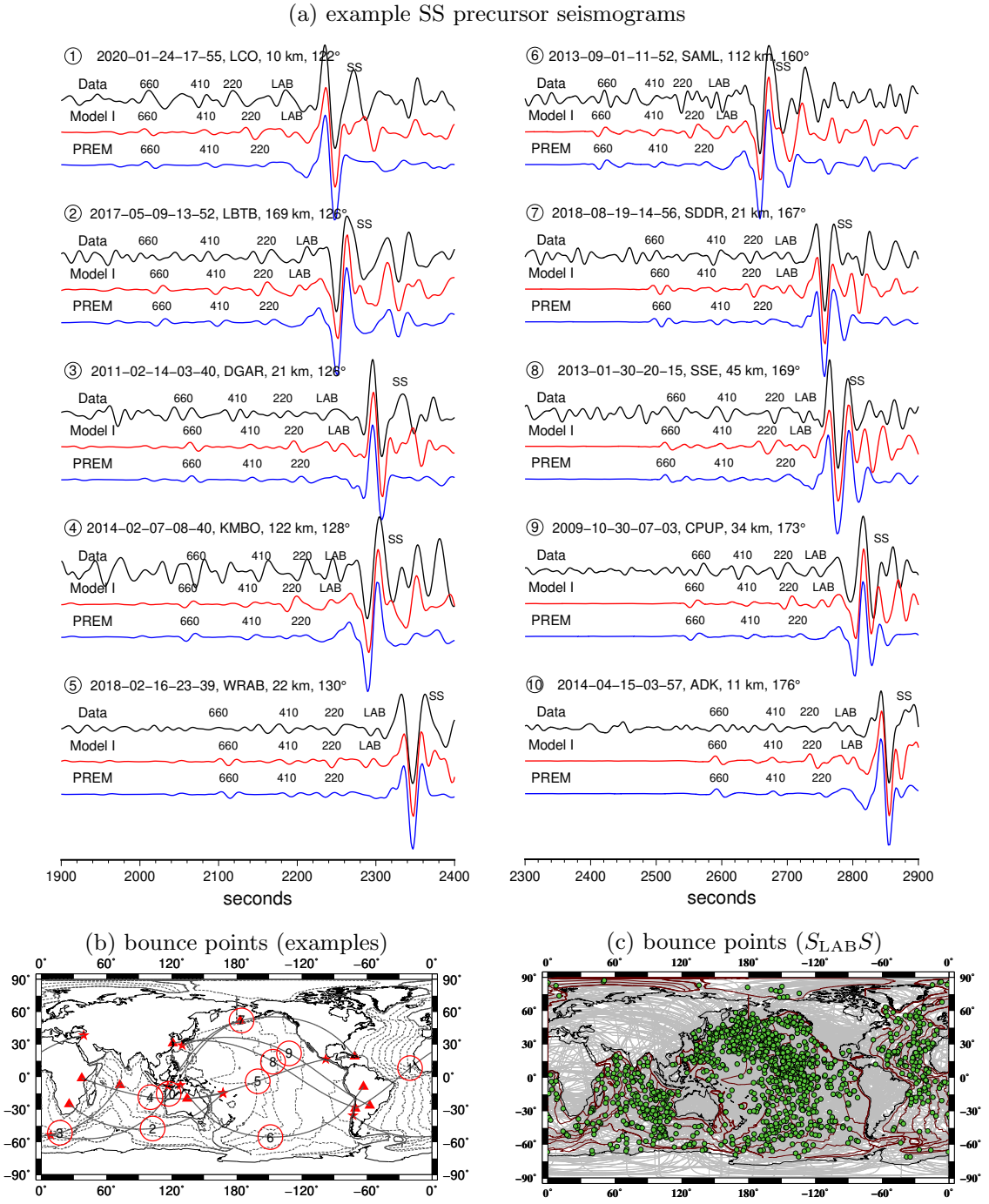

Figure 2.1: (a) example transverse-component seismograms with large-amplitude $S_{\mathrm{LAB}}S$ and $S_{220}S$ phases. The black seismograms are data, the red seismograms are synthetics calculated in a reference 1-D model (Model I) with 12.5% of the velocity jump across the LAB, and the blue synthetics are calculated in PREM in which there is no discontinuity at the LAB depth. The reference models are plotted in Figure 2.3. The seismograms have been band-pass filtered between 10 and 80 mHz and aligned using their SS arrivals for better illustration. The precursor closest to the main SS wave is labeled as $S_{\mathrm{LAB}}S$ as we investigate possible reflections from the top of the asthenosphere. The arrivals of the $S_{220}S$, $S_{410}S$ and $S_{660}S$ waves are also labeled. The earthquake event date/time and station name as well as depth and epicentral distance are denoted on each seismogram. The corresponding geographic ray paths (black lines) and bounce points (red circles) of the $S_{\mathrm{LAB}}S$ waves are plotted in (b). Ray paths and bounce points of the 1,380 $S_{\mathrm{LAB}}S$ waves with anomalously large amplitudes are plotted in (c). Seafloor age contours are plotted at 20, 60, 100 and 140 Ma.

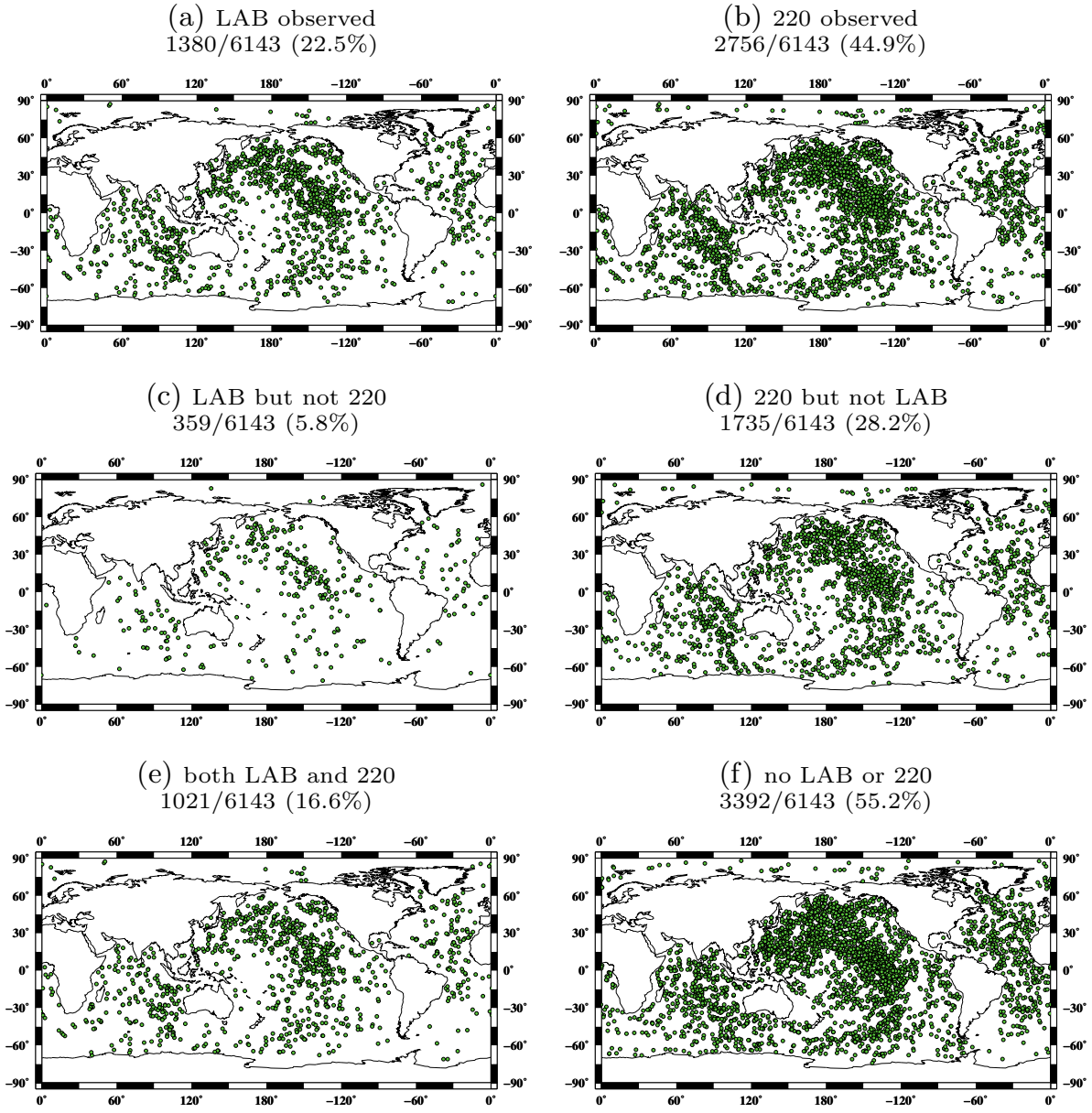

Figure 2.2: Geographic distribution of subsets of the data plotted at SS bounce points. (a) clear $S_{\mathrm{LAB}}S$ observed, (b) clear $S_{220}S$ observed, (c) $S_{\mathrm{LAB}}S$ observed but not $S_{220}S$, (d) $S_{220}S$ observed but not $S_{\mathrm{LAB}}S$, (e) both $S_{\mathrm{LAB}}S$ and $S_{220}S$ observed, (f) no $S_{\mathrm{LAB}}S$ or $S_{220}S$ observed. There is no apparent geographic pattern associated with either the presence or absence of the $S_{\mathrm{LAB}}S$ and $S_{220}S$.

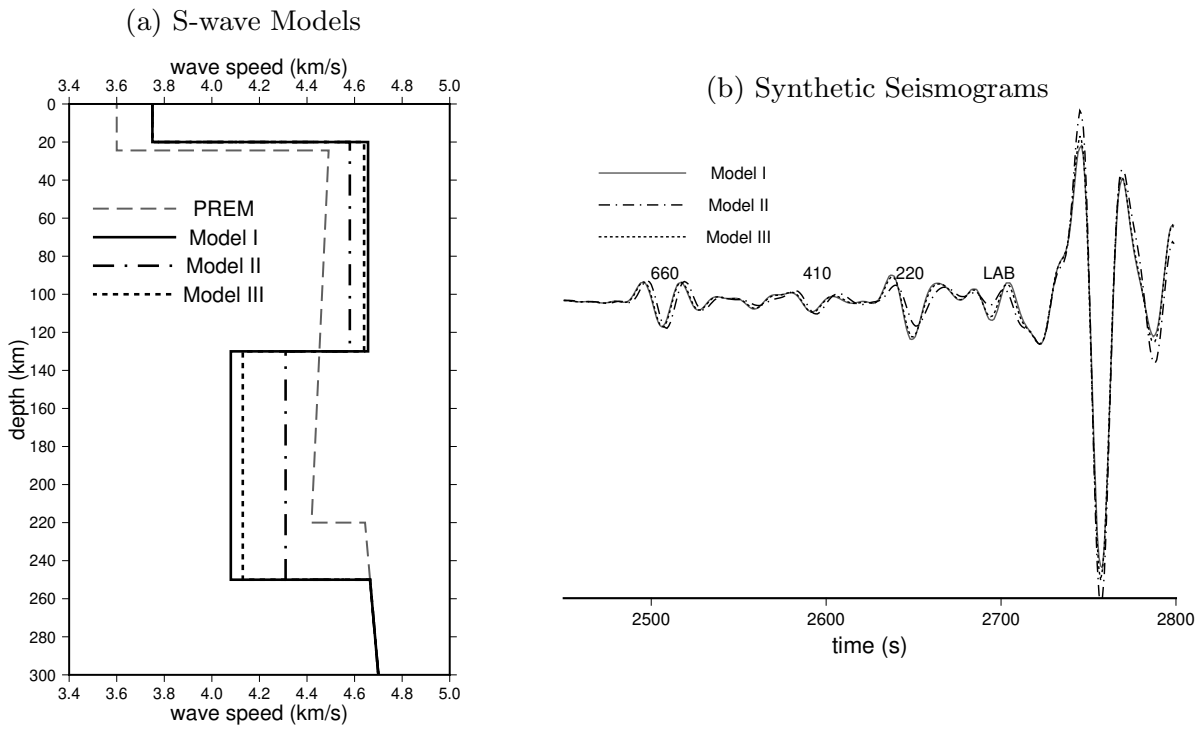

Figure 2.3: (a) Three 1-D reference earth models Model I, Model II and Model III used in this study and their corresponding example synthetic seismograms are plotted in (b). Model PREM is also plotted in (a) for reference. The synthetic seismograms are calculated using the three reference models for a magnitude 6.9 Indonesia earthquake occurred in August 2018 recorded at a GSN station SDDR (https://doi.org/10.7914/SN/CU). The observed seismogram is plotted in Figure 2.1. The seismograms have been band-pass filtered between 10 and 80 mHz and have been aligned using the main SS wave arrivals for better illustration. The velocity contrast across the LAB at a depth of 130 km is 12.5% in Model I, 6% in Model II and 11% in Model III. The corresponding $S_{\mathrm{LAB}}S$ wave amplitude in Model I is much larger than that in Model II and slightly larger than that in Model III, as expected.

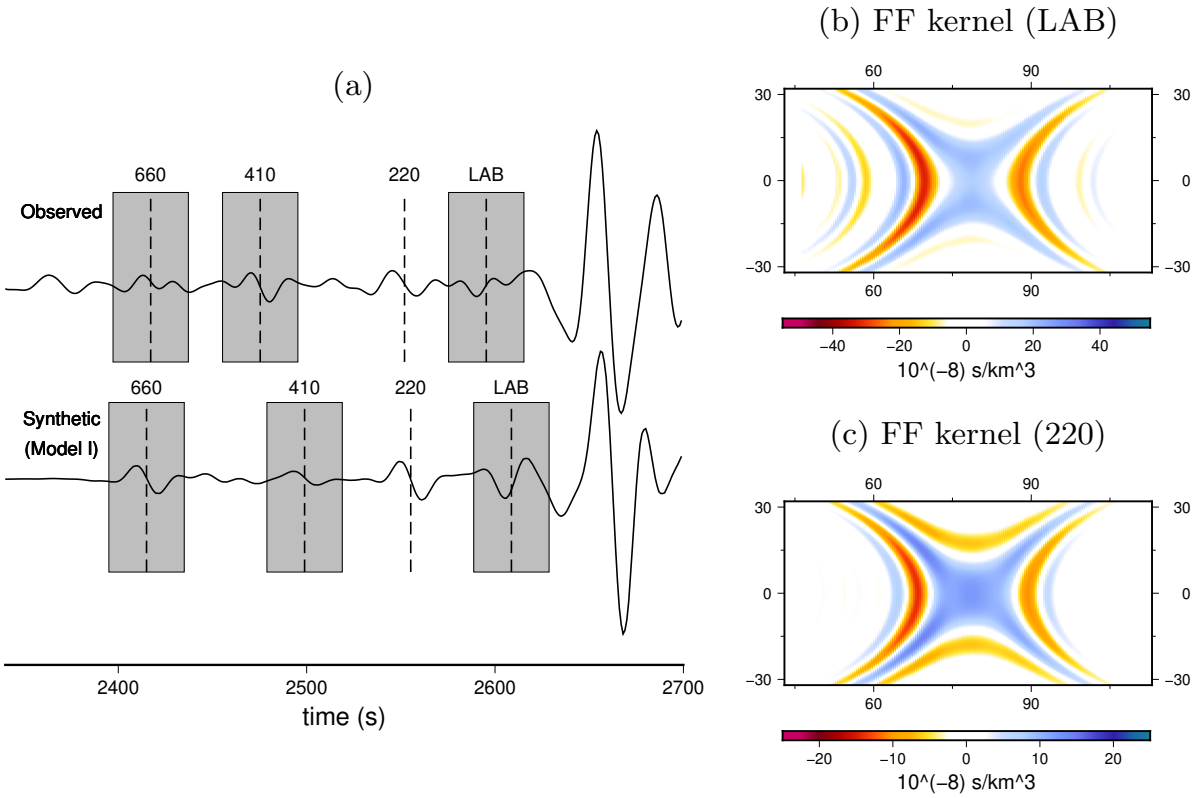

Figure 2.4: (a) shows example measurement windows used for LAB amplitude ratio measurements $A_{S_{\mathrm{LAB}}S}/A_{S_{410}S}$ and $A_{S_{\mathrm{LAB}}S}/A_{S_{660}S}$. The seismograms are for a magnitude 6.6 Mexico earthquake occurred in January 2016 recorded at a GSN station MSEY (https://doi.org/10.7914/SN/II), and the epicentral distance is 158°. The synthetic seismogram is calculated for Model I as in Figure 2.3 and both seismograms have been band-pass filtered between 10 and 80 mHz. (b) and (c) are finite-frequency traveltime boundary sensitivity kernels for the $S_{\mathrm{LAB}}S$ and $S_{220}S$ waves, respectively. The sensitivity kernels are plotted in map view in the ray coordinates, centered at the bounce point which is about 79° away from the source and the receiver.

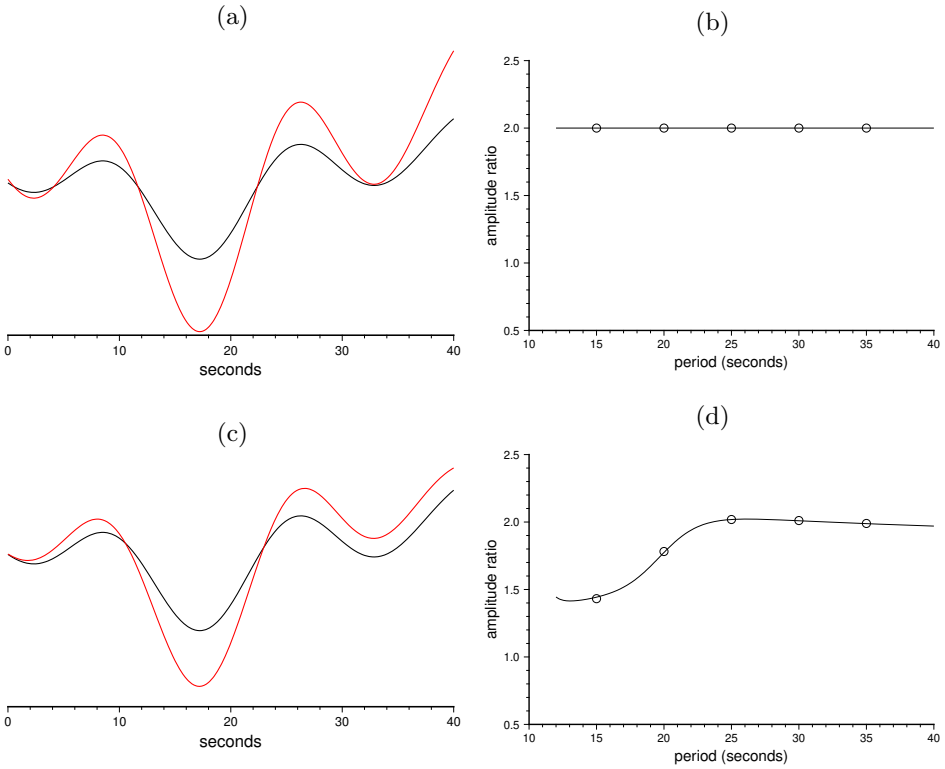

Figure 2.5: Synthetic amplitude measurement experiment using the same 40-second time window as applied in data. (a) The black seismogram is the LAB phase from the observed seismogram in Figure 2.4, and we multiply the seismogram by a constant factor of two (frequency-independent) to obtain the red seismogram. (b) Theoretical amplitude spectral ratio (black line) and measurements made at periods of 15, 20, 25, 30 and 35 seconds (circles). (c) The black seismogram is the same as in (a) and the red seismogram is obtained by multiplying the amplitude spectrum of the black seismogram with a frequency-dependent function. The corresponding theoretical amplitude ratios and measurements made at 15, 20, 25, 30 and 35 seconds period are plotted in (d). The experiment confirms that amplitude ratios at the measurement frequency (25 seconds) can be determined using a 40-second time window.

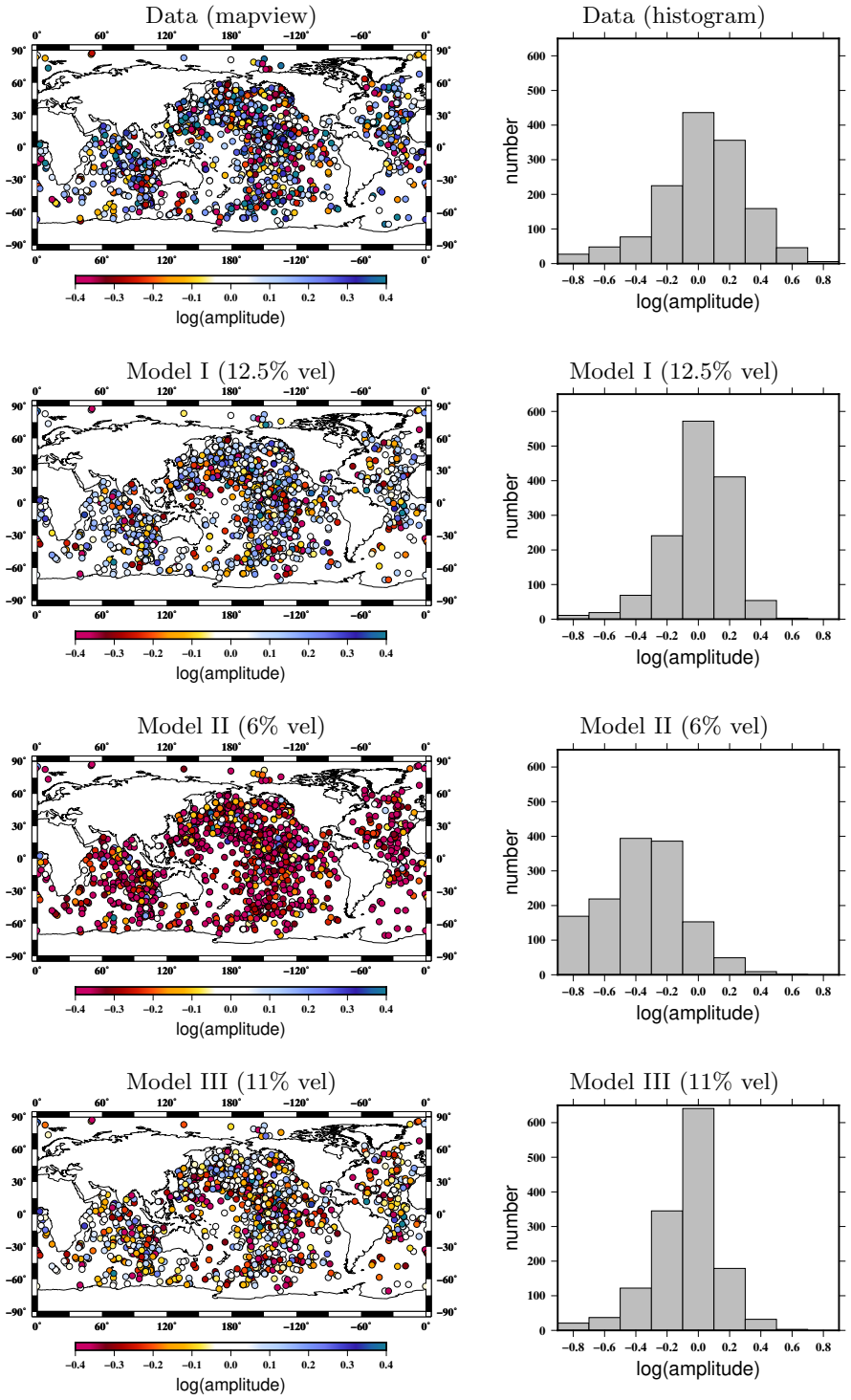

Figure 2.6: $S_{\rm LAB}S$ amplitude measurements γ= minimum $[\log(A_{S_{\rm LAB}S}/A_{S_{410}S}),\ \log(A_{S_{\rm LAB}S}/A_{S_{660}S})]$ obtained using observed seismograms (top) as well as synthetic seismograms calculated for three reference models (Model I, II and III) plotted at the bounce points in mapviews and histograms. The observed $S_{\rm LAB}S$ amplitudes show a similar distribution (histogram) to the amplitude ratios calculated for Model I (12.5% velocity drop across the LAB). The amplitude ratios calculated in Model II (6% velocity drop across the LAB) are overall much smaller than the observations, and the amplitude ratios calculated in Model III (11% velocity drop across the LAB) are slightly smaller than the observed amplitude ratios. We conclude that the observed large amplitude of the $S_{\rm LAB}S$ waves can be explained by 12.5% of velocity drop across the LAB.

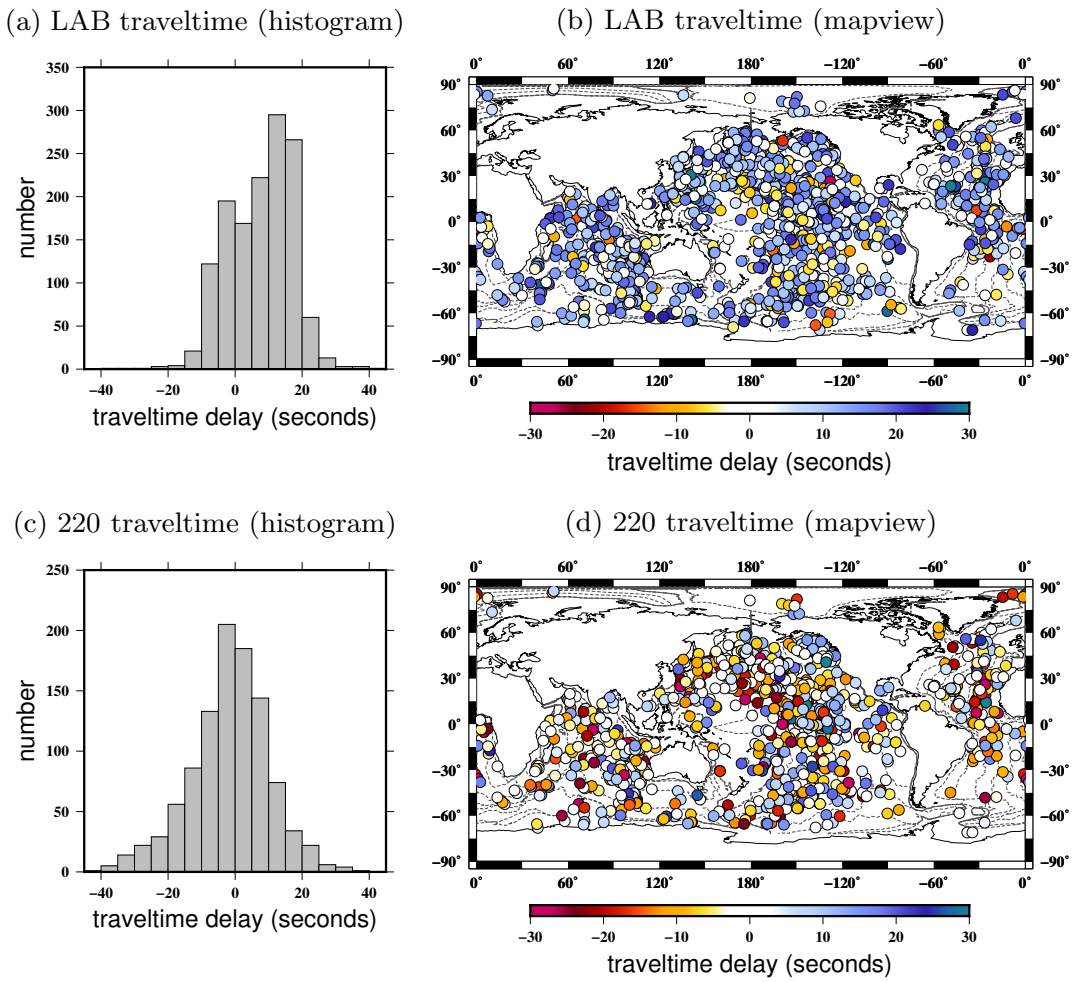

Figure 2.7: (a) and (b) are $S_{\mathrm{LAB}}S$ traveltime measurements plotted in histograms and mapviews at their bounce points. The measurements are made with respect to Model I synthetic seismograms. 3-D mantle wavespeed and crustal corrections have been applied. (c) and (d) are the same as (a) and (b) but for $S_{220}S$.

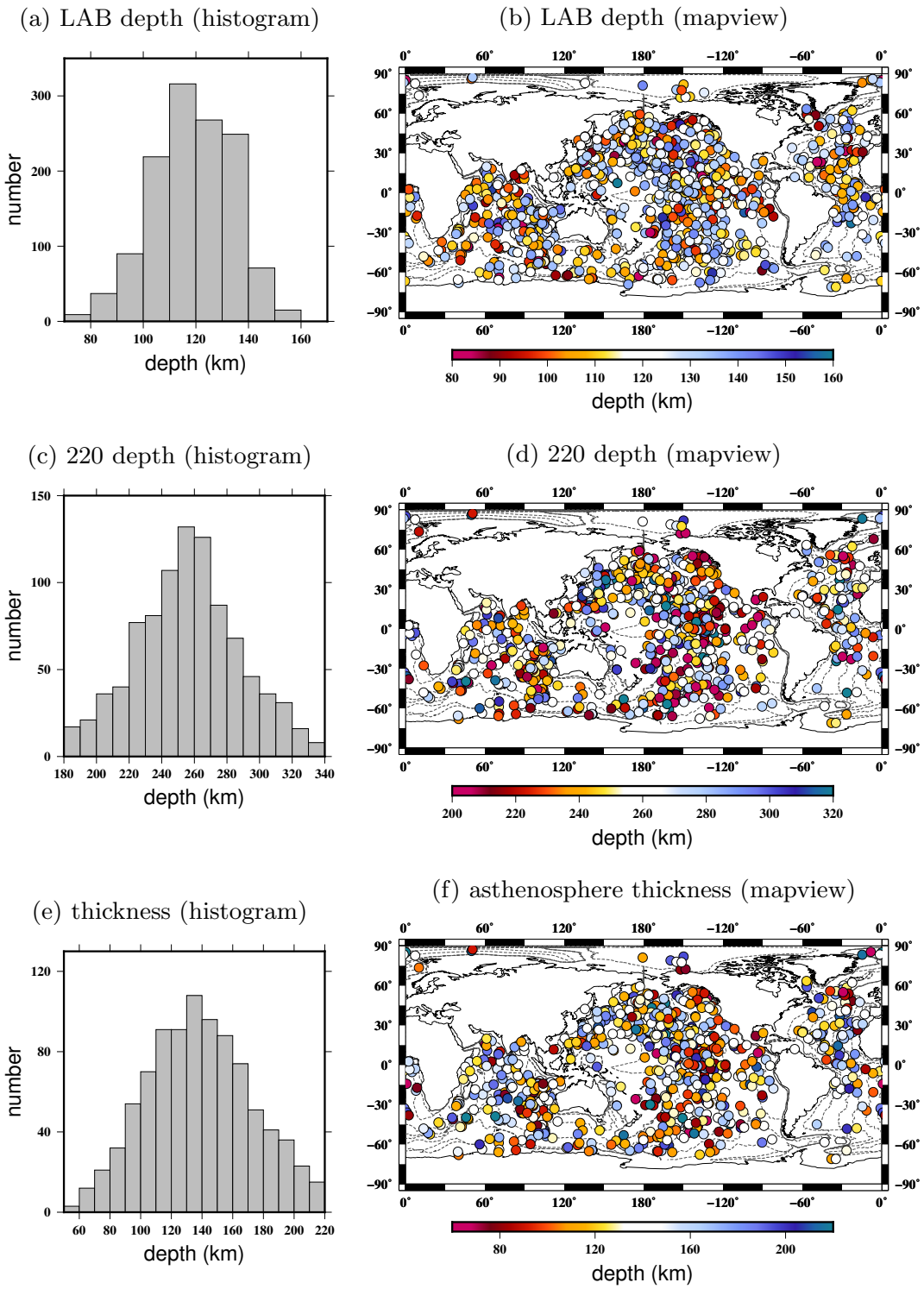

Figure 2.8: (a) and (b) are the depths of the LAB calculated from traveltime measurements, plotted in histogram and mapview at $S_{\mathrm{LAB}}S$ bounce points. (c) and (d) are the depths of the 220-km discontinuity. (e) and (f) are the asthenosphere thicknesses calculated from the depths of the LAB and the 220.

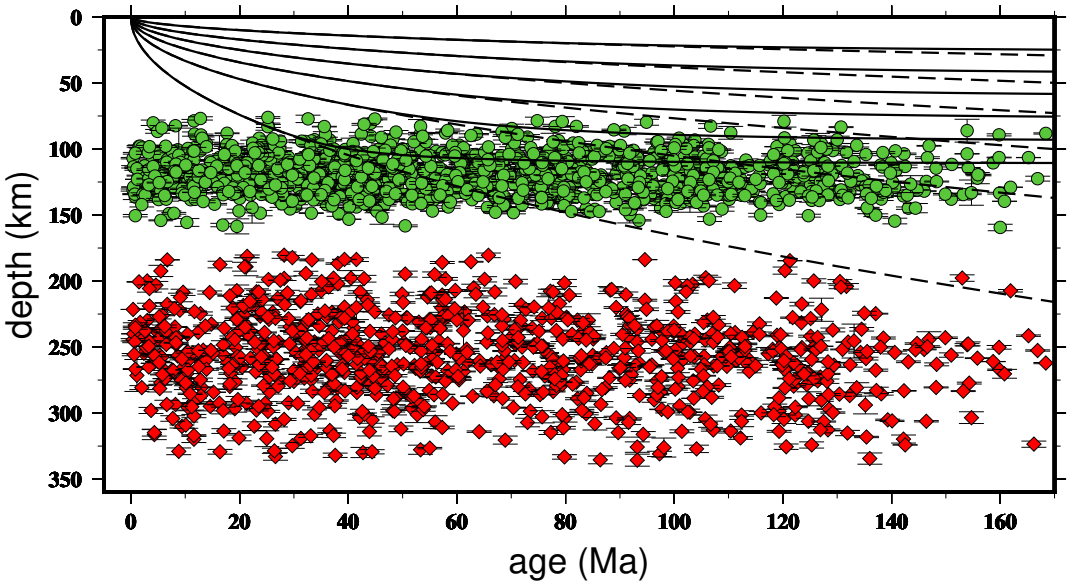

Figure 2.9: **Age-independent thickness of the oceanic plate.** Green circles and red diamonds are depths of the LAB and the 220-km discontinuity obtained from this study, plotted as a function of the seafloor age. Isotherms at an interval of 200°C (starting at 300°C) from the half space cooling model (dashed line) and the plate model (solid line) are plotted for reference. The observed depths of the two discontinuities show significant local variations. The average depths of the LAB and the 220-km discontinuity are at 120 km and 255 km, independent of seafloor age. The depth uncertainties estimated from frequency-dependent measurements are plotted as error bars.

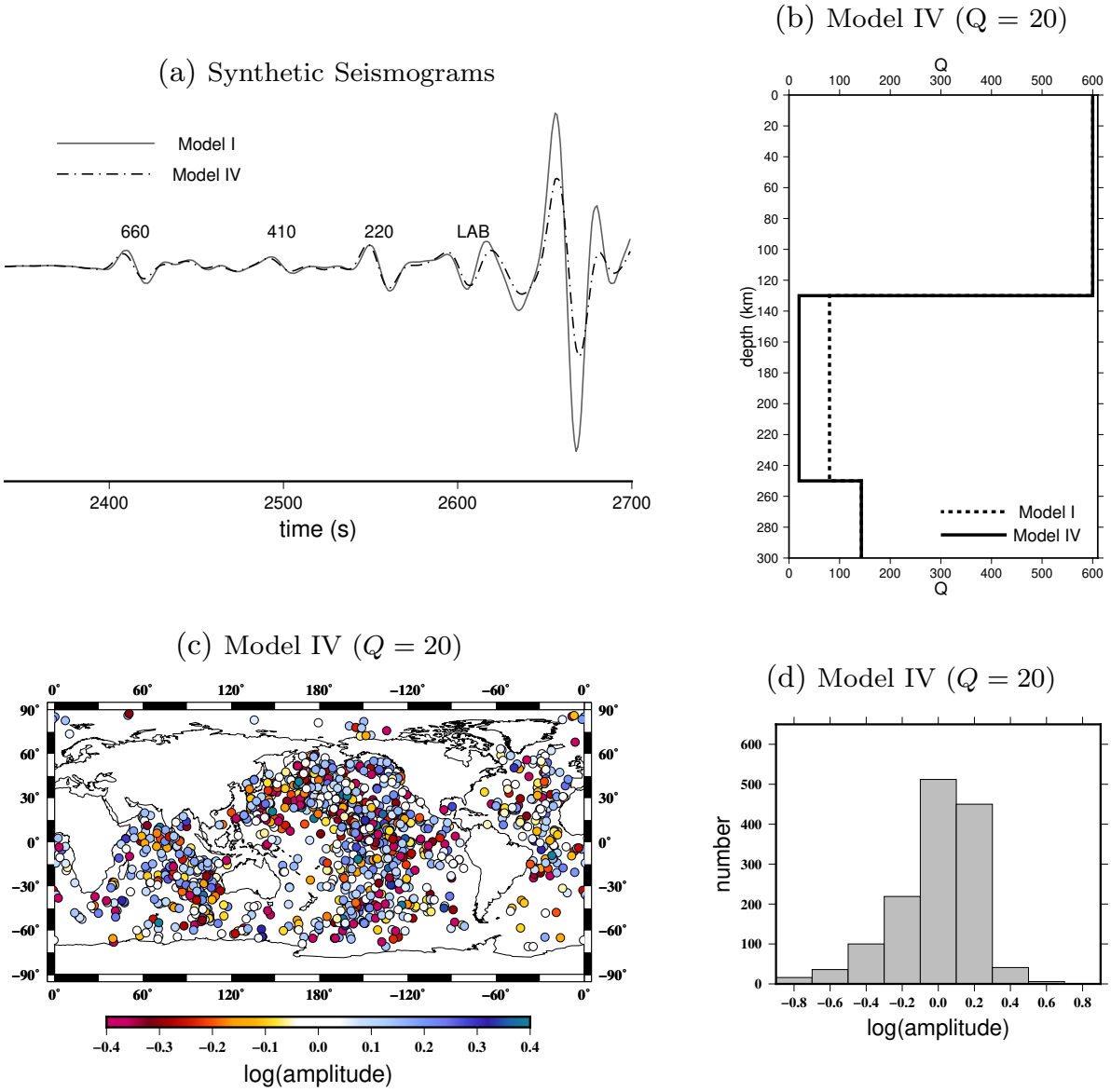

Figure 2.10: (a) Synthetic seismograms calculate for Model I and Model IV as in Figure 2.3. (b) Q structure in the 1-D reference models Model I and Model IV. Model IV is identical to Model I in velocity and density but has a much smaller Q value (Q=20) in the asthenosphere than in Model I (Q=80). The amplitude of the main SS wave becomes smaller in Model IV synthetics due to the overall stronger attenuation associated with the lower Q value in the asthenosphere but its impact on the amplitude of the SS precursor $S_{\rm LAB}S$ is very limited. This is because anelasticity also reduces the effective wave speed in the low Q region. Therefore, velocity contrast across the LAB increases, resulting a larger reflection coefficient which increases the amplitude of the $S_{\rm LAB}S$ wave. The observed large amplitudes of the $S_{\rm LAB}S$ waves therefore can not be fully explained by a reduction of Q values in the asthenosphere.

Bibliography

[1] Sun, S. & Zhou, Y. Age-independent oceanic plate thickness and asthenosphere melting from ss precursor imaging. *Journal of Geophysical Research: Solid Earth* **128**, e2022JB024805 (2023).

[2] Fischer, K. M., Ford, H. A., Abt, D. L. & Rychert, C. A. The lithosphere-asthenosphere boundary. *Annual Review of Earth and Planetary Sciences* **38**, 551–575 (2010).

[3] Fischer, K. M. *et al.* A comparison of oceanic and continental mantle lithosphere. *Physics of the Earth and Planetary Interiors* 106600 (2020).

[4] Gaherty, J. B. & Jordan, T. H. Lehmann discontinuity as the base of an anisotropic layer beneath continents. *Science* **268**, 1468–1471 (1995).

[5] Karato, S.-i. On the lehmann discontinuity. *Geophysical Research Letters* **19**, 2255–2258 (1992).

[6] Kawakatsu, H. & Utada, H. Seismic and electrical signatures of the lithosphere–asthenosphere system of the normal oceanic mantle. *Annual Review of Earth and Planetary Sciences* **45** (2017).

[7] Rychert, C. A., Schmerr, N. & Harmon, N. The pacific lithosphere-asthenosphere boundary: Seismic imaging and anisotropic constraints from ss waveforms. *Geochemistry, Geophysics, Geosystems* **13** (2012).

[8] Rychert, C. A., Harmon, N., Constable, S. & Wang, S. The nature of the lithosphere-asthenosphere boundary. *Journal of Geophysical Research: Solid Earth* **125**, e2018JB016463 (2020).

[9] Parsons, B. & Sclater, J. G. An analysis of the variation of ocean floor bathymetry and heat flow with age. *Journal of geophysical research* **82**, 803–827 (1977).

[10] Richards, F., Hoggard, M., Crosby, A., Ghelichkhan, S. & White, N. Structure and dynamics of the oceanic lithosphere-asthenosphere system. *Physics of the Earth and Planetary Interiors* 106559 (2020).

[11] Richter, F. M. Convection and the large-scale circulation of the mantle. *Journal of Geophysical Research* **78**, 8735–8745 (1973).

[12] Richter, F. M. & Parsons, B. On the interaction of two scales of convection in the mantle. *Journal of Geophysical Research* **80**, 2529–2541 (1975).

[13] Korenaga, T. & Korenaga, J. Subsidence of normal oceanic lithosphere, apparent thermal expansivity, and seafloor flattening. *Earth and Planetary Science Letters* **268**, 41–51 (2008).

[14] French, S., Lekic, V. & Romanowicz, B. Waveform tomography reveals channeled flow at the base of the oceanic asthenosphere. *Science* **342**, 227–230 (2013).

[15] Godfrey, K. E., Dalton, C. A. & Ritsema, J. Seafloor age dependence of rayleigh wave phase velocities in the indian ocean. *Geochemistry, Geophysics, Geosystems* **18**, 1926–1942 (2017).

[16] James, E. K., Dalton, C. A. & Gaherty, J. B. Rayleigh wave phase velocities in the a tlantic upper mantle. *Geochemistry, Geophysics, Geosystems* **15**, 4305–4324 (2014).

[17] Ma, Z. & Dalton, C. A. Evidence for dehydration-modulated small-scale convection in the oceanic upper mantle from seafloor bathymetry and rayleigh wave phase velocity. *Earth and Planetary Science Letters* **510**, 12–25 (2019).

[18] Maggi, A., Debayle, E., Priestley, K. & Barruol, G. Multimode surface waveform tomography of the pacific ocean: a closer look at the lithospheric cooling signature. *Geophysical Journal International* **166**, 1384–1397 (2006).

[19] Debayle, E., Bodin, T., Durand, S. & Ricard, Y. Seismic evidence for partial melt below tectonic plates. *Nature* **586**, 555–559 (2020).

[20] Rychert, C. A. & Shearer, P. M. Imaging the lithosphere-asthenosphere boundary beneath the pacific using ss waveform modeling. *Journal of Geophysical Research: Solid Earth* **116** (2011).

[21] Schmerr, N. The gutenberg discontinuity: Melt at the lithosphere-asthenosphere boundary. *Science* **335**, 1480–1483 (2012).

[22] Tharimena, S., Rychert, C., Harmon, N. & White, P. Imaging pacific lithosphere seismic discontinuities—insights from ss precursor modeling. *Journal of Geophysical Research: Solid Earth* **122**, 2131–2152 (2017).

[23] Kawakatsu, H. *et al.* Seismic evidence for sharp lithosphere-asthenosphere boundaries of oceanic plates. *Science* **324**, 499–502 (2009).

[24] Li, X. *et al.* Mapping the hawaiian plume conduit with converted seismic waves. *Nature* **405**, 938–941 (2000).

[25] Li, X., Kind, R., Yuan, X., Wölbern, I. & Hanka, W. Rejuvenation of the lithosphere by the hawaiian plume. *Nature* **427**, 827–829 (2004).

[26] Rychert, C. A. & Shearer, P. M. A global view of the lithosphere-asthenosphere boundary. *Science* **324**, 495–498 (2009).

[27] Mehouachi, F. & Singh, S. C. Water-rich sublithospheric melt channel in the equatorial atlantic ocean. *Nature Geoscience* **11**, 65–69 (2018).

[28] Stern, T. *et al.* A seismic reflection image for the base of a tectonic plate. *Nature* **518**, 85–88 (2015).

[29] Turcotte, D. & Oxburgh, E. Finite amplitude convective cells and continental drift. *Journal of Fluid Mechanics* **28**, 29–42 (1967).

[30] Faul, U. H. & Jackson, I. The seismological signature of temperature and grain size variations in the upper mantle. *Earth and Planetary Science Letters* **234**, 119–134 (2005).

[31] Auer, L., Becker, T. W., Boschi, L. & Schmerr, N. Thermal structure, radial anisotropy, and dynamics of oceanic boundary layers. *Geophysical Research Letters* **42**, 9740–9749 (2015).

[32] Beghein, C., Yuan, K., Schmerr, N. & Xing, Z. Changes in seismic anisotropy shed light on the nature of the gutenberg discontinuity. *Science* **343**, 1237–1240 (2014).

[33] Karato, S.-i. & Wu, P. Rheology of the upper mantle: A synthesis. *Science* **260**, 771–778 (1993).

[34] Karato, S.-i. On the origin of the asthenosphere. *Earth and Planetary Science Letters* **321**, 95–103 (2012).

[35] Yamauchi, H. & Takei, Y. Polycrystal anelasticity at near-solidus temperatures. *Journal of Geophysical Research: Solid Earth* **121**, 7790–7820 (2016).

[36] Dziewonski, A. M. & Anderson, D. L. Preliminary reference earth model. *Physics of the earth and planetary interiors* **25**, 297–356 (1981).

[37] Hales, A., Muirhead, K. & Rynn, J. A compressional velocity distribution for the upper mantle. *Tectonophysics* **63**, 309–348 (1980).

[38] Lehmann, I. Velocities of longitudinal waves in the upper part of the earth's mantle. In *Annales de géophysique*, vol. 15, 93 (1959).

[39] Lehmann, I. S and the structure of the upper mantle. *Geophysical Journal International* **4**, 124–138 (1961).

[40] Goncz, J. H. & Cleary, J. R. Variations in the structure of the upper mantle beneath australia, from rayleigh wave observations. *Geophysical Journal International* **44**, 507–516 (1976).

[41] Revenaugh, J. & Jordan, T. H. Mantle layering from scs reverberations: 3. the upper mantle. *Journal of Geophysical Research: Solid Earth* **96**, 19781–19810 (1991).

[42] Sacks, I., Snoke, J. & Husebye, E. Lithosphere thickness beneath the baltic shield. *Tectonophysics* **56**, 101–110 (1979).

[43] Vidale, J. E. & Benz, H. M. Upper-mantle seismic discontinuities and the thermal structure of subduction zones. *Nature* **356**, 678–683 (1992).

[44] Deuss, A. & Woodhouse, J. H. A systematic search for mantle discontinuities using ss-precursors. *Geophysical Research Letters* **29**, 90–1 (2002).

[45] Deuss, A. & Woodhouse, J. H. The nature of the lehmann discontinuity from its seismological clapeyron slopes. *Earth and Planetary Science Letters* **225**, 295–304 (2004).

[46] Gu, Y. J., Dziewonski, A. M. & Ekström, G. Preferential detection of the lehmann discontinuity beneath continents. *Geophysical Research Letters* **28**, 4655–4658 (2001).

[47] Schmerr, N. & Garnero, E. Investigation of upper mantle discontinuity structure beneath the central pacific using ss precursors. *Journal of Geophysical Research: Solid Earth* **111** (2006).

[48] Shearer, P. M. Constraints on upper mantle discontinuities from observations of long-period reflected and converted phases. *Journal of Geophysical Research: Solid Earth* **96**, 18147–18182 (1991).

[49] Turcotte, D. L. & Schubert, G. *Geodynamics* (Cambridge university press, 2002).

[50] Guo, Z. & Zhou, Y. Finite-frequency imaging of the global 410-and 660-km discontinuities using ss precursors. *Geophysical Journal International* **220**, 1978–1994 (2020).

[51] Guo, Z. & Zhou, Y. Stagnant slabs and their return flows from finite-frequency tomography of the 410-km and 660-km discontinuities. *Journal of Geophysical Research: Solid Earth* **126**, e2020JB021099 (2021).

[52] Liu, K. & Zhou, Y. Travelling-wave green tensor and near-field rayleigh-wave sensitivity. *Geophysical Supplements to the Monthly Notices of the Royal Astronomical Society* **205**, 134–145 (2016).

[53] Dziewonski, A. M., Chou, T.-A. & Woodhouse, J. H. Determination of earthquake source parameters from waveform data for studies of global and regional seismicity. *Journal of Geophysical Research: Solid Earth* **86**, 2825–2852 (1981).

[54] Ekström, G., Nettles, M. & Dziewoński, A. The global cmt project 2004–2010: Centroid-moment tensors for 13,017 earthquakes. *Physics of the Earth and Planetary Interiors* **200**, 1–9 (2012).

[55] USGS. Preliminary determination of epicenters (PDE) bulletin: US Geological Survey. *US Geological Survey Earthquake Hazards Program* (2017).

[56] Xue, J., Zhou, Y. & Chen, Y. J. Tomographic resolution of plume anomalies in the lowermost mantle. *Geophysical Journal International* **201**, 979–995 (2015).

[57] Deng, K. & Zhou, Y. Wave diffraction and resolution of mantle transition zone discontinuities in receiver function imaging. *Geophysical Journal International* **201**, 2008–2025 (2015).

[58] Zhou, Y. Multimode surface wave sensitivity kernels in radially anisotropic earth media. *Geophysical Journal International* **176**, 865–888 (2009).

[59] Zhou, Y., Dahlen, F., Nolet, G. & Laske, G. Finite-frequency effects in global surface-wave tomography. *Geophysical Journal International* **163**, 1087–1111 (2005).

[60] Dahlen, F. Finite-frequency sensitivity kernels for boundary topography perturbations. *Geophysical Journal International* **162**, 525–540 (2005).

[61] Laske, G., Masters, G., Ma, Z. & Pasyanos, M. Update on crust1. 0—a 1-degree global model of earth's crust. In *Geophys. Res. Abstr*, vol. 15, 2658 (2013).

[62] Ritsema, J., Deuss, a. A., Van Heijst, H. & Woodhouse, J. S40rts: a degree-40 shear-velocity model for the mantle from new rayleigh wave dispersion, teleseismic traveltime and normal-mode splitting function measurements. *Geophysical Journal International* **184**, 1223–1236 (2011).

[63] Müller, R. D. *et al.* A global plate model including lithospheric deformation along major rifts and orogens since the triassic. *Tectonics* **38**, 1884–1907 (2019).

[64] Hammond, W. C. & Humphreys, E. D. Upper mantle seismic wave velocity: Effects of realistic partial melt geometries. *Journal of Geophysical Research: Solid Earth* **105**, 10975–10986 (2000).

[65] Chantel, J. *et al.* Experimental evidence supports mantle partial melting in the asthenosphere. *Science advances* **2**, e1600246 (2016).

[66] Team, T. M. S. Imaging the deep seismic structure beneath a mid-ocean ridge: The melt experiment. *Science* **280**, 1215–1218 (1998).

[67] Ni, H., Keppler, H. & Behrens, H. Electrical conductivity of hydrous basaltic melts: implications for partial melting in the upper mantle. *Contributions to Mineralogy and Petrology* **162**, 637–650 (2011).

[68] Karato, S.-i. & Jung, H. Water, partial melting and the origin of the seismic low velocity and high attenuation zone in the upper mantle. *Earth and Planetary Science Letters* **157**, 193–207 (1998).

[69] Burgos, G. *et al.* Oceanic lithosphere-asthenosphere boundary from surface wave dispersion data. *Journal of Geophysical Research: Solid Earth* **119**, 1079–1093 (2014).

[70] Nettles, M. & Dziewoński, A. M. Radially anisotropic shear velocity structure of the upper mantle globally and beneath north america. *Journal of Geophysical Research: Solid Earth* **113** (2008).

[71] Zhou, Y., Nolet, G., Dahlen, F. A. & Laske, G. Global upper-mantle structure from finite-frequency surface-wave tomography. *Journal of Geophys. Res.* **111**, doi:10.1029/2005JB003677 (2006).

[72] Rychert, C. A. *et al.* A dynamic lithosphere–asthenosphere boundary near the equatorial mid-atlantic ridge. *Earth and Planetary Science Letters* **566**, 116949 (2021).

[73] Wang, S., Constable, S., Rychert, C. A. & Harmon, N. A lithosphere-asthenosphere boundary and partial melt estimated using marine magnetotelluric data at the central middle atlantic ridge. *Geochemistry, Geophysics, Geosystems* **21**, e2020GC009177 (2020).

[74] Byrnes, J. S. *et al.* An upper mantle seismic discontinuity beneath the g alápagos a rchipelago and its implications for studies of the lithosphere-asthenosphere boundary. *Geochemistry, Geophysics, Geosystems* **16**, 1070–1088 (2015).

[75] Rost, S. & Weber, M. A reflector at 200 km depth beneath the northwest pacific. *Geophysical Journal International* **147**, 12–28 (2001).

[76] Holtzman, B. K. Questions on the existence, persistence, and mechanical effects of a very small melt fraction in the asthenosphere. *Geochemistry, Geophysics, Geosystems* **17**, 470–484 (2016).

Chapter 3

SS Precursor Imaging Reveals A Global Oceanic Asthenosphere Modulated by Sea-Floor Spreading

3.1 Introduction

A global discontinuity at a depth of about 220 km was first introduced in the Preliminary Reference Earth Model (PREM) in the 1980s as the base of the asthenosphere. This discontinuity has been reported in seismic studies in continental regions and also known as the Lehmann discontinuity [1, 2, 3, 4, 5, 6]. However, later studies suggested that this interface may not be a global feature as a reflection from this depth has been missing in long-period global stacks of seismograms [7, 8, 9, 10, 11]. In oceanic regions, seismic signals from this interface have only been reported sporadically and the global existence of an oceanic 220-km discontinuity remains enigmatic [12, 13, 14, 15, 16].

In this study, we investigate the existence of a lower asthenosphere boundary in the global oceans using seismic SS precursors, which are SS waves reflected off the underside of the 220-km discontinuity (hereinafter referred to as $S_{220}S$ waves). The SS precursors $S_{220}S$ are

most sensitive to the structure of the interface at the reflection points, which is about half way between the earthquake and the station. In general, SS precursors provide excellent data coverage in the global oceanic areas where seismic stations are sparse. Our seismic dataset include amplitude and arrival time measurements of SS precursors at a period of 25 seconds, measured on long-period transverse component seismograms recorded at GSN stations for large earthquakes occurred between 2009 and 2020 (Figure B.1).

We observe strong SS precursors reflected off the 220-km discontinuity across the global oceanic regions, including the Pacific ocean, the Indian Ocean and the Atlantic Oceans, regardless of the seafloor age (Figure 3.1). This is surprising especially that SS precursors reflected off mantle discontinuities are secondary waves, and their amplitudes are expected to be small. In addition, such a discontinuity at the base of the oceanic asthenosphere has been absent in global stacks. Nevertheless, strong SS precursors from this interface were observed on about 42% of the SS seismograms. In addition, The average amplitudes of the observed SS precursors are larger than the predicted amplitudes calculated for model PREM. This indicates a larger velocity contrast across the 220-km discontinuity in oceanic regions than that in the model PREM.

We measure the differential arrival times between SS waves and SS precursors $\delta t|_{S_{220}S} - \delta t|_{SS}$ based on observed and synthetic seismograms. Measurements made with respect to synthetics calculated using PREM as the reference model show that the distribution of traveltime measurements does not have a zero mean but has an average advance time of about 5 seconds, regardless of 3-D crustal and mantle corrections applied (Figure 3.2). This is not unexpected because PREM is a global average model, which does not necessary represent the average seismic structure in the global oceanic regions. In fact, it is known that there are

large differences between oceans and continents in their crustal and mantle structures. The overall early arrivals of $S_{220}S$ waves with respect to the PREM synthetics indicate that the S-wave speed above the discontinuity in oceanic regions is slower than that in model PREM, or the depth of the 220-km discontinuity is deeper than that in PREM, or a combination of both. Based on the traveltime measurements, we construct an oceanic 1-D reference model, model MOCE with the depth of the 220-km discontinuity at 250 km and S-wave speed in the asthenosphere slower than that in PREM (Figure 3.2 & Figure B.2). The calculated differential arrival times $\delta t|_{S_{220}S} - \delta t|_{SS}$ is centered at zero, indicating that model MOCE is a reasonable reference model for the global oceanic regions.

To quantify the velocity contrast across the interface, we calculate amplitude ratios $S_{220}S/S_{410}S$ and $S_{220}S/S_{660}S$ using observed seismograms when reference phases $S_{660}S$ and $S_{410}S$ phases can also be clearly identified. For comparison, the same ratios are also calculated for synthetic seismograms computed for reference models MOCE and PREM. We define the minimum amplitude ratios (γ) as $\gamma = \text{minimum}[\log(A_{S_{\text{LAB}}S}/A_{S_{410}S}), \log(A_{S_{\text{LAB}}S}/A_{S_{660}S})]$. The mean values of the minimum amplitude ratio γ calculated from the observed SS precursors is close to zero. This indicates that the observed $S_{220}S$ amplitudes in this dataset are roughly as large as the amplitudes of the $S_{410}S$ (or $S_{660}S$) waves. The calculated mean amplitude ratio γ for the final model MOCE is also close to zero, while the mean value of γ calculated for model PREM is about -0.2, meaning that on average the $S_{220}S$ amplitudes are only about 63% of the amplitudes of the $S_{410}S$ (or $S_{660}S$) waves. We conclude that the 7% velocity reduction across the 220-km discontinuity in model MOCE explain amplitude observations better than the 5% velocity reduction in model PREM (Figure 3.3).

To obtain the depths of the discontinuity in the global oceans, we use the differential travel-

times $\delta t|_{S_{220}S} - \delta t|_{SS}$ of the observed seismograms with respect to the synthetic seismograms calculated in model MOCE. 3-D crustal and mantle wavespeed corrections are applied using global crustal models CRUST1.0 [17] and S40RTS [18]. The mean values of the $\delta t|_{S_{220}S} - \delta t|_{SS}$ traveltime delays are roughly the same with or without wavespeed corrections, with both mean values close to zero (Figures 3.2 and B.3). This implies that the average velocity in the uppermost mantle in the reference model is close to the global average.

We calculate finite-frequency sensitivities of the arrival times to depth perturbations of the 220-km discontinuity based on travelling-wave mode coupling (Figure B.4), which fully account for source radiation patterns, interference of seismic waves arriving in the measurement window as well as seismogram windowing and tapering. We parameterize the global surface of the discontinuity using a set of spherical triangular grid points with a lateral spacing of about 4°, and solve the 2-D linear tomographic problem based on singular value decomposition (SVD). The optimal model obtained by tradeoff analysis (Figure B.5) based on data misfit and model norm is plotted in Figure 3.4.

3.2 Topography of the 220-km Discontinuity

The optimal model obtained from 2-D finite-frequency tomography of the $\delta t|_{S_{220}S} - \delta t|_{SS}$ traveltime measurements shows large depth variations of the 220-km discontinuity in oceanic regions, with perturbations locally up to ∼30 km. The variations are characterized by alternating (shallow and deep) bands of linear anomalies roughly following the longitude direction, parallel to the seafloor age contours. This suggests a fundamental connection between the asthenosphere boundary depth and seafloor spreading. However, perturbations in discontinuity depth show no apparent correlation with either seafloor age or spreading rate (Figures

3.4 and B.6). This indicates that the relation is more complex and a conclusion can not be drawn without further analysis of the spatial characteristics of the discontinuity, for example, the roughness of the of the 220-km discontinuity topography.

The average depth of the 220-km discontinuity obtained from this study is about 251.6 km in the global oceans. Reflectors at those depths have been reported in previous studies in oceanic regions [7]. The mean depth of the discontinuity is about 250 km for seafloors younger than 75 million years old, and it is about 252 km for older seafloors. In addition, there is increased variability in the older seafloors (Figure 3.4). The resolution is not uniform across the oceans, for example, the resolution of our model is relatively poor in the Southern Atlantic ocean and the Western Indian ocean (Figure B.7).

3.3 Boundary Roughness and Seafloor Spreading Rate

To quantify the characteristics of lateral variations in the 220-km discontinuity, we compute the surface Laplacian (roughness) of the discontinuity topography based on finite difference calculations, with the surface Laplacian operator defined as (D&T A.135),

$$\nabla_1^2 f = \frac{\partial^2 f}{\partial \theta^2} + \frac{\cos\theta}{\sin\theta}\frac{\partial f}{\partial \theta} + \frac{1}{\sin^2\theta}\frac{\partial^2 f}{\partial \phi^2}, \tag{3.1}$$

where $f(\theta, \phi)$ is the depth of the 220-km discontinuity, with θ and ϕ being the colatitude and longitude, respectively. The surface roughness the 220-km discontinuity is plotted in Figure 3.5.

The most striking feature on the roughness of the 220-km discontinuity is the apparent ge-

ographic correlation between the boundary roughness (Figure 3.5a) and the spreading rates of the seafloor (Figure 3.4c), both following the seafloor age contours. For example, in the Pacific, spreading rates are the greatest (over 15 cm/year) at the youngest East Pacific Rise as well as the 130-million years seafloors in the Western Pacific, and largest asthenosphere boundary roughness are also observed in those regions. It is worth noting that the model resolution of the asthenosphere boundary is not uniform across the oceans due to limited data coverage, and we will focus our analysis on well-resolved regions with the diagonal elements of the resolution matrix greater than 0.25 (Figure B.7).

The correlation between the roughness of the discontinuity and the sea-floor spreading rate does not appear to be linear across all oceans. In particular, spreading rates in the Atlantic ocean are overall small but the roughness of the 220-km discontinuity are relatively large in the mid Atlantic, indicating that the correlation may be different for different oceans. To further investigate the correlation, we calculate the maximum asthenosphere boundary roughness for seafloors in every $5^\circ \times 5^\circ$ degree cells over the global oceans (Figure 3.5c). The average values in every 10 mm/year spreading rate interval is plotted in Figure 3.5d. The plots show clearly two distinctly different regimes in the relation between boundary roughness and sea-floor spreading rates. For slow-spreading seafloors (less than 40 mm/yr), the roughness increases rapidly with spreading rate (Figures 3.5, 3.6 and B.8), and it reaches a level similar to the roughness of the fast-spreading seafloors at a rate of about 40 mm/yr. For fast-spreading seafloors, the roughness in general increases with spreading rates, but the increase is much more gradual compared to the slow-spreading sea floors and it also shows considerable fluctuations. For example, the roughness of the seafloors with spreading rates between 80 and 100 mm/year is overall larger than seafloors with spreading rates between 40 and 70 mm/year, but there is no increase (but slight decrease) in boundary roughness

from 80 mm/year to 100 mm/year. The two distinctly different regimes in roughness and spreading-rates relation can be clearly observed at all length scales when seafloor and boundary roughness maps are filtered to different length scales (Figure B.9). There is only a weak positive correlation between the 220-km roughness and seafloor age (Figure 3.5) and spreading rate generally remains constant at different seafloor ages (Figure B.10).

3.4 Seafloor Spreading and Asthenosphere Convection

It has been long recognized that seafloor spreading plays an important role in plate tectonics, but the time scale and depth extent of its influence on upper-mantle convection remains poorly understood. In addition to strong SS precursors reflected off the 220-km discontinuity across the global oceanic regions, we have observed a strong correlation between the roughness of the discontinuity and the spreading rate of the seafloor. In general, the base of the asthenosphere is smoother under slow-spreading seafloors than fast-spreading seafloors, but the boundary roughness increases very rapidly with spreading rate until the the spreading rates reaches about 40 mm/yr. This suggests that convections in the asthenosphere is closely related to the formation of the oceanic plates at the spreading centers.

If we assume that convection in the asthenosphere is controlled largely by the thermal and viscosity structure of the lithosphere and the asthenosphere, the differences in the 220-km discontinuity roughness would indicate variations in the thermal and compositional structure associated with the formation of the oceanic plates, which often involves magnetism and mechanical extension at the spreading centers. The relative importance of the two processes vary considerably depending on the seafloor spreading rate. At fast-spreading centers,

the oceanic crust formed by decompression melting of the upwelling mantle has a relatively homogeneous and layered structure due to continuous magma injection and the existence of a perennial magma chamber [19, 20, 21]. The fast-spreading ridges are usually characterized by smooth topography [22]. It has been suggested that differences in spreading rates also introduce variations in composition due to distinct processes in chemical differentiation. The extent of mantle melting increases with increasing spreading rate [23] and magnetism becomes the dominant process at fast spreading centers. At fast spreading ridges, magma chambers are typically shallower, and thus subjected to more significant cooling, leading to a higher degree of differentiation. On the other hand, slow spreading centers are characterized by hotter and deeper magma, resulting in reduced levels of chemical differentiation in the newly formed crust [24].

Mechanical deformation is far more important at the slow spreading centers than at fast spreading centers [25]. In particular, slow spreading ridges are characterized by deep axial rift valleys and intense normal faulting, with low-angle detachment faults extending to the upper mantle [26, 27, 28, 29, 30, 31]. This is different from fast-spreading centers where the development of faults is limited and only extends to a shallower depth in the crust [28]. The fault zones developed by mechanical extension at slow-spreading centers will influence the thermal property of the lithosphere, as those faults are major conduits for the penetration of cooling water into the lithosphere. The broken morphology of the slow spreading centers allows for circulation of fluids and well-developed serpentinization as peridotite react with seawater. Serpentinization affect the thermal properties of the lithosphere. This is because serpentine minerals have lower thermal conductivity than peridotite, which make the lithosphere less effective in conducting heat out of the asthenosphere. As the seafloor slowly moves away from the spreading centers, gradual dehydration of serpentine through hydrogen

diffusion beneath slow-spreading seafloors may release water which will reduce the viscosity of the asthenosphere.

3.5 Conclusions

In contrast to previous studies based on SS precursor stacking, we have observed strong SS precursors reflected off the 220-km discontinuity throughout the global oceanic regions. We interpret the strong reflector as the base of the oceanic asthenosphere, possibly associated with partial melting. The large amplitudes of the SS precursors ($S_{220}S$) can be explained by ∼7% velocity change across a first-order discontinuity at a depth of about 250 km, which indicates about 1% of partial melt in the asthenosphere based on finite element calculations for shear modulus reduction [32] and recent experimental results [33]. The 220-km discontinuity has a mean depth of ∼ 250 km with a lateral perturbation up to ∼30 km. The depth perturbations closely follow the seafloor age contours, indicating a fundamental connection between seafloor spreading and mantle convection in the asthenosphere.

In addition to the global existence of a lower asthenosphere boundary, the analysis on the topography of the boundary reveals a smoother asthenosphere base under seafloors formed at slow-spreading centers. Moreover, the roughness of this boundary increases rapidly with spreading rate until it reaches about 40 mm/year. In contrast, under seafloors with spreading rates exceeding 40 mm/year, the roughness of the discontinuity increases only gradually with spreading rates. This difference indicates a connection between asthenosphere boundary roughness and oceanic plate formation processes. The dominant process at fast spreading centers is magmatism, while structural extension plays an important role at slow-spreading centers. This produces oceanic plates with different thermal, compositional, and deforma-

tion structures. It has been suggested that variations in lithospheric structure may explain variations in mantle melting [34]. One possible mechanism that may explain the apparent correlation between the roughness of the 220-km discontinuity and the spreading rates of oceanic plates is that serpentinization in the oceanic lithosphere affect the dynamics of asthenospheric convections. At slow-spreading centers, the faulted morphology allows for fluid circulation and serpentinization, which reduces the thermal conductivity of the lithosphere. As the lithosphere moves away from the spreading center, gradual dehydration of serpentine through hydrogen diffusion may release water, further reducing the viscosity of the asthenosphere beneath the lithosphere. The differences in melting, cooling, mechanical extension and metamorphism at sea-floor spreading centers leave permanent imprints in the chemical compositions and physical properties of the lithosphere plate, introducing a long lasting influence on upper mantle convection, millions of year after the plates have moved away from the spreading centers.

3.6 Data & Methods

We investigate the 220-km discontinuity in the global oceanic regions using SS precursors on long-period transverse component seismograms. The horizontal-component seismograms were recorded at 144 GSN stations for 459 earthquakes that occurred between 2009 and 2020. The moment magnitude of the earthquake varies between 6.0 and 8.0. The seismograms are rotated to radial and transverse directions and then band-pass filtered between 10 and 80 mHz. A total number of 32,369 transverse component seismograms have SS wave bounce points in oceanic regions are processed (Figure 3.1a). The final dataset include 6,506 seismograms that have strong SS waves with simple source time functions. SS precursors are secondary waves and therefore their amplitudes are small, which makes it challenging

to identify them on many seismograms. They are often below the noise level due to weak source radiation, small reflection coefficient as well as defocusing caused by mantle heterogeneities. Nevertheless, strong SS precursors are observed on 2,754 seismograms recorded at 144 stations for 459 earthquakes (Figure B.1). The majority of the SS precursors (1,906 out of 2,754) have focal depths shallower than 50 km. Their epicentral distances range from 76° to 177° with the majority (2494 out of 2754) larger than 100°.

The observed SS precursors $S_{220}S$ are often characterized by large amplitudes, which was unexpected. The amplitudes of the $S_{220}S$ phases are similar in magnitude to the $S_{410}S$ and $S_{660}S$ phases, which are SS reflected off the mantle transition zone discontinuities, roughly at 410 and 660 km depths. The observation of robust SS precursors reflected at the 220-km discontinuity across the global oceanic regions presents a challenge to earlier observations because this phase has been reported to be largely absent in earlier oceanic seismic studies, in which seismograms are stacked to enhance the signal-to-noise ratios. One possible explanation to the absence of a coherent reflection from the 220-km discontinuity in the global stacks is that local variations in its depth is so large that no coherent reflections could be formed due to phase equalization [9, 11]. For instance, a strong 220-km discontinuity topography of tens of kilometers has been observed beneath the northwestern Pacific in a short-period array study [13]. When stacking is applied to SS precursors with reflection points in regions where large depth variations occur over very short distances, The amplitude of the SS precursors could be effectively minimized when stacking is applied to signals with non-coherent arrivals of the $S_{220}S$ waves (Figure B.11). In Figure B.11, we show a simple example to illustrate the concept of phase cancellation – the presence of significant fluctuations in SS precursor amplitudes and arrival times can lead to absence or amplitude reduction of the SS precursor in the stacking results.

To constrain the velocity reduction across the 220-km discontinuity that can explain the observed large amplitudes of the SS precursors, we construct a 1-D reference model MOCE, which is modified from PREM to include a large velocity increase at the depth of 250 km (Figure 3.2). A large velocity decrease at 130 km is also included in model MOCE. It has been proposed that this discontinuity represents the lithosphere asthenosphere boundary (LAB) in oceanic regions (Sun & Zhou 2023) and SS precursors $S_{\mathrm{LAB}}S$ observed in this study show large amplitudes that can be modeled by reflections off the LAB discontinuity in model MOCE. Synthetic seismograms are calculated for model MOCE based on traveling-wave mode summation. The global Centroid-Moment-Tensor (CMT) solutions and the USGS Preliminary Determination of Epicenters (PDE) source locations and origin times are used in the calculations of the synthetic seismograms. The synthetic seismograms are filtered using the same bandpass filter as applied to the observed seismograms.

We measure the differential delay times between the SS waves and their precursors $S_{220}S$ in the frequency domain at a period of 25 seconds (Figure B.4). The use of differential traveltimes minimizes measurement uncertainties associated with source parameters such as the earthquake origin times. The length of the measurement windows for SS wave varies from 47 to 157 seconds, while the length of the measurement windows for $S_{220}S$ waves ranges from 34 to 78 seconds. We apply 3-D crust and mantle wave speed corrections to the traveltime measurements using a global crustal model CRUST1.0 [17] and a global mantle model S40RTS [18]. The mean $\delta t|_{S_{220}S}$-$\delta t|_{SS}$ traveltime delay before and after the corrections remains approximately the same (Figure 3.2 and Figure B.3). This indicates that the average velocity in the uppermost 250 km in the reference model MOCE is close to the global average (Figure 3.2).

3.6.1 2-D Finite-Frequency Tomography

To image the depth perturbations of the 220-km discontinuity, we calculate the finite-frequency sensitivities of SS precursor traveltime measurements to boundary depth perturbations based on Born (single-scattering) approximation. The synthetic seismograms in 1-D reference earth models and the Born sensitivity kernels are computed in the frame work of travelling-wave mode coupling [35, 36]. The finite-frequency sensitivity kernels accounts for first-order wave diffraction effects and therefore allow us to image small scale features (in the order of a couple hundred kilometers) that are not resolvable in traditional ray-theory based methods. Based upon Born scattering approximation, travel time measurements can be expressed as a two-dimensional integration over depth perturbations over the global surface,

$$\delta t(\omega) = \iint_{\Sigma} K_{\Sigma}(\mathbf{x}, \omega)\, \delta d(\mathbf{x})\, d\Sigma, \tag{3.2}$$

where $K_{\Sigma}(\mathbf{x}, \omega)$ is the sensitivity of a traveltime measurement at angular frequency ω to depth perturbations $\delta d(\mathbf{x})$ of the corresponding seismic discontinuity. The boundary sensitivity kernels fully account for source radiation patterns, interference of seismic waves arriving in the measurement window as well as seismogram windowing and tapering. It is important to emphasize that the sensitivity kernels are associated with measurement windows which automatically account for all possible phases arriving within a measurement time window. They are applied to identify potential phase interferences in the measurement windows, for example, the topside reflections $S_{660}sS$ (Figure B.12). Those sensitivity kernels under phase interferences present abnormally large or small values (e.g., Figure B.12) which are excluded from the dataset.

We parameterize the surface of the Earth using a set of spherical triangular grid points.

The spherical triangles are 16-fold, with 2562 vertices and a lateral spacing of about 4.3°. The depth perturbations within any spherical triangle can be determined by linear interpolation of perturbations at the three vertices of the associated spherical triangle. This model parametrization allows us to write the linear tomographic problem in eq. (4.1) as

$$\mathbf{A}\mathbf{x} = \mathbf{b} \tag{3.3}$$

where $\mathbf{A}$ is the kernel matrix, $\mathbf{x}$ denotes the unknown depth perturbations of the 220-km discontinuity and $\mathbf{b}$ is the differential traveltime $\delta t|_{S_{220}S} - \delta t|_{SS}$.

The tomographic inverse problem is ill-posed and we solve a least square inverse problem

$$\mathbf{A}^T\mathbf{A}\mathbf{x} - \mathbf{A}^T\mathbf{b} = 0 \tag{3.4}$$

to find a model that minimizes the sum of the squared differences between the observed traveltimes and model predictions based on single-value decomposition (SVD) [37, 38]. In SVD, the symmetric matrix $\mathbf{A}^T\mathbf{A}$ can be decomposed as

$$\mathbf{A}^T\mathbf{A} = \mathbf{U}\mathbf{\Sigma}\mathbf{U}^T \tag{3.5}$$

and the solution to the least-square inverse problem can be written as

$$\mathbf{x} = \sum_i^N \frac{\mathbf{u}_i{}^{\mathrm{T}}\left(\mathbf{A}^{\mathrm{T}}\mathbf{b}\right)}{\sigma_i}\mathbf{u}_i \tag{3.6}$$

where σ_i is the ith largest singular value, and $\mathbf{u}_i$ is the associated singular vector. Because the inverse problem is ill posed, the solution is regularized by leaving out insignificant sin-

gular vectors whose associated singular values are small, and the summation is over the first N largest singular vectors. The optimal value of N is determined by analyzing the tradeoff between data misfit and model norm (Figure B.5). The depth and roughness maps of the 220-km discontinuity calculated before and after the 3-D crust and mantle corrections are shown in Figures 3.4, 3.5 and B.3. Overall, they show very similar structures. This is not unexpected as double differential traveltimes are used in this study, which minimizes the effects of wavespeed perturbations in the bulk mantle.

The associated resolution matrix of the optimal model can be calculated from the singular vectors,

$$\mathbf{R} = \mathbf{U}_N \mathbf{U}_N^{\mathrm{T}} \tag{3.7}$$

where the columns of matrix $\mathbf{U}_N$ are the singular vectors summed in eq. (3.6). The resolution of the model (diagonal elements of the matrix $\mathbf{R}$) are plotted in Figure B.7.

3.6.2 Amplitudes of SS Precursors

To quantify the velocity contrast across the 220-km discontinuity, we measure the amplitudes of the $S_{220}S$ waves as well as the reference waves $S_{410}S$ and $S_{660}S$, all at a period of 25 seconds. The measurements are made in the frequency domain using a 40-second window centered at the arrival of the SS precursors. Amplitude ratios $S_{220}S/S_{410}S$ and $S_{220}S/S_{660}S$ are calculated for the observed datasets as well as synthetic seismograms calculated in 1-D reference Earth models, MOCE and PREM. For each observed and synthetic seismogram, we calculate the minimum amplitude ratio $\gamma = \text{minimum}[\log(S_{220}S/S_{410}S), \log(S_{220}S/S_{660}S)]$. The mean value of the minimum amplitude ratio γ is close to zero for both the observed SS precursors and synthetic SS precursors calculated for model MOCE (Figure 3.3). A γ

value of zero indicates that the amplitudes of the $S_{220}S$ waves are roughly as large as the amplitudes of the $S_{410}S$ (or $S_{660}S$) waves. The mean value of the minimum amplitude ratio γ calculated for PREM is about about -0.2, indicating that the average $S_{220}S$ amplitude is much smaller in model PREM, the average amplitudes of the $S_{220}S$ is about 63% of the amplitudes of the $S_{410}S$ (or $S_{660}S$) waves.

In addition to the SS precursors reflected off the 220-km discontinuity, we also observe strong SS precursors reflected at the lithosphere-asthenosphere boundary (LAB), $S_{\mathrm{LAB}}S$. The amplitudes of the $S_{\mathrm{LAB}}S$ waves are comparable to the amplitudes of the $S_{410}S$ and $S_{660}S$ waves (Figure B.13). This observation is consistent with the recent study of Sun & Zhou (2023) in which they observe strong LAB reflections across the global oceans. The 12% velocity reduction across the LAB in model MOCE can explain the observed amplitudes of the $S_{\mathrm{LAB}}S$ phases reasonably well.

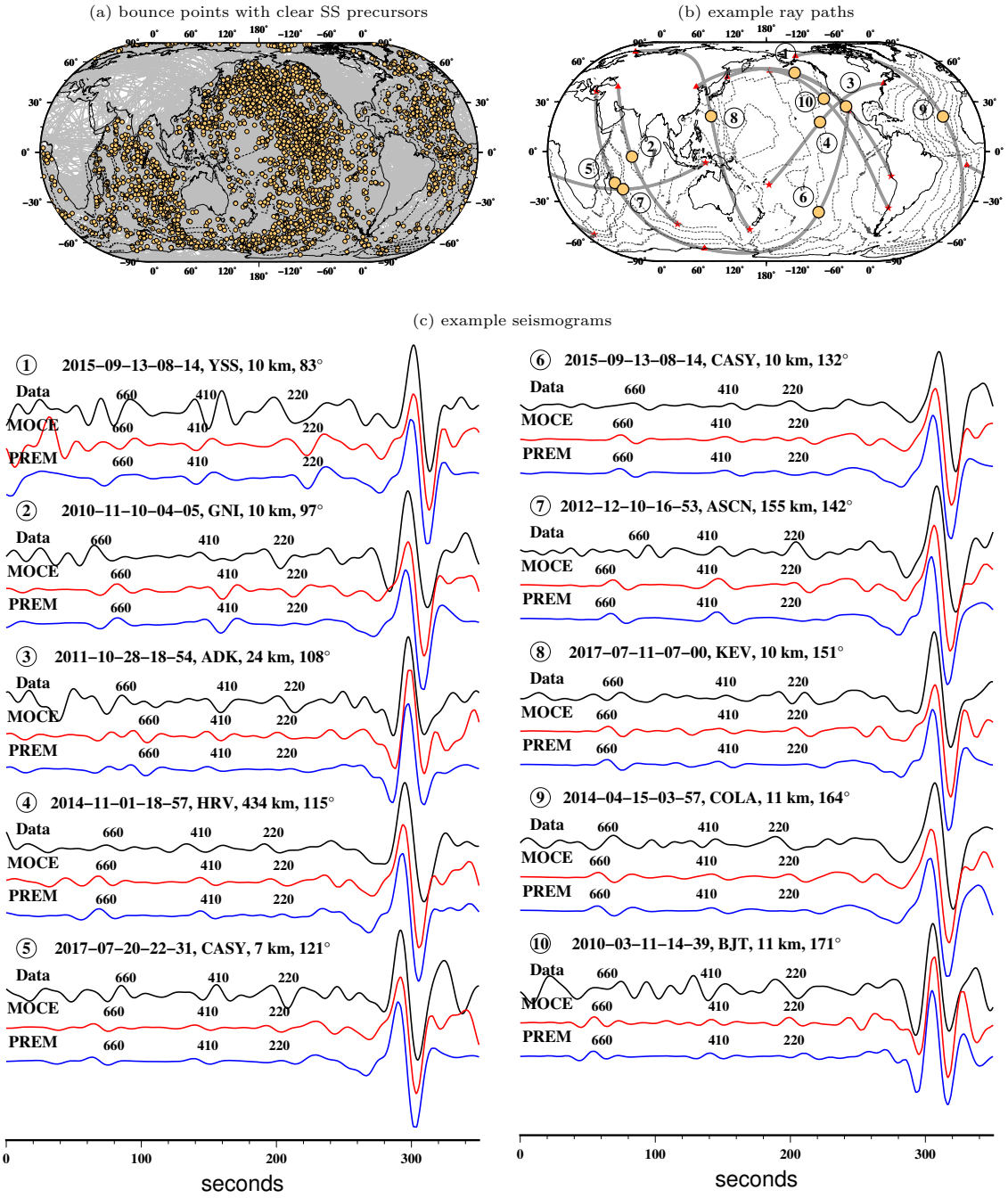

Figure 3.1: **(a)** geographic ray paths (gray lines) and bounce points (orange dots) of the SS precursors ($S_{220}S$) used in this study. **(b)** bounce points and ray paths for example seismograms plotted in **(c)**. **(c)** example transverse-component seismograms with $S_{220}S$ phases. The epicentral distance ranges from 80° to 180°. The black seismograms are data, the red seismograms are synthetics calculated in a reference 1-D model MOCE with 7% of the velocity jump across the 220-km discontinuity, and the blue synthetics are calculated in PREM in which the velocity increases is 5% across the discontinuity. Model MOCE and PREM are plotted in Figure 3.2. The seismograms have been band-pass filtered between 10 and 80 mHz and aligned using their SS arrivals for better illustration. The arrivals of the $S_{410}S$ and $S_{660}S$ waves are also labeled for reference. Station name, earthquake event date/time, depth and epicentral distance are denoted. Seafloor age contours (10, 50, 90, 130 and 170 Ma) in dashed black lines.

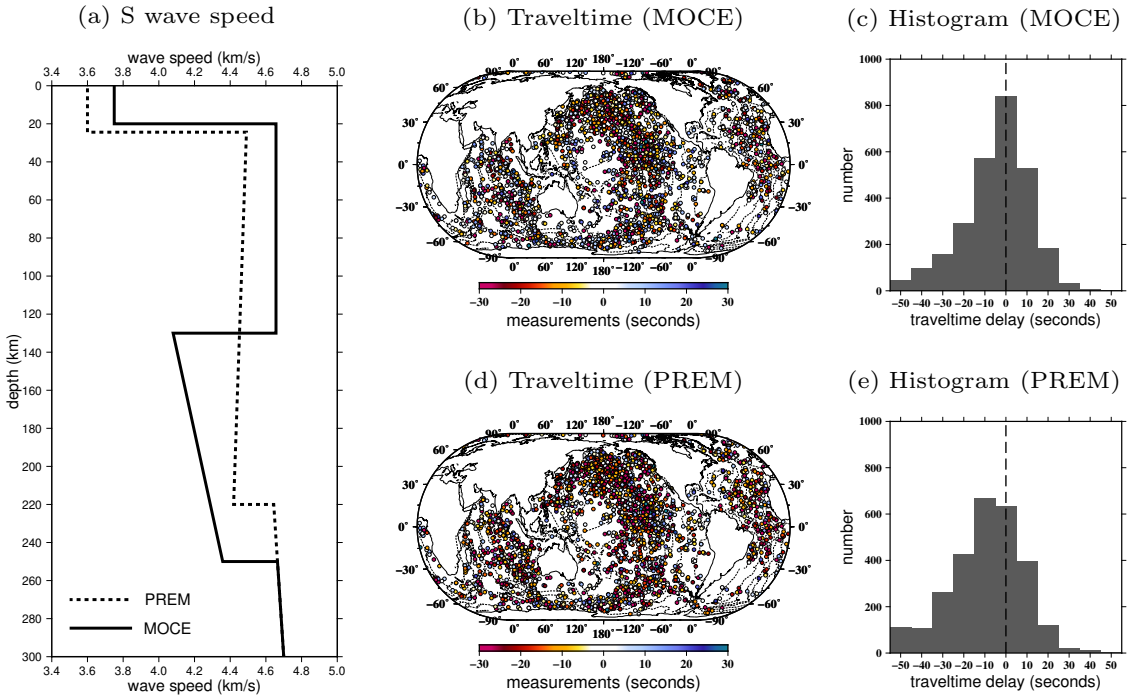

Figure 3.2: **(a)** S-wave speed profiles in model MOCE (solid black line) and model PREM (dotted black line). There is $\sim 5\%$ velocity increase across the 220-km discontinuity in mode PREM. Model MOCE is revised from PREM model and it incorporates two discontinuities at 250 km and 130 km with velocity contrasts of 7% and 12%, respectively, to represent the 220-km discontinuity and the lithosphere asthenosphere boundary (LAB), respectively. **(b)** and **(c)** are $\delta t|_{S_{220}S} - \delta t|_{SS}$ traveltimes of the 2754 data calculated for model MOCE after crustal and mantle corrections plotted in mapview and histogram. Seafloor age contours are plotted in dash, black lines at 10, 50, 90, 130 and 170 Ma. **(d)** and **(e)** are the same with **(b)** and **(c)**, respectively, but for model PREM. The average of $\delta t|_{S_{220}S} - \delta t|_{SS}$ traveltimes in model MOCE is close to 0, while that in model PREM is $\sim$ -5 seconds.

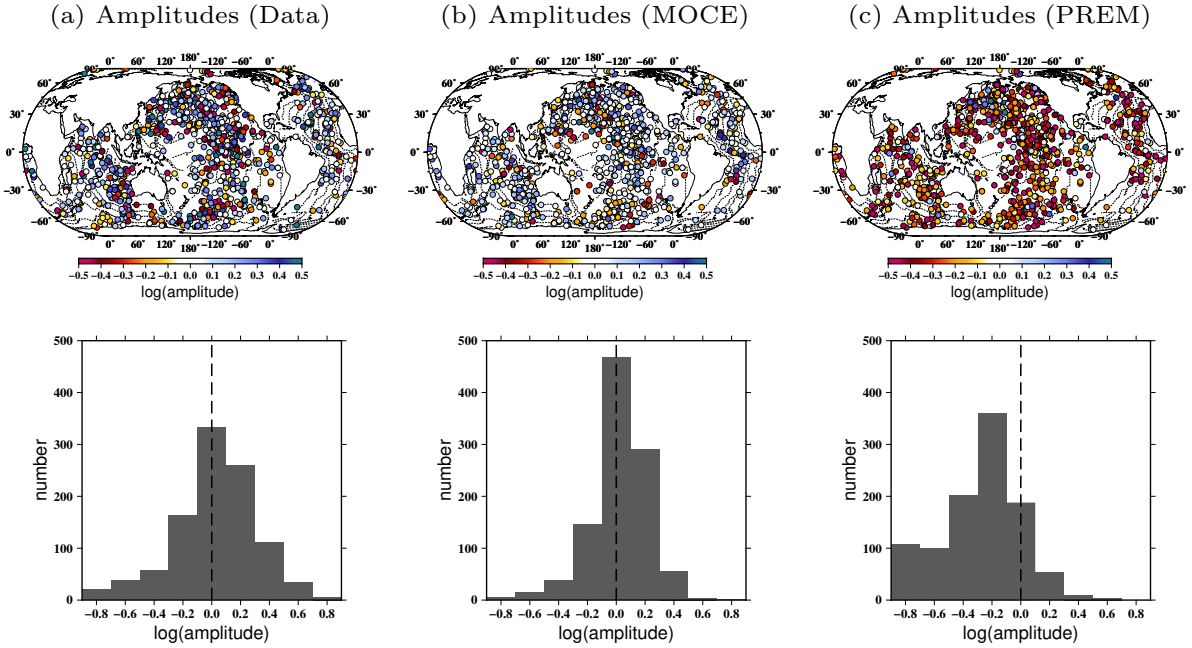

Figure 3.3: **Amplitude measurements of $S_{220}S$ waves. (a)**, amplitude measurements of 2754 sets of observed $S_{220}S$ waves in data calculated as γ= minimum [log ($A_{S_{\rm LAB}S}$ /$A_{S_{410}S}$), log($A_{S_{\rm LAB}S}$ /$A_{S_{660}S}$)] plotted in mapview (top) and histogram (bottom), respectively. **(b)** and **(c)**, the same with **(a)** but for model MOCE and model PREM, respectively. The mean amplitudes of observed $S_{220}S$ waves are roughly consistent with that of the synthetic $S_{220}S$ waves in model MOCE, both of which are larger than that in model PREM.

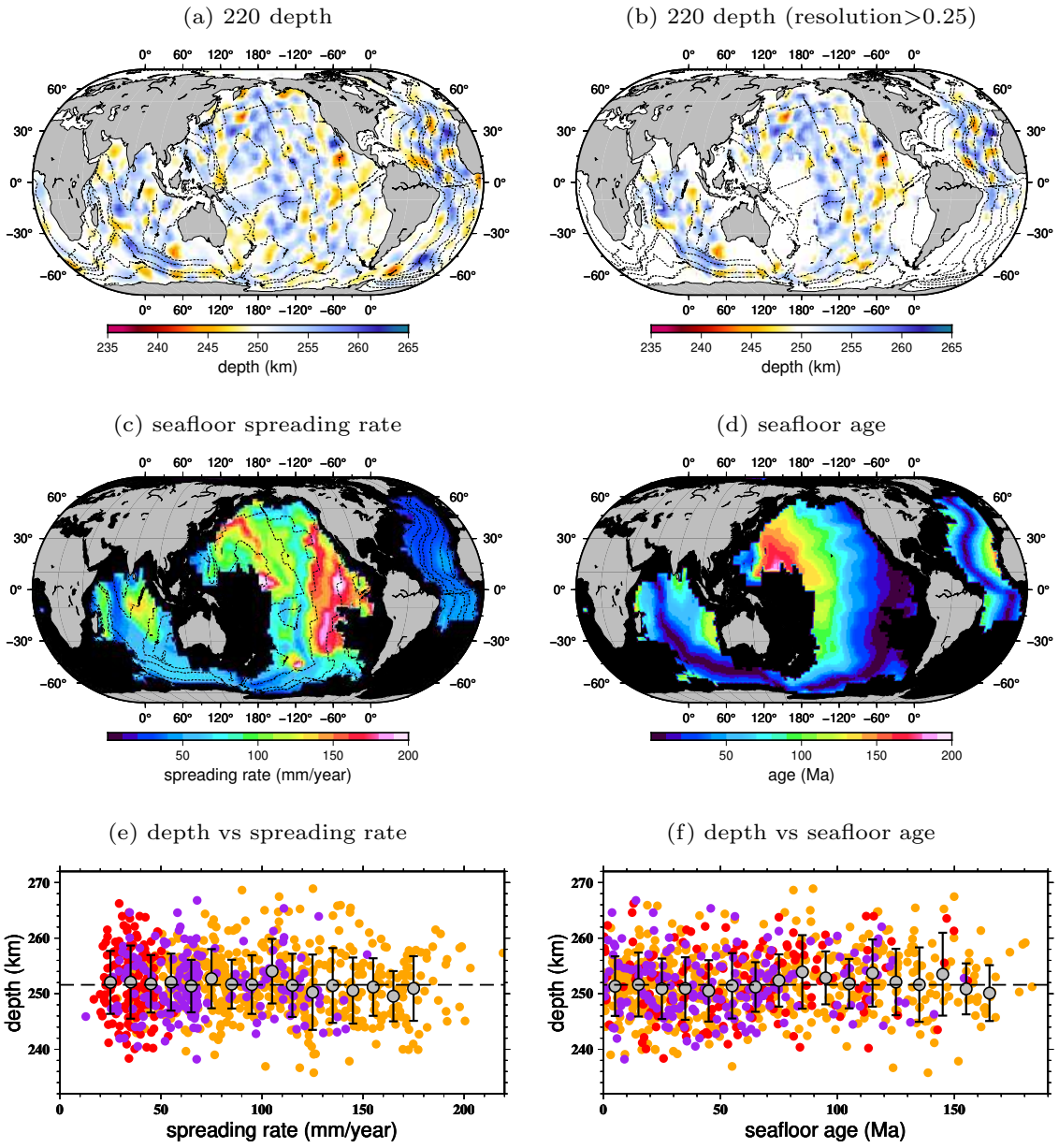

Figure 3.4: **(No) correlation between the 220-km discontinuity depth and seafloor spreading rate or seafloor age.** **(a)**, depth of the 220-km discontinuity in oceanic regions **(b)**, depth of the 220-km discontinuity in oceanic regions with large resolution (> 0.25). **(c)** and **(d)**, seafloor spreading rate and seafloor age, respectively, in oceanic regions with large resolution (> 0.25). **(e)**, scatter plot of maximum depth of the 220-km discontinuity with respect to the seafloor spreading rate in $5^\circ \times 5^\circ$ degree cells in global oceans (Pacific Ocean in orange, Atlantic Ocean in red and Indian Ocean in purple). The earth surface is divided into certain 5° (longitude) $\times$ 5° (latitude) areas in **(b)** and then the maximum 220-km depth in each area are extracted, which are then plotted against the spreading rate at the center of the $5^\circ \times 5^\circ$ areas. Mean (maximum) depth of the 220-km discontinuity is plotted on the top in gray dots with one standard deviation. The mean (maximum) depth is obtained by averaging the maximum depth at seafloor spreading rate ranges of every 10 $mm/year$. The 220-km depth remains roughly constant at different seafloor spreading rates. **(f)**, same with **(e)** but for the scatterplots of the depth of the 220-km discontinuity against seafloor age. The 220-km depth remains roughly constant at different seafloor ages.

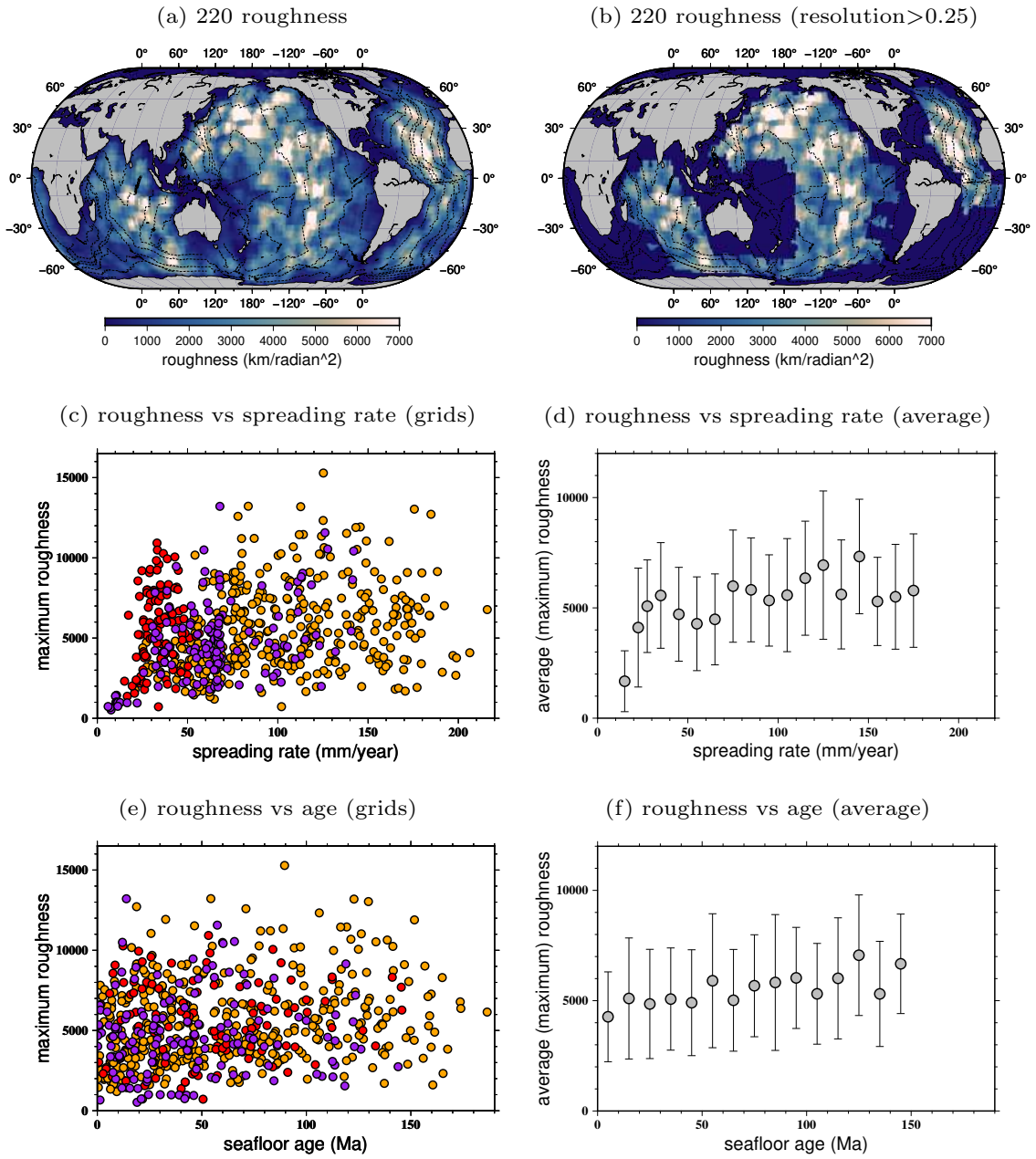

Figure 3.5: **Correlation between the 220-km discontinuity roughness and seafloor spreading rate. (a)**, roughness of the 220-km discontinuity in oceanic regions **(b)**, roughness of the 220-km discontinuity in oceanic regions with large resolution (> 0.25). **(c)**, scatter plot of maximum roughness of the 220-km discontinuity with respect to the seafloor spreading rate in $5^\circ \times 5^\circ$ degree cells in global oceans (Pacific Ocean in orange, Atlantic Ocean in red and Indian Ocean in purple). **(d)**, scatter plot of mean (maximum) roughness of the 220-km discontinuity against the seafloor spreading rate. The 220-km roughness generally increases with seafloor spreading rate in the global oceans. In addition, the roughness increases rapidly with spreading rate at slow-spreading seafloors while it increases slowly with spreading rate at fast-spreading seafloors. **(e)** and **(f)**, same with **(c)** and **(d)**, respectively, but for the scatterplots of the roughness of the 220-km discontinuity against seafloor age. There exists a weak positive correlation between the 220 roughness and seafloor age in global oceans.

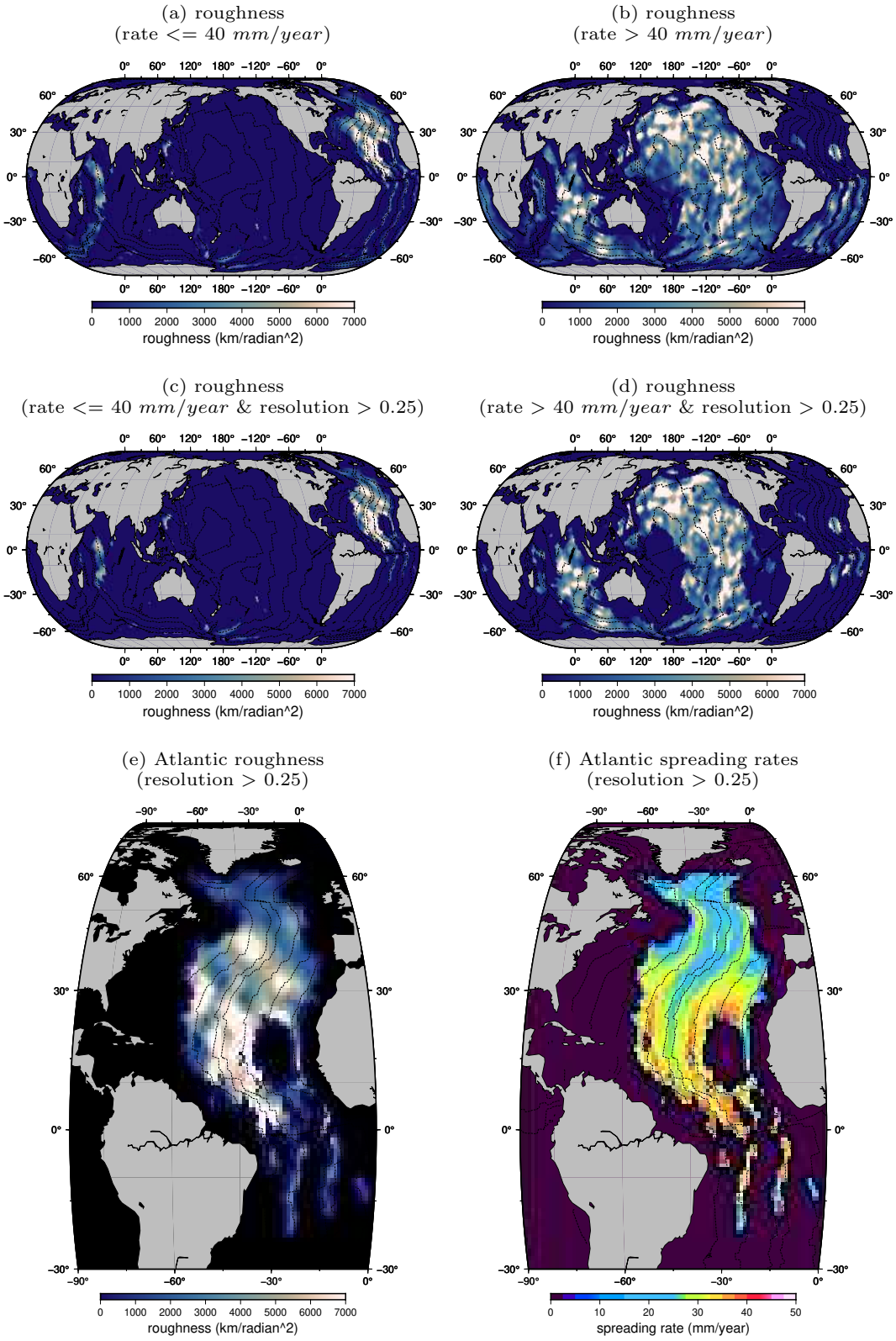

Figure 3.6: **(a)** and **(b)**, roughness of the 220-km discontinuity in oceanic regions with spreading rate <= 40 $mm/year$ and spreading rate > 40 $mm/year$, respectively. **(c)** and **(d)** are same with **(a)** and **(b)**, respectively, but only for oceanic regions with large resolution (> 0.25). **(e)**, roughness of the 220-km discontinuity in Atlantic Ocean with spreading rate <= 40 $mm/year$ and large resolution (> 0.25). **(f)**, spreading rate (<= 40 $mm/year$) in the Atlantic Ocean with large resolution (> 0.25).

Bibliography

[1] Gaherty, J. B. & Jordan, T. H. Lehmann discontinuity as the base of an anisotropic layer beneath continents. *Science* **268**, 1468–1471 (1995).

[2] Goncz, J. H. & Cleary, J. R. Variations in the structure of the upper mantle beneath australia, from rayleigh wave observations. *Geophysical Journal International* **44**, 507–516 (1976).

[3] Hales, A., Muirhead, K. & Rynn, J. A compressional velocity distribution for the upper mantle. *Tectonophysics* **63**, 309–348 (1980).

[4] Lehmann, I. Velocities of longitudinal waves in the upper part of the earth's mantle. In *Annales de géophysique*, vol. 15, 93 (1959).

[5] Lehmann, I. S and the structure of the upper mantle. *Geophysical Journal International* **4**, 124–138 (1961).

[6] Revenaugh, J. & Jordan, T. H. Mantle layering from scs reverberations: 3. the upper mantle. *Journal of Geophysical Research: Solid Earth* **96**, 19781–19810 (1991).

[7] Deuss, A. & Woodhouse, J. H. A systematic search for mantle discontinuities using ss-precursors. *Geophysical Research Letters* **29**, 90–1 (2002).

[8] Deuss, A. & Woodhouse, J. H. The nature of the lehmann discontinuity from its seismological clapeyron slopes. *Earth and Planetary Science Letters* **225**, 295–304 (2004).

[9] Gu, Y. J., Dziewonski, A. M. & Ekström, G. Preferential detection of the lehmann discontinuity beneath continents. *Geophysical Research Letters* **28**, 4655–4658 (2001).

[10] Schmerr, N. & Garnero, E. Investigation of upper mantle discontinuity structure beneath the central pacific using ss precursors. *Journal of Geophysical Research: Solid Earth* **111** (2006).

[11] Shearer, P. M. Constraints on upper mantle discontinuities from observations of long-period reflected and converted phases. *Journal of Geophysical Research: Solid Earth* **96**, 18147–18182 (1991).

[12] Cara, M. Lateral variations of s velocity in the upper mantle from higher rayleigh modes. *Geophysical Journal International* **57**, 649–670 (1979).

[13] Rost, S. & Weber, M. A reflector at 200 km depth beneath the northwest pacific. *Geophysical Journal International* **147**, 12–28 (2001).

[14] Shen, Y., Sheehan, A. F., Dueker, K. G., de Groot-Hedlin, C. & Gilbert, H. Mantle discontinuity structure beneath the southern east pacific rise from p-to-s converted phases. *Science* **280**, 1232–1235 (1998).

[15] Tkalčić, H., Flanagan, M. P. & Cormier, V. F. Observation of near-podal P'P' precursors: Evidence for back scattering from the 150–220 km zone in the earth's upper mantle. *Geophysical research letters* **33** (2006).

[16] Vidale, J. E. & Benz, H. M. Upper-mantle seismic discontinuities and the thermal structure of subduction zones. *Nature* **356**, 678–683 (1992).

[17] Laske, G., Masters, G., Ma, Z. & Pasyanos, M. Update on crust1. 0—a 1-degree global model of earth's crust. In *Geophys. Res. Abstr*, vol. 15, 2658 (2013).

[18] Ritsema, J., Deuss, a. A., Van Heijst, H. & Woodhouse, J. S40rts: a degree-40 shear-velocity model for the mantle from new rayleigh wave dispersion, teleseismic traveltime

and normal-mode splitting function measurements. *Geophysical Journal International* **184**, 1223–1236 (2011).

[19] Bach, W. & Früh-Green, G. L. Alteration of the oceanic lithosphere and implications for seafloor processes. *Elements* **6**, 173–178 (2010).

[20] Cannat, M. Emplacement of mantle rocks in the seafloor at mid-ocean ridges. *Journal of Geophysical Research: Solid Earth* **98**, 4163–4172 (1993).

[21] Horen, H., Zamora, M. & Dubuisson, G. Seismic waves velocities and anisotropy in serpentinized peridotites from xigaze ophiolite: Abundance of serpentine in slow spreading ridge. *Geophysical Research Letters* **23**, 9–12 (1996).

[22] Carbotte, S. M. & Macdonald, K. C. Comparison of seafloor tectonic fabric at intermediate, fast, and super fast spreading ridges: Influence of spreading rate, plate motions, and ridge segmentation on fault patterns. *Journal of Geophysical Research: Solid Earth* **99**, 13609–13631 (1994).

[23] Niu, Y. & Hekinian, R. Spreading-rate dependence of the extent of mantle melting beneath ocean ridges. *Nature* **385**, 326–329 (1997).

[24] Rubin, K. H. & Sinton, J. M. Inferences on mid-ocean ridge thermal and magmatic structure from morb compositions. *Earth and Planetary Science Letters* **260**, 257–276 (2007).

[25] Mutter, J. C. & Karson, J. A. Structural processes at slow-spreading ridges. *Science* **257**, 627–634 (1992).

[26] Bull, J. M. & Scrutton, R. A. Fault reactivation in the central indian ocean and the rheology of oceanic lithosphere. *Nature* **344**, 855–858 (1990).

[27] Phipps Morgan, J., Parmentier, E. & Lin, J. Mechanisms for the origin of mid-ocean ridge axial topography: Implications for the thermal and mechanical structure of accreting plate boundaries. *Journal of Geophysical Research: Solid Earth* **92**, 12823–12836 (1987).

[28] Purdy, G., Kong, L., Christeson, G. & Solomon, S. Relationship between spreading rate and the seismic structure of mid-ocean ridges. *Nature* **355**, 815–817 (1992).

[29] Thatcher, W. & Hill, D. P. A simple model for the fault-generated morphology of slow-spreading mid-oceanic ridges. *Journal of Geophysical Research: Solid Earth* **100**, 561–570 (1995).

[30] Toomey, D. R., Solomon, S. C., Purdy, G. & Murray, M. H. Microearthquakes beneath the median valley of the mid-atlantic ridge near 23° n: Hypocenters and focal mechanisms. *Journal of Geophysical Research: Solid Earth* **90**, 5443–5458 (1985).

[31] Toomey, D. R., Solomon, S. C. & Purdy, G. Microearthquakes beneath median valley of mid-atlantic ridge near 23° n: Tomography and tectonics. *Journal of Geophysical Research: Solid Earth* **93**, 9093–9112 (1988).

[32] Hammond, W. C. & Humphreys, E. D. Upper mantle seismic wave velocity: Effects of realistic partial melt geometries. *Journal of Geophysical Research: Solid Earth* **105**, 10975–10986 (2000).

[33] Chantel, J. *et al.* Experimental evidence supports mantle partial melting in the asthenosphere. *Science advances* **2**, e1600246 (2016).

[34] Escartin, J. *et al.* Central role of detachment faults in accretion of slow-spreading oceanic lithosphere. *Nature* **455**, 790–794 (2008).

[35] Deng, K. & Zhou, Y. Wave diffraction and resolution of mantle transition zone discontinuities in receiver function imaging. *Geophysical Journal International* **201**, 2008–2025 (2015).

[36] Zhou, Y. Multimode surface wave sensitivity kernels in radially anisotropic earth media. *Geophysical Journal International* **176**, 865–888 (2009).

[37] Guo, Z. & Zhou, Y. Stagnant slabs and their return flows from finite-frequency tomography of the 410-km and 660-km discontinuities. *Journal of Geophysical Research: Solid Earth* **126**, e2020JB021099 (2021).

[38] Zhou, Y. Anomalous mantle transition zone beneath the yellowstone hotspot track. *Nature Geoscience* **11**, 449–453 (2018).

Chapter 4

Finite-Frequency Imaging of the 220-km Discontinuity beneath the Global Continents

4.1 Introduction

A global low-velocity zone in the upper mantle was first proposed by Gutenberg based on an exponentially decrease in P wave amplitudes observed at a certain epicentral distance range also called shadow zone [1]. The existence of such a low-velocity layer at depths between 100 and 250 km was later confirmed by global surface wave studies. Seismic velocity decrease of $\sim$ 2%-10% in this layer has been reported in global oceans and continents including cratons and tectonically active regions [2, 3]. This low-velocity zone is also characterized by high electrical conductivities and strong attenuation. It is generally understood that this weak layer plays a key role in decoupling tectonic plates from the convecting mantle [1, 4, 5, 6, 7, 8]. The base of the weak layer (asthenosphere) was first observed in Europe and North America, with a sudden velocity increase at a depth of about 220 km [9, 10]. This discontinuity is often referred as the Lehmann discontinuity. A discontinuity at this depth with 5% of velocity increase was incorporated in the spherically averaged Preliminary Reference Earth Model (PREM) [11].

The 220-km discontinuity has been observed in continental regions in seismic studies using nuclear explosion data [12], refraction [13, 14, 15], underside reflections of depth phases [16], surface waves [17, 18], receiver functions [19, 20, 21], joint inversion of surface waves, body waves and ScS reverberation [22, 23, 24, 25]. The oceanic observations are generally more difficult to make because of limited deployment of seismic stations in the global oceans and this discontinuity has only been detected sporadically in different local oceanic areas using surface waves [26], receiver functions [27], PP and P'P' precursors [28, 29].

SS precursors are shear waves reflected off an internal discontinuity about half way between the source and receiver. They arrive at the receivers tens to hundreds of seconds prior to the main SS waves. SS precursors have become a popular seismic phase in imaging internal mantle discontinuities because they are sensitive to the structure in the vicinity of the SS bounce points and therefore they provide excellent global data coverage. SS precursors are secondary waves with small amplitudes and they are easily subjected to noise contamination. SS precursor stacking, which stacks a large amount of seismograms, has been used to enhance the signal levels of the data. In PREM, the magnitude of the velocity change across the 220-km discontinuity is comparable to that across the 410-km and 660-km discontinuities. Given that reflections from the 410-km and 660-km discontinuities are visible in global stacks, signals from 220-km discontinuity are also expected. However, reflections from this discontinuity have been missing or weak on global stacks of long-period seismograms [30, 31]. Geographic stacking is an approach by which seismic records in geographic caps within a certain radius (e.g., 10°) are stacked. Based on geographic stacking, Gu et al. (2001) suggested that $S_{220}S$ waves are observed mostly in the continental areas [32] while other studies reported observations in both continental and oceanic regions [31, 33]. A recent study by Sun and Zhou (2023) [8] observed the 220-km discontinuity across the global oceanic regions and proposed that the absence of the $S_{220}S$ wave on many global stacks may

be caused by large depth perturbations of this discontinuity. The absence of the $S_{220}S$ wave on global stacks and its presence on some geographic stacks indicate stacking result may depend on variations of the $S_{220}S$ arrivals across seismograms.

This paper represents a follow-up study of Sun and Zhou (2023) [8, 34] with a focus on the 220-km discontinuity beneath the continental regions. The observations of the 220-km discontinuity in the global oceans has been documented in Sun and Zhou (2023) [34]. In this paper, we will focus on the dataset of the $S_{220}S$ waves with reflection points in continental regions and we will discuss the structure of the 220-km discontinuity at a global scale. Lateral depth perturbations of the discontinuity will be obtained using finite-frequency tomography, and we will discuss the absence of the $S_{220}S$ wave in global stacks based on analysis of discontinuity topography.

4.2 Data and Methods

We download a total of 54,675 seismograms from the Data Management Center at the Incorporated Research Institutions for Seismology (IRIS) for earthquakes with magnitudes between 6.0 and 8.0 that occurred between 2009 and 2020. In this dataset, 32,369 seismograms (59.2%) have SS wave bounce points in oceanic regions (hereinafter referred as oceanic data) and 22,306 seismograms (40.8%) have SS reflection points in continental regions (hereinafter referred as continental data). We deconvolve the instrument response from each seismogram and then rotate the horizontal component seismograms to obtain the radial and transverse components. The seismograms are bandpass filtered between 10 and 80 mHz. We only analyze transverse (SH) component displacement seismograms in this study to avoid the contamination of P and SV waves. We first examine the dataset and keep only seismograms with simple SS waves while excluding those with complicated source time

functions. SS waves that are significantly different (e.g., in polarity) from the synthetic SS waves are discarded. We also exclude seismograms with epicentral distances smaller than 80 degrees because SS precursors from different mantle discontinuities are not well separated. These selection criteria leaves 14,592 out of 54,675 seismograms ($\sim$ 26.7%) including 6,506 oceanic data and 8,086 continental data, respectively.

The SS waves with bouncepoints in oceanic regions has been discussed in Sun and Zhou (2023) [8, 34]. In this followup study, we include data with bouncepoints in the continental regions and will focus on observations of the 220-km discontinuity at a global scale. A total of 8,086 high-quality SS waves from 524 earthquake events are recorded on 145 Global Seismographic Network (GSN) stations (Figure 4.1). The majority of the earthquake events (396 out of the 524) have focal depths shallower than 75 km. This limits the interference between sSS waves and SS precursors. The $S_{220}S$ waves are the first precursors following the $S_{410}S$ waves. We inspect the SS precursors visually and identify 3,669 clear $S_{220}S$ on the 8,086 seismograms ($\sim$ 45.3%). $S_{220}S$ waves are not observed on many seismograms due to weak source radiation and those heavily contaminated by other seismic phases are also not used in this study. The dataset shows a fairly uniform distribution of epicentral distances ranging from 80 to 178 degrees (Figure 4.1).

4.2.1 Identification of Phase Interference Using Finite-Frequency Sensitivities

$S_{220}S$ precursors are characterized by small amplitudes and may not be the dominant phase in a measurement window. For shallow earthquakes, the possible interfering phases include topside reflections (e.g., $S_{660}sS$ and $S_{660}sS_{diff}$) at epicentral distance range $\sim$ 80° - $\sim$ 95°, $S_{670}ScS_{670}S$ at $\sim$ 120° - $\sim$ 130° and $S_{410}ScS_{410}S$ at $\sim$ 140° - $\sim$ 160°. At distances greater than

$\sim 160°$, $S_{220}S$ waves interfere with ScS reverberations reflected at the 220-km discontinuity. At distance between 95° and 120° as well as 130° and 140°, $S_{220}S$ waves are separated well with the above interferences. Depth phases (e.g., $sS_{660}S$ and $sS_{410}S$) may interfere with $S_{220}S$ for earthquakes with deep focal depths. To better isolate $S_{220}S$ waves from interference phases, we examine the moveout of each by inspecting both the synthetic and observed seismograms across a wide epicentral distance range.

The classic stacking approach used in SS precursor studies works well when observations are made in a narrower epicentral distance range and earthquakes are shallow such that the SS precursors are well separated from interfering phases, which would exclude a large amount of data. In this study, we calculate the finite-frequency traveltime sensitivities to boundary depth perturbations, which take into account complete phase interactions regardless of earthquake depth and station distance. We examine the finite-frequency sensitivities of $S_{220}S$ waves to identify phase interference and measurements associated with abnormal sensitivities are excluded. Due to phase interactions, the abnormal kernels are often extremely small or large in amplitudes with structures different from what is expected for reflected waves [8]. To reduce the uncertainty of the model, measurements outside two standard deviations are not used in tomographic inversion. Synthetic seismograms are calculated for 1-D reference models MREF and PREM based on traveling-wave mode summation [35]. The reference model MREF is modified from PREM and it includes a sharp discontinuity at 250 km depth with a 7% velocity increase to represent the base of the asthenosphere.

4.2.2 Finite Frequency Tomography

We measure differential traveltimes between $S_{220}S$ waves and SS waves $\delta t|_{S_{220}S} - \delta t|_{SS}$. The application of differential traveltime minimizes the uncertainties associated with source

origin times and 3-D mantle structure. The traveltime measurements are made for observed seismograms with respect to the synthetic seismograms calculated in the frequency domain at 25-second period. The length of the measurement windows for SS and $S_{220}S$ waves ranges from 39 to 128 seconds and from 38 to 90 seconds, respectively. The measurements $\delta t|_{S_{220}S} - \delta t|_{SS}$ can be expressed as a two-dimensional integration over the entire global surface of the 220-km discontinuity, Σ

$$\delta t|_{S_{220}S}(\omega) - \delta t|_{SS}(\omega) = \iint_{\Sigma} \left[K_{\Sigma}^{S_{220}S}(\mathbf{x}, \omega) - K_{\Sigma}^{SS}(\mathbf{x}, \omega) \right] \, \delta d(\mathbf{x}) \, d\Sigma, \tag{4.1}$$

where ω is the angular frequency and $\mathbf{x}$ is the position vector. $K_{\Sigma}^{S_{220}S}(\mathbf{x}, \omega)$ and $K_{\Sigma}^{SS}(\mathbf{x}, \omega)$ are the finite-frequency sensitivities of the $S_{220}S$ and the SS waves to the depth perturbations $\delta d(\mathbf{x})$ of the discontinuity. We parameterize the surface of the discontinuity using a set of spherical triangular gridpoints. The spherical triangles are 16-fold, with 2562 vertexes and an average lateral spacing of about 4.3°. The discontinuity depth perturbations within any spherical triangle can be approximated by linear spatial interpolations through the depth perturbations at the three vertexes [36].

This discrete inverse problem can be written as

$$\boldsymbol{G}\boldsymbol{m} = \boldsymbol{d} \tag{4.2}$$

where $\boldsymbol{m}$ is the vector of the unknown depth perturbations of the discontinuity. $\boldsymbol{d}$ is the data vector of differential traveltime delay $\delta t|_{S_{220}S} - \delta t|_{SS}$. $\boldsymbol{G}$ is the finite-frequency sensitivity matrix.

This inverse problem is ill-posed because of the insufficient data coverage as well as noise in the data [37, 38]. We seek an optimal solution that minimizes data misfit:

$$\|\boldsymbol{Gm} - \boldsymbol{d}\|^2 = minimum \tag{4.3}$$

The minimization problem leads to:

$$\boldsymbol{G}^T\boldsymbol{Gm} - \boldsymbol{G}^T\boldsymbol{d} = 0 \tag{4.4}$$

The above inverse problem is solved based on the singular value decomposition of the matrix $\boldsymbol{G}^T\boldsymbol{G}$

$$\boldsymbol{G}^T\boldsymbol{G} = \boldsymbol{U}\boldsymbol{\Sigma}\boldsymbol{V}^T \tag{4.5}$$

where, $\boldsymbol{U}$ and $\boldsymbol{V}$ contain data and model singular vectors $\boldsymbol{u}_i$ and $\boldsymbol{v}_i$, respectively. $\boldsymbol{\Sigma}$ is a rectangular diagonal matrix with an upper 2562×2562 diagonal matrix ($\sigma_1 >= \sigma_2 >= \sigma_3$ ... $>= \sigma_{2562}$) and a lower zero matrix [39, 40]. Truncated singular value decomposition (TSVD) is applied to regularize the ill-posed linear least squares problem. In the case of TSVD, we approximate the matrix with a lower rank matrix $\boldsymbol{G}_k^T\boldsymbol{G}_k$, and the solution could be rewritten as,

$$\boldsymbol{m} = \sum_i^k \frac{{\boldsymbol{u}_i}^T\boldsymbol{G}^T\boldsymbol{d}}{\sigma_i}\boldsymbol{v}_i \tag{4.6}$$

The TSVD solution is not sensitive to the noise in $\boldsymbol{d}$ when the number k is chosen properly [41]. The truncation parameter k is determined by studying the trade-offs between the model norm and data misfit (Figure C.1). The corresponding resolution matrix of the model is:

$$\boldsymbol{R} = \boldsymbol{V}_k\boldsymbol{V}_k^T \tag{4.7}$$

4.3 Results

Strong $S_{220}S$ waves are observed on 3,422 individual transverse-component (SH) seismograms across the global continental regions, including cratons and tectonically active regions (Figure 4.2). At epicentral distance range between 96° and 119°, $S_{220}S$ waves are separated well from topside reflections or ScS reverberations. Example traces with clear $S_{220}S$ waves with SS bounce points in different tectonic settings are plotted in Figure 4.2. The focal depths of these example data are all less than 35 km so $S_{220}S$ waves are also not interfered by depth phases.

4.3.1 Finite-frequency Tomography of the Continental 220

SS precursors with bounce points in continental regions are used in finite-frequency tomography to map depth perturbations of the 220-km discontinuity. We measure traveltime delays of the SS waves and SS precursors with respect to synthetic seismograms computed for model MREF. The differential traveltimes $\delta t|_{S_{220}S} - \delta t|_{SS}$ are plotted in Figure 4.3. We apply crustal and mantle corrections to the measurements using global wavespeed models S40RTS [42] and CRUST 1.0 [43]. The mean travel time measurement after corrections is $\sim$ -5.2 seconds, close to the value $\sim$ -5.1 seconds without corrections (Figure 4.3). Negative mean traveltime delays indicate that the observed $S_{220}S$ waves arrive earlier than the synthetic $S_{220}S$ waves when SS waves are aligned.

The optimal model for the depth perturbations of the 220-km discontinuity is plotted in Figure 4.4a and Figure 4.5a, which is determined based on trade-off between model norm and data misfit (Figure C.1). The resolution of the model is plotted in Figure 4.4b and Figure 4.5c. Large lateral depth perturbations of the 220-km discontinuity can be observed over the global continents. The average 220-km depth is at $\sim$ 251.7 km while it varies from $\sim$ 235

km to $\sim$ 267 km (Figure 4.6a). A linear anomaly with shallower 220-km discontinuity can be found in the interior of the Eurasian plate, roughly in directions following the foothills of high topography. At the southern border of Eurasian plate where it collides with the Nubian, Arabian and Indian plates, a shallower 220-km discontinuity is observed stretching from the Mediterranean regions to southeastern Asia. The discontinuity is shallowest in the southern Mediterranean sea where subduction is complex. Shallower 220-km anomalies are also observed along the pacific subduction zones including the Cascadia Subduction Zone, Peru-Chile Trench and Japan-Kuril Kamchatka Trench. Discontinuity structures in high-latitude continental areas are best resolved, for example, in eastern Asia and northwest North America (Figure 4.4b and Figure 4.5c). Structures in Africa, Australia and South America are less well resolved because of uneven distribution of seismic events and stations. Regions close to the south pole in the Antarctic present minimal model resolution due to limited data coverage.

4.3.2 Global Tomography (Oceans and Continents)

In this section, we present depth perturbations of the 220-km discontinuity from joint inversion of both the continental and oceanic $\delta t|_{S_{220}S} - \delta t|_{SS}$ measurements. The global dataset comprises 6,176 measurements, with 3,422 measurements from continental regions and 2,754 measurements from oceanic areas (Figure 4.3). Crustal and mantle corrections have been applied to both dataset. Trade-off curves (Figure C.1) are used to determine the optimal model (Figure 4.5b). The resolution of the global inversion is plotted in Figure 4.5d, which is overall similar to model resolution from the independent inversion (Figures 4.4b and 4.5c). The optimal model from joint inversion using global measurements is also similar to the model obtained from independent inversion of only using the continental measurements (Figures 4.4a and 4.5a). The structures in independent inversion are overall stronger because more

"damping" is required to regularize the inversion of the global dataset. The depth of the 220-km discontinuity beneath continental regions ranges from $\sim$ 237 km to $\sim$ 265 km with average at $\sim$ 251.6 km (Figure 4.6b), similar to the model from independent inversion. Figure 4.7 shows the depth perturbations of the 220-km discontinuity in both oceanic and continental regions obtained by joint inversion using global $S_{220}S$ traveltime delays. The depth of the 220-km discontinuity beneath global oceans varies between $\sim$ 236 km and $\sim$ 266 km, with an average depth of 251.0 km, which is about the same as the average depth of continental 220-km discontinuity (251.6 km). The depth models obtained using data without crustal and mantle corrections shows similar depth structure (Figure 4.8). We calculate depth-averaged shear wavespeed perturbations in upper mantle using model S40RTS and find there is no clear correlation between wavespeed anomalies and the 220-km depth perturbations (Figure 4.9).

4.3.3 $S_{220}S$ Amplitude Measurements

To constrain the velocity contrast across the discontinuity, we measure the amplitudes of the $S_{220}S$ waves following the same measurement approach as in by Sun and Zhou (2023) [8]. The amplitudes of SS precursors, including $S_{220}S$, $S_{410}S$ and $S_{660}S$ are all measured in frequency domain. We calculate the minimum amplitude ratio γ = minimum[$\log(A_{S_{\mathrm{LAB}}S}/A_{S_{410}S})$, $\log(A_{S_{\mathrm{LAB}}S}/A_{S_{660}S})$] to model the velocity contrast across the 220. There is no obvious difference between the amplitudes of $S_{220}S$ waves beneath the continental and oceanic regions, which both show average values close to 0 (Figure 4.10a), indicating that the amplitude of the $S_{220}S$ is about the same as the amplitude of the $S_{410}S$ and $S_{660}S$. The mean amplitudes of the synthetic $S_{220}S$ waves calculated for model MREF are also close to 0 for both continental and oceanic data (Figure 4.10b), indicating the observed $S_{220}S$ waves could be explained by a $\sim$7% velocity increase in model MREF. PREM synthetics underestimates the velocity

increase across the 220-km discontinuity because the mean amplitudes of PREM synthetics in oceans and continents are both at $\sim$ -0.2 (Figure 4.10c).

4.4 Discussions

4.4.1 Global Presence of the 220-km Discontinuity

SS precursors from the 220-km discontinuity is observed across the globe in both continental and oceanic regions. This interface has a large lateral depth variations with a range from 235 km to 267 km. The average depth of the 220-km discontinuity is about 250 km beneath both continents and oceans. This is roughly consistent with a recent global receiver function study which proposed that a discontinuity with a positive velocity gradient exist in broad regions with a center depth of $\sim$ 260 km globally [44].

Large depth perturbations of the 220-km interface have been observed in many global and regional studies, including SS precursors studies in both continents and oceans [23, 28, 45]. Regional SS precursor stacks in eastern Asia reveal a 220-km interface at depths 250-260 km in eastern Asia [46]. Analysis of regional receiver functions have also suggested the presence of the 220-km boundary at a depth of 240 km in central Fennoscandia [19] and a depth range of 200 $\sim$ 300 km in Europe, North America and Australia [23, 47, 48, 49, 50].

Deeper reflectors at depth between 250 and 350 km are sometimes referred as the X discontinuity and they have been observed in different tectonic settings [23, 45, 51, 52, 53, 54, 55, 56], though we do not observe reflectors deeper than 270 km in this study. Seismic reflectors at this depth range are often associated with a wide range 2%-8% of velocity increase [33, 45, 53, 54, 55], and with a larger velocity change in continental regions than the oceanic regions [33, 45]. The large variations in velocity increase may reflect a strong topography of

this discontinuity, which reduces the amplitudes of the waves in stacking.

The 220-km discontinuity is shallower in the western US and becomes deeper in the central US. This is consistent with the study of Calò et al. (2016) [25] in which an increase in the 220-km depth was observed from the western side of the Rocky mountain towards the more stable cratons to the east [25]. The 220-km depth is proposed to reside deepest beneath the western Australian craton and turn shallower beneath Phanerozoic orogenic zones [23]. However, in Australia, the 220 is deeper in the eastern tectonically active regions in this study. There is no clear correlation between the average wavespeed in the mantle and the depth of the 220 (Figure 4.9). This observation indicates mantle temperature at the depth of 250 km is about the same regardless of tectonic settings and secular cooling has minimum impact on the base of the asthenosphere in continental regions.

4.4.2 Correlation between the 220-km Discontinuity and Surface Tectonics

The Pacific subduction zone and the southern boundary of the Eurasian plate present the most prominent structures of gravity, topography and wavespeed anomalies on the earth (Figure 4.4). Strong, continuous shallow 220-km discontinuity anomalies aligned approximately in a West-East direction are observed along the southern edge of the Eurasian plate, extending from the Mediterranean regions to southeastern Asia, indicating a connection between the asthenospheric dynamics and the collision of Nubian, Arabian and Indian plates to Eurasian plate. Linear structures of the 220-km depth perturbations roughly following the circum-Pacific subduction zone can also be observed in the western North America, South America. This observation indicates subduction at the convergent boundaries may have a major impact on the asthenospheric dynamics. Shallower 220-km discontinuity anomalies

are observed along the foothills of high topography and strong gravity anomalies in the interior of the Eurasian plate might result from the far-field effect of the continent-continent collision at the southern border of the Eurasian plate because the India-Asia collision has been suggested to deform the regions over large distances, from the Himalayan Orogen to Baikal rift zone in southeast Siberia [57, 58, 59, 60].

4.4.3 The Absence of $S_{220}S$ on Global Stacks

Many previous studies have reported that $S_{220}S$ waves are absent on global SS wave stacks (e.g., [30, 31]). To investigate limitations in stacking, we stack 6,176 seismograms in our global dataset in every 10° epicentral distance intervals. To reduce interference with depth phases, we restrict our dataset to shallow earthquake events with focal depths less than 75 km. The first step is to align the SS waves using a cross-correlation method for both observed and synthetic seismograms. The polarities are reversed whenever necessary. Seismograms with SS bounce points in oceanic and continental regions are stacked separately. The stacking result is plotted in Figure 4.11. Strong precursors $S_{660}S$, $S_{410}S$, $S_{220}S$ are observed on both the oceanic and continental stacks of synthetic seismograms. However, unlike the transition zone $S_{410}S$ and $S_{660}S$ phases, we do not observe strong $S_{220}S$ waves on most of the stacks of observed seismograms. This suggests that lateral depth variations of the 220-km discontinuity are much larger which leads to destructive interference of the $S_{220}S$ waves in stacking [8, 28, 32].

However, $S_{220}S$ waves have been reported on some geographic stacks in previous studies which are obtained by stacking seismograms with SS bounce points in small geographic regions (e.g., [33, 45]). If lateral depth variations of the 220-km discontinuity is small, it is possible to produce coherent $S_{220}S$ waves on the geographic stacks. We stack seismograms

in 10° radius in different geographic locations. The observed arrivals of $S_{220}S$, $S_{410}S$ and $S_{660}S$ are individually corrected to a reference epicentral distance of 120° using travel time tables calculated for model MREF. Seismograms with SS bounce points within a 10° circle distance around each of 2562 grid points are included to build the stacks. A minimum of 30 seismograms is required to build a stack at a particular grid point. Due to limited seismograms in this dataset, the geographic stacking does not have a good global coverage. Example stacking in Figures 4.12 and 4.13 show that $S_{220}S$ waves could be observed on stacks in regions where the standard deviations of the 220-km discontinuity depth are small (Figure 4.12). On the other hand, $S_{220}S$ waves are weak to absent on the stacks in regions in the northwestern Pacific where large 220-km depth variations are observed (Figure 4.13). We should point out that the correlation between the standard deviation of the 220-km depth perturbations and clear $S_{220}S$ waves on stacked seismograms is not expected to be perfect because we have limited resolution. In addition, factors other than depth perturbations, for example, data quality, number of data points, will also affect the $S_{220}S$ stacks. However, we observe a general correlation that can explain the absence of the $S_{220}S$ in some regions, for example, the Northwestern pacific.

4.5 Conclusions

In this study, we observe clear SS precursors reflected off the 220-km discontinuity across the continents around the globe, including tectonically active regions, stable cratons and subduction zones. Finite-frequency tomography of SS precursors shows that the 220-km discontinuity varies between 235 km and 267 km with an average depth of about 250 km. The amplitudes can be explained by a velocity increase of $\sim 7\%$ across the interface. The continental 220-km discontinuity is comparable to the oceanic 220-km discontinuity interface

in their average depth, lateral variation and velocity change across the boundary, and this observation indicates a common mechanism of asthenosphere beneath the continents and oceans. In continental regions, the 220-km depth anomalies are observed along convergent plate boundaries as well as within the plate interior. For instance, West-East striking 220-km depth anomalies are observed along the convergent plate boundaries between the Eurasian and Indian-Arabian-Nubian plates. Depth anomalies are also observed in the Western North America, Eastern Asia and South America, parallel to the Pacific subduction zone. The formation of these anomalies might be closely related to the mantle processes associated with the continent-continent collision and subduction. Depth anomalies are also observed in the interior of Eurasian plate, roughly following the foothills of high topography and strong gravity anomaly, which might be a result of far-field dynamics associated with continent-continent collision at the southern border of the Eurasian plate. We show that reflections from the 220-km discontinuity are absent on the global stacks, which can be explained by large variations of the 220-km discontinuity depth. For example, $S_{220}S$ waves are absent on geographical stacks in regions with large variations in discontinuity depth while they become clear signals on the stacks in areas with small lateral depth perturbations. There is no apparent connection between mantle wavespeed perturbations and the depth of the 220, indicating that secular cooling has a minimum impact on the base of the asthenosphere.

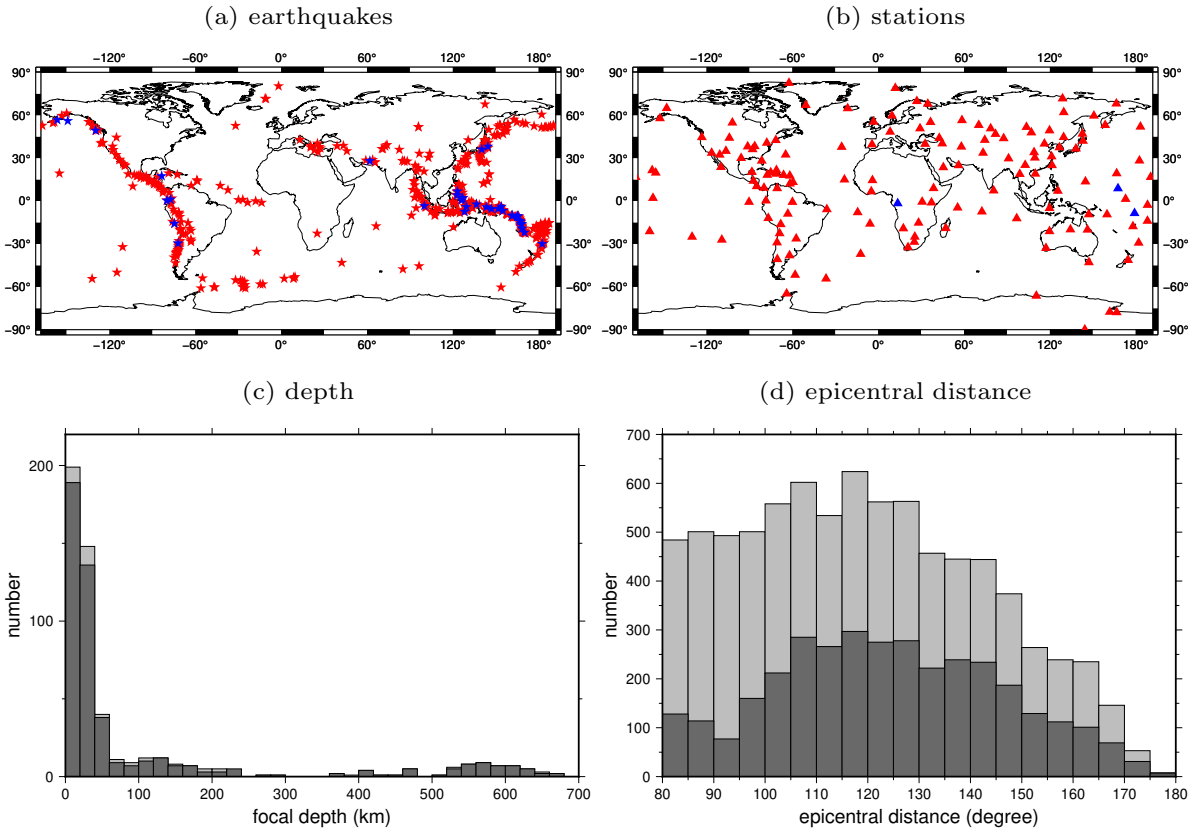

Figure 4.1: (a) distribution of 524 earthquakes used in the global dataset, with strong SS waves observed on 8,087 seismograms. The bouncepoints of the SS waves are all located in continental regions. The 487 red stars are events from which clear $S_{220}S$ waves are observed and the 37 blue stars are events from which no clear $S_{220}S$ waves are observed. (b) distribution of 145 GSN stations where clear SS waves are observed, with $S_{220}S$ waves also observed on 142 of the stations (red triangles). (c) gray histograms are the focal depths of all 524 earthquake events. Black histograms are focal depths of the 487 events with clear $S_{220}S$ waves. (d) epicentral distances of the corresponding earthquakes in (c).

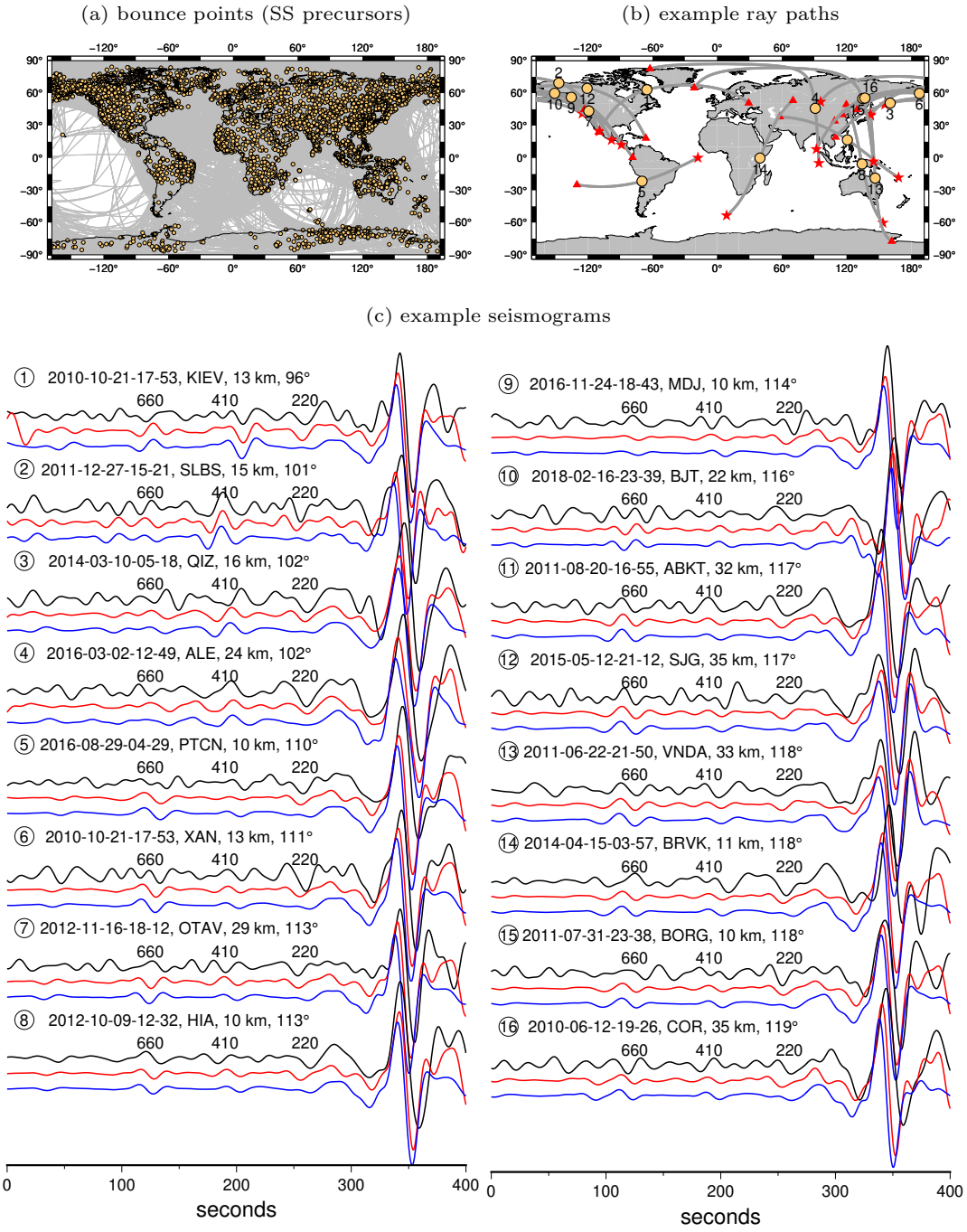

Figure 4.2: **(a)** bouncepoints of the $S_{220}S$ waves in the global continental dataset, plotted on top of their ray paths (grey lines). The dataset provides a good coverage across all continental regions. **(b)** bounce points and geographic ray paths of 16 example seismograms plotted in **(c)**. **(c)** example transverse-component seismograms with clear $S_{220}S$ phases including data (black) and synthetics calculated in reference 1-D models MREF (red) and PREM (blue). The velocity jumps across the 220-km discontinuity in MREF and PREM are 7% and 5%, respectively. SS waves have been aligned and some of the polarities are reversed for illustration only. The $S_{410}S$ and $S_{660}S$ waves arrivals are also labeled. The seismograms have been band-pass filtered between 10 and 80 mHz. The earthquake event date, station name, focal depth and epicentral distance are denoted on each set of seismograms. The epicentral distances of these example seismograms range between 96° and 119° and the focal depths are all shallower than 35 km. Theoretically, $S_{220}S$ waves are not interfered by other phases including topside reflections (e.g., $S_{660}sS$ and $S_{660}sS_{diff}$), ScS reverberations (e.g., $S_{670}ScS_{670}S$ and $S_{410}ScS_{410}S$) as well as depth phases (sSS waves).

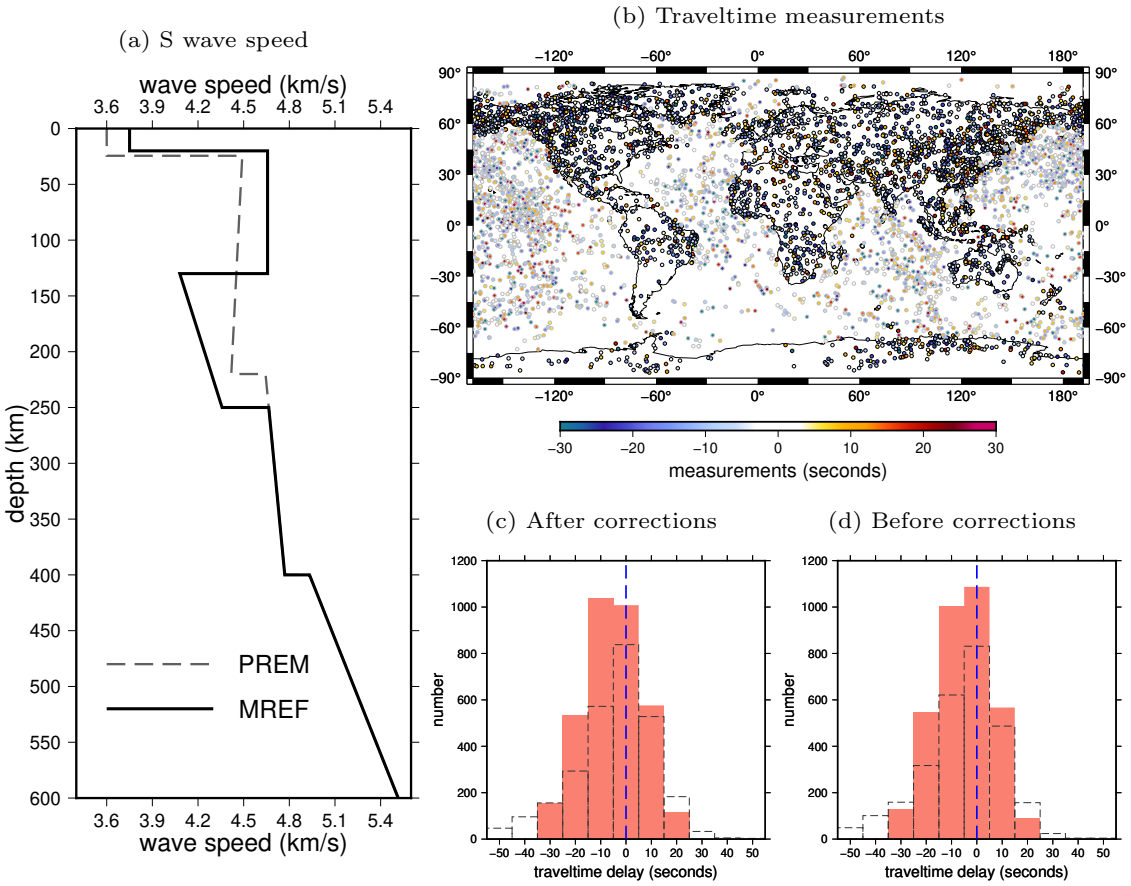

Figure 4.3: **(a)** S-wave speed in model MREF (solid black line) and model PREM (dashed black line). The velocity increase across the 220-km discontinuity in model PREM is 5%. Model MREF is revised from model PREM and it incorporates two discontinuities at 130 km and 250 km depths, to represent the lithosphere asthenosphere boundary (LAB) and the 220-km discontinuity, respectively, with the velocity contrasts of 12% and 7%. **(b)** $\delta t|_{S_{220}S} - \delta t|_{SS}$ traveltime measurements after crustal and mantle corrections. The global dataset includes 3,422 measurements with SS wave bouncepoints located in the global continental regions (black outlines) as well as 2,754 measurements with bouncepoints in the global oceanic regions from the study of Sun & Zhou (in submission). **(c)** histograms of traveltime measurements including the 3,422 continental measurements (red filling) and 2,754 oceanic data (black, dashed outlines). **(d)** same as **(c)** but for traveltimes without crustal and mantle corrections. The mean traveltime of the continental $\delta t|_{S_{220}S} - \delta t|_{SS}$ measurements after and before corrections are -5.2 seconds and -5.1 seconds, respectively. The mean oceanic measurements after and before corrections are -4.5 seconds and -5.3 seconds.

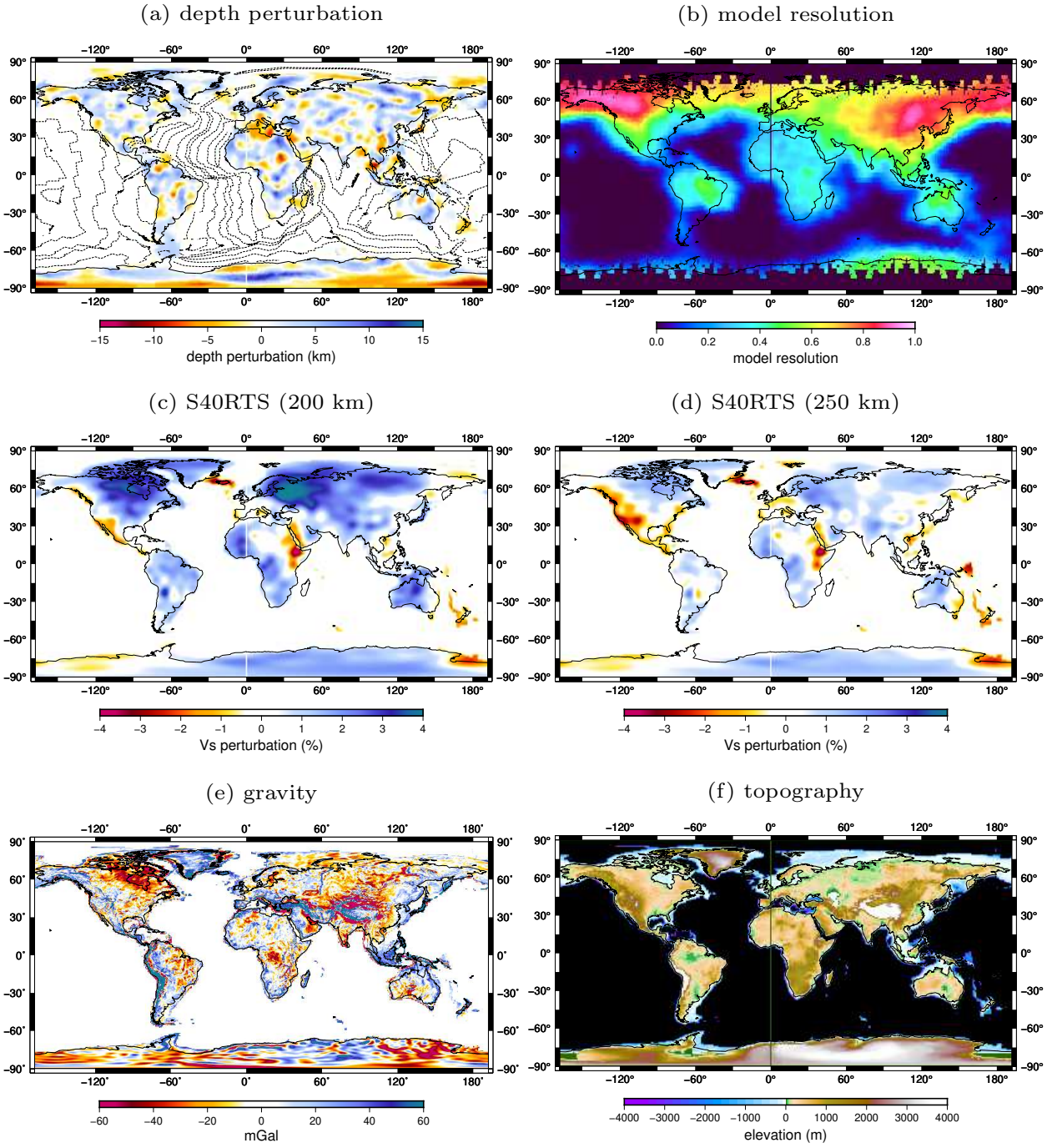

Figure 4.4: **(a)** depth perturbations of the 220-km discontinuity obtained from finite-frequency inversion of the continental data (Fig. 3). The resolution of the model is plotted in **(b)**. **(c)** and **(d)** are shear wavespeed perturbations from model S40RTS at 200 km and 250 km depths, respectively. **(e)** and **(f)** are gravity anomalies [61] and topography [62] in continental regions, respectively.

(a) depth perturbation (continental)

(b) depth perturbation (global)

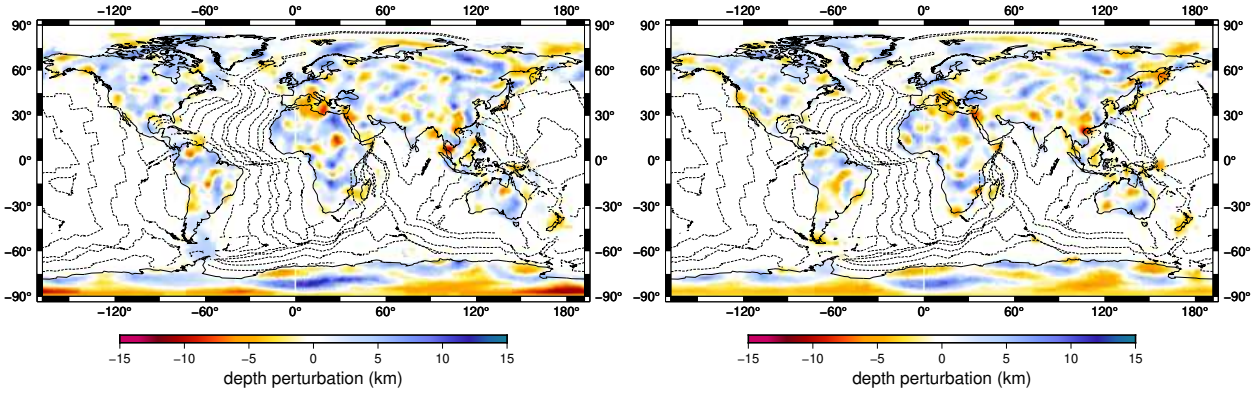

(c) resolution (continental)

(d) resolution (global)

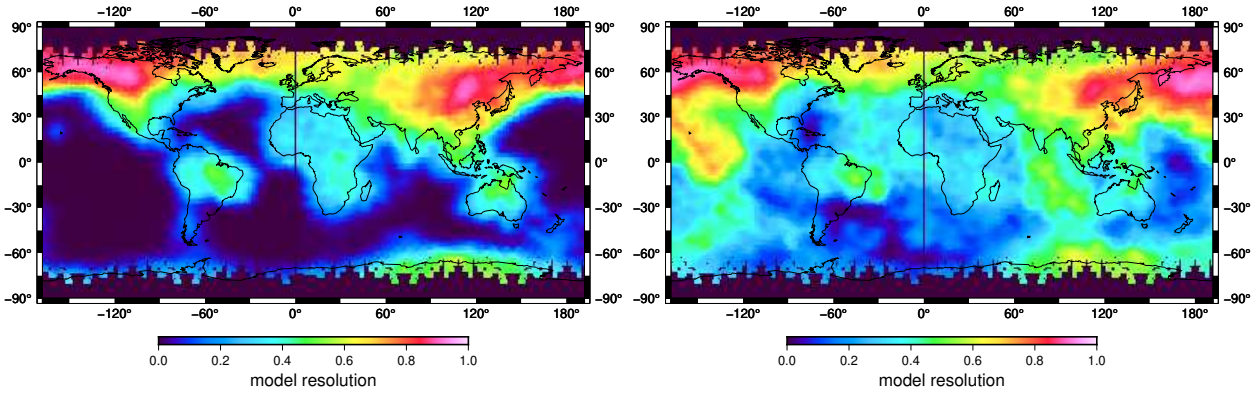

Figure 4.5: Depth perturbations of the 220-km discontinuity in continental regions obtained from finite-frequency inversion using only the continental data in **(a)** and joint inversion of both oceanic and continental data in **(b)**. Only structures in the continental regions are plotted for comparison. **(c)** and **(d)** are the model resolutions of **(a)** and **(b)**, respectively.

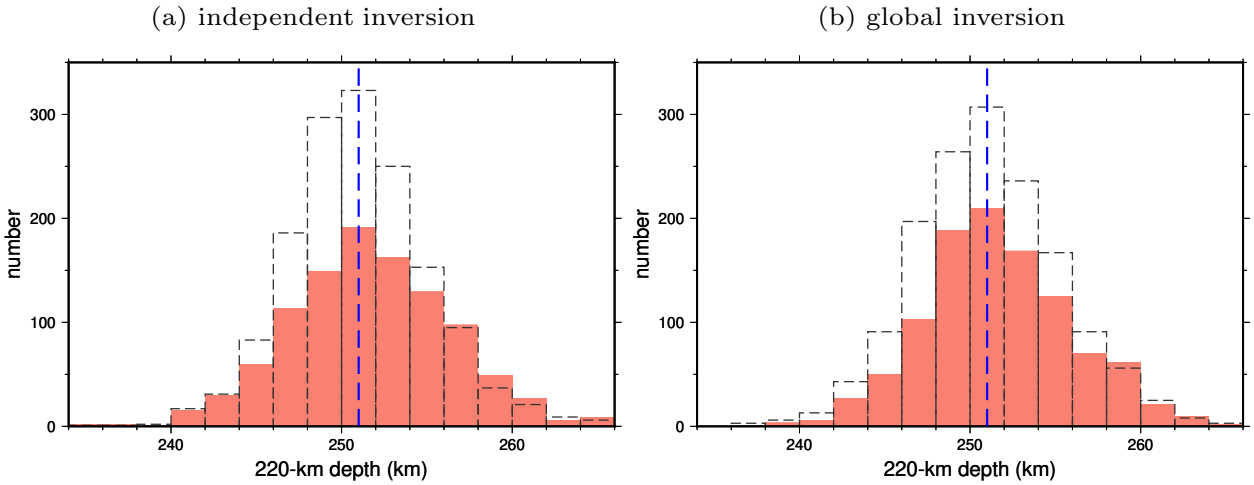

Figure 4.6: (a) histograms of the 220-km discontinuity depth in continental (red filling) and oceanic regions (dashed, black outlines). The 220-km discontinuity depth in continental and oceanic regions are inverted independently. (b) same as (a) but for depths from joint global inversion of both the oceanic and continental data. The average continental 220-km discontinuity depth is about 251 km, which is close to the average depth of the oceanic 220-km discontinuity in both independent and joint inversions.

(a) oceanic 220-km discontinuity

(b) continental 220-km discontinuity

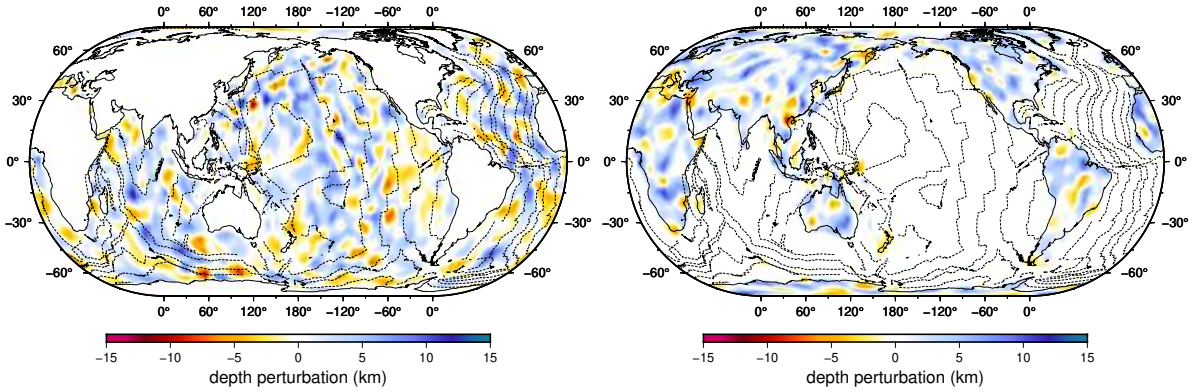

Figure 4.7: (a) and (b) are the 220-km discontinuity depth perturbations in oceanic and continental regions, respectively, obtained from joint inversion of both the continental and the oceanic data.

(a) Traveltime (no corrections)

(b) 220 perturbations (no corrections)

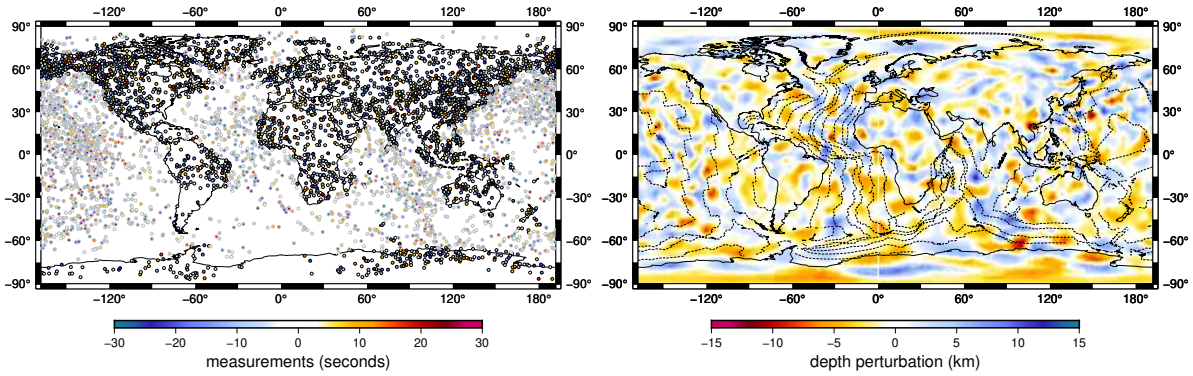

Figure 4.8: **(a)** is same as Fig. 3b but for $\delta t|_{S_{220}S} - \delta t|_{SS}$ traveltimes without crustal and mantle corrections. **(b)** same as Fig. 7, but for depth perturbation of the 220-km discontinuity without corrections.

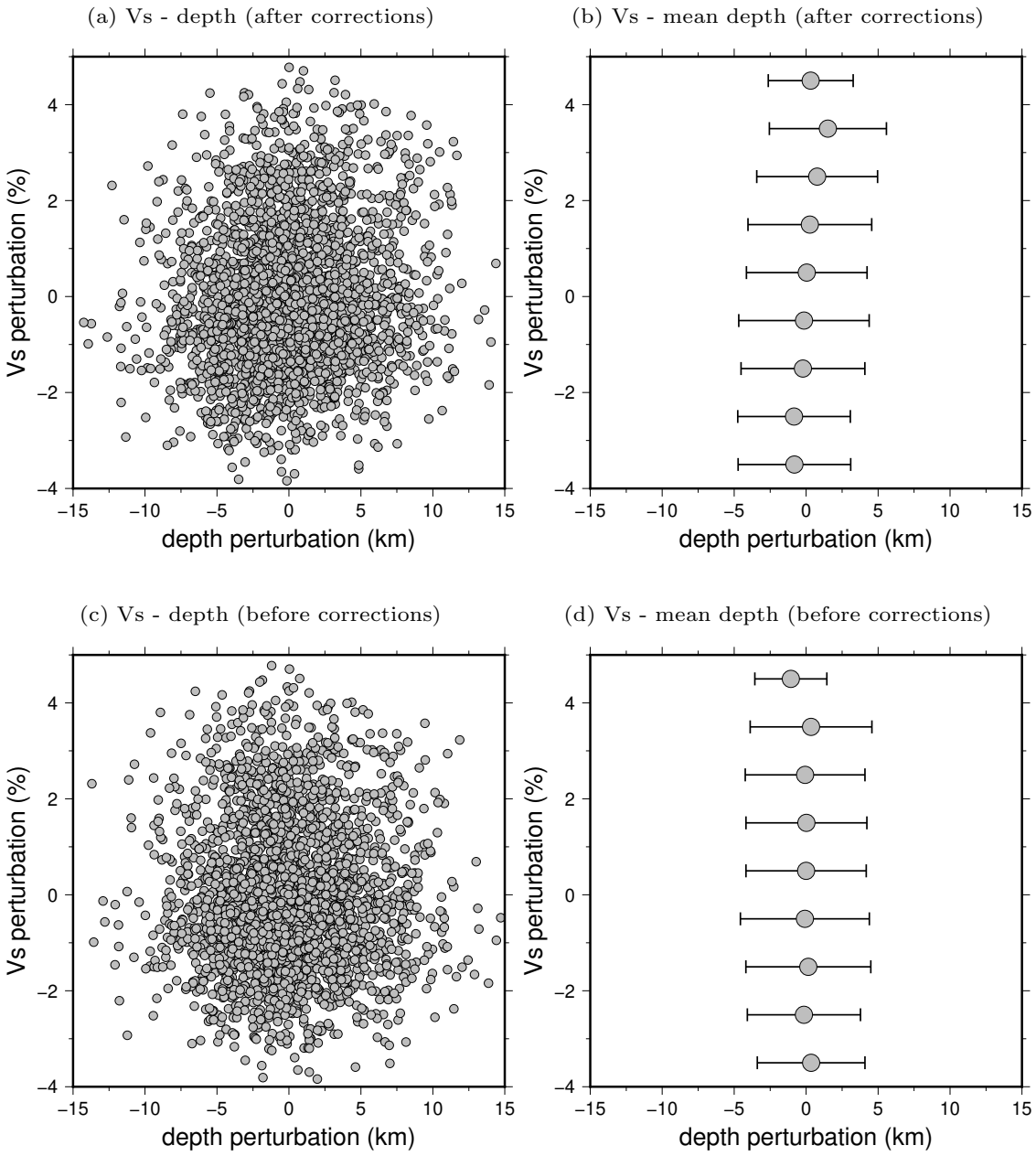

Figure 4.9: **(No) correlation between S wavespeed perturbations and the 220-km discontinuity depth perturbations.** **(a)** (weak) correlation between S wavespeed perturbations and the 220-km depth perturbations. The average S-wave speed perturbations are calculated from model S40RTS, averaged between perturbations in the upper mantle from 100 to 300 km depth. **(b)** same as **(a)** but for the mean discontinuity depth perturbations averaged over regions with the same S-wave speed perturbations. **(c)** and **(d)** are same as **(a)** and **(b)** but for the 220-km discontinuity depth perturbations obtained without crustal and mantle wavespeed corrections. There is no apparent correlations between S wavespeed perturbations in the upper mantle and the depths of the 220-km discontinuity.

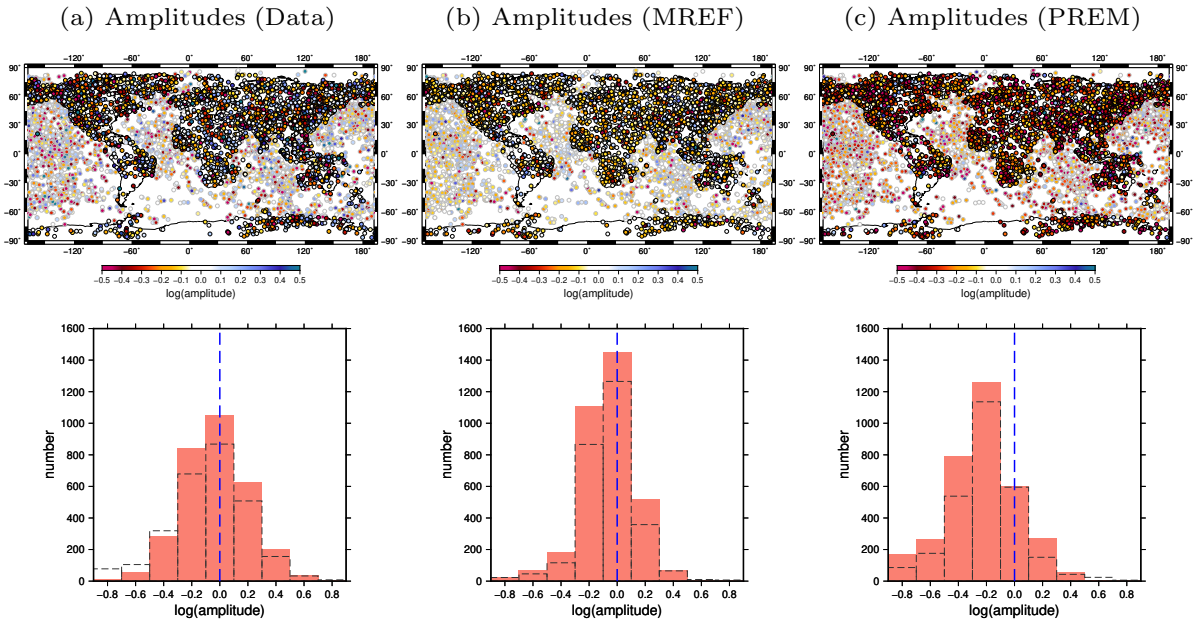

Figure 4.10: **Amplitude measurements of $S_{220}S$ waves.** Panel **(a)**, amplitude measurements $\gamma =$ minimum $[\log(A_{S_{\mathrm{LAB}}S}/A_{S_{410}S}), \log(A_{S_{\mathrm{LAB}}S}/A_{S_{660}S})]$ plotted in mapview (top) and histogram (bottom), respectively. In the top mapview, amplitude measurements of the continental data are plotted with black outlines while the oceanic measurements are plotted with gray outlines. In the bottom histograms, amplitude measurements of the continental data are plotted in red while the oceanic data are plotted as back, dashed lines. **(b)** and **(c)** are same as **(a)** but for synthetic SS precursors in model MREF and PREM, respectively. The mean amplitudes of the observed $S_{220}S$ waves in **(a)** are close to the MREF synthetics in **(b)** while PREM synthetics underpredict the amplitudes of the observed $S_{220}S$ waves.

(a) Continental stacks

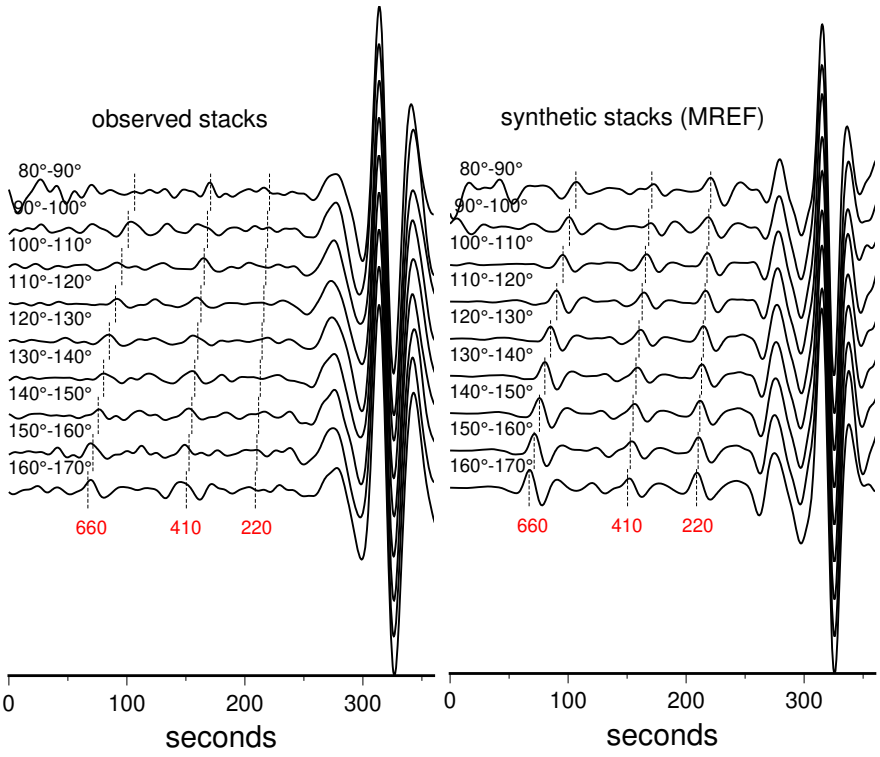

(b) Oceanic stacks

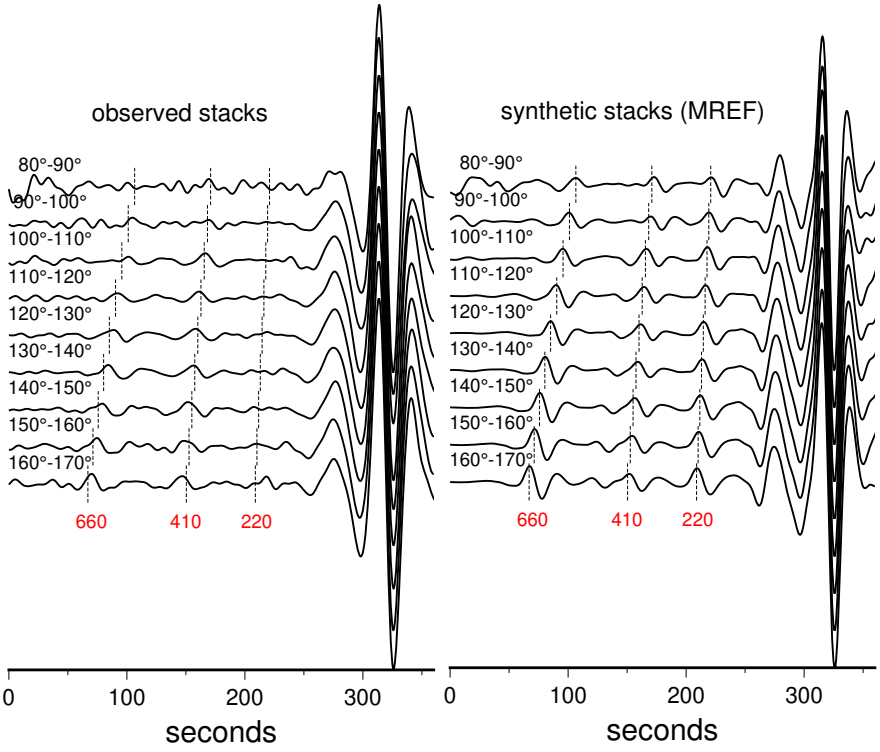

Figure 4.11: (a) stacks of observed (left) and synthetic (right) seismograms with SS bounce points in continental regions. The synthetic seismograms are calculated in model MREF. Seismograms in every 10-degree epicentral distance intervals in the global dataset are included to build the stacks. The bottom panel is the same but for the stacks using oceanic data. Unlike the $S_{410}S$ and the $S_{660}S$ waves, the $S_{220}S$ phase is weak or absent on the majority of the global stacks.

(a) Geographical stacks

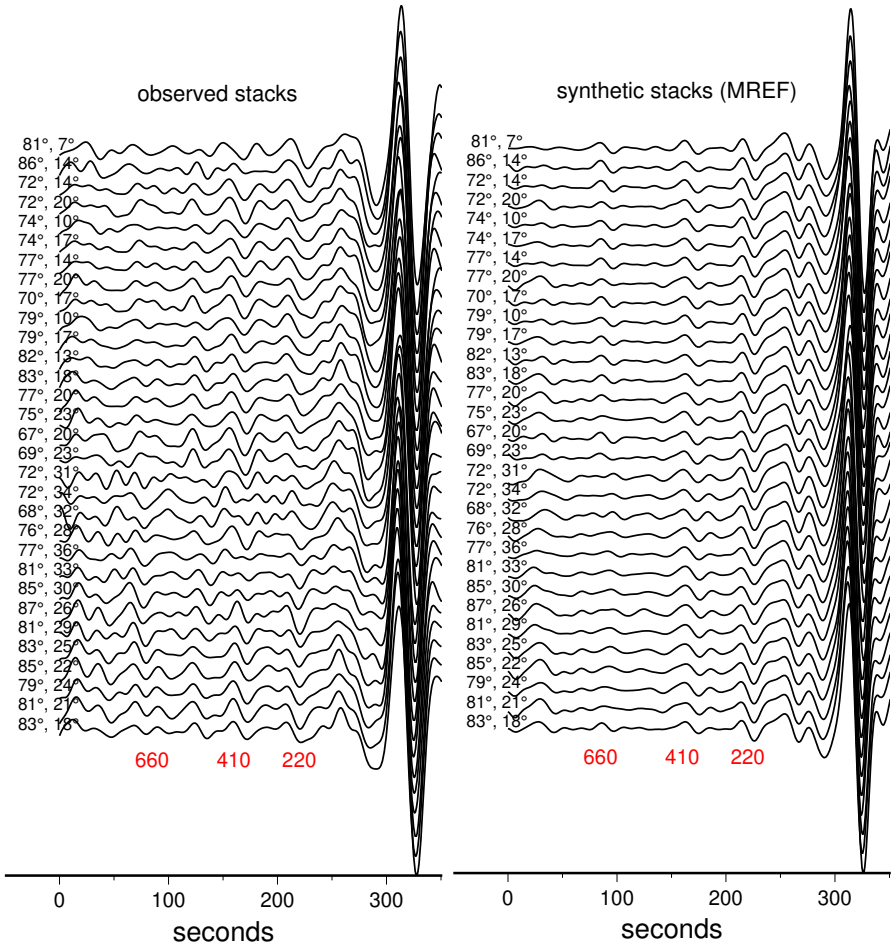

(b) Standard deviations

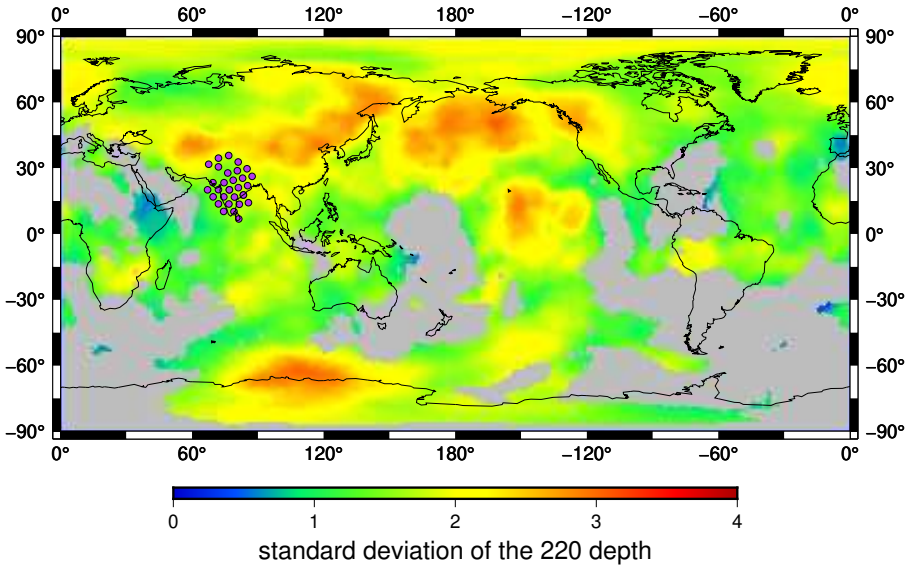

Figure 4.12: Example regional stacks in which strong $S_{220}S$ waves are observed on the stacked seismograms. Panel (a) shows example geographic stacks at grid points shown in (b) where standard deviations of the 220-km discontinuity depth are small. Observed and synthetic seismograms within a 10° circle distance around each grid points have been used to calculate the observed (left) and synthetic (right) stacks, respectively. (b) shows the location of the grid points plotted on top of the standard deviations of the 220-km discontinuity depths obtained from finite frequency tomography.

(a) Geographical stacks

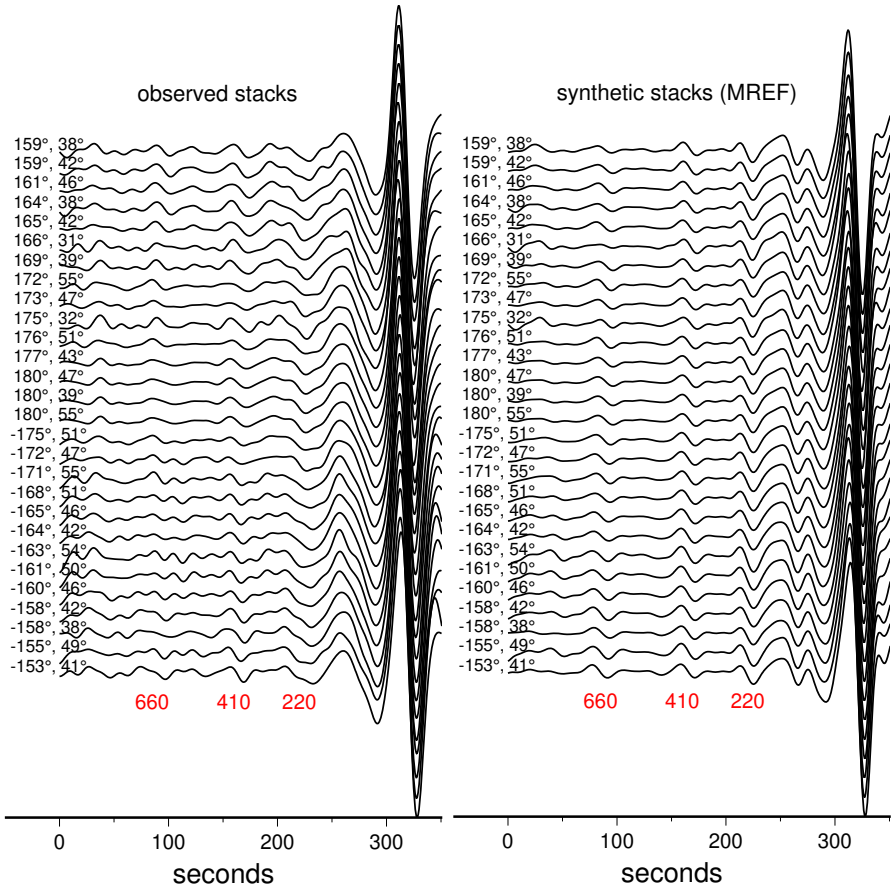

(b) Standard deviations

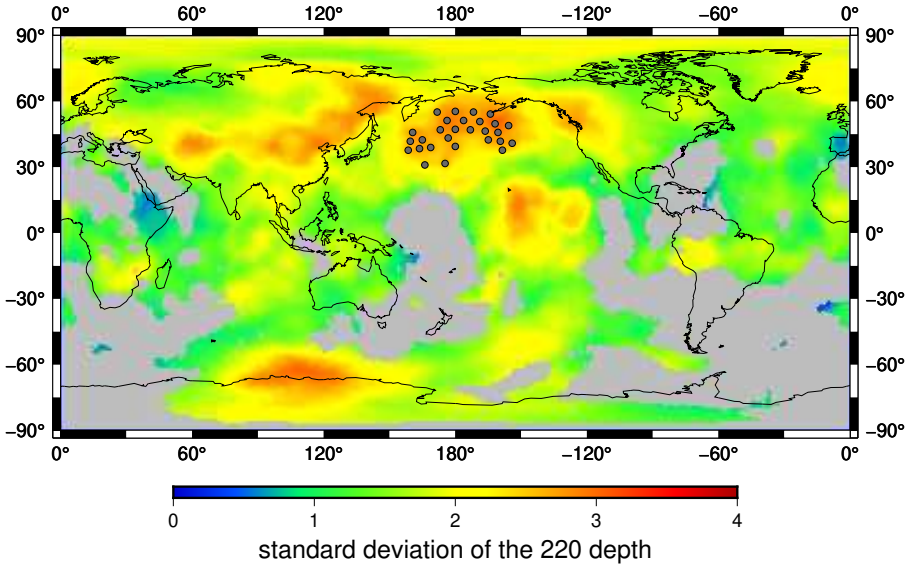

Figure 4.13: Similar to Figure 10, but for weak stacks in regions where large 220-km depth variations are observed. Panel (a) shows example stacks of observed and synthetic seismograms, respectively. (b) locations of the grid points where stacks are calculated. These grid points are located in regions with large lateral depth variations in the 220-km discontinuity.

Bibliography

[1] Gutenberg, B. The asthenosphere low-velocity layer. *Annals of Geophysics* **12**, 439–460 (1959).

[2] Boschi, L. & Ekström, G. New images of the earth's upper mantle from measurements of surface wave phase velocity anomalies. *Journal of Geophysical Research: Solid Earth* **107**, ESE–1 (2002).

[3] Nettles, M. & Dziewoński, A. M. Radially anisotropic shear velocity structure of the upper mantle globally and beneath north america. *Journal of Geophysical Research: Solid Earth* **113** (2008).

[4] Sifré, D. *et al.* Electrical conductivity during incipient melting in the oceanic low-velocity zone. *Nature* **509**, 81–85 (2014).

[5] Debayle, E., Bodin, T., Durand, S. & Ricard, Y. Seismic evidence for partial melt below tectonic plates. *Nature* **586**, 555–559 (2020).

[6] Thybo, H. The heterogeneous upper mantle low velocity zone. *Tectonophysics* **416**, 53–79 (2006).

[7] Richards, M. A. & Lenardic, A. The cathles parameter (ct): a geodynamic definition of the asthenosphere and implications for the nature of plate tectonics. *Geochemistry, Geophysics, Geosystems* **19**, 4858–4875 (2018).

[8] Sun, S. & Zhou, Y. Age-independent oceanic plate thickness and asthenosphere melting from ss precursor imaging. *Journal of Geophysical Research: Solid Earth* **128**, e2022JB024805 (2023).

[9] Lehmann, I. Velocities of longitudinal waves in the upper part of the earth's mantle. In *Annales de géophysique*, vol. 15, 93 (1959).

[10] Lehmann, I. S and the structure of the upper mantle. *Geophysical Journal International* **4**, 124–138 (1961).

[11] Dziewonski, A. M. & Anderson, D. L. Preliminary reference earth model. *Physics of the earth and planetary interiors* **25**, 297–356 (1981).

[12] Hales, A. Upper mantle models and the thickness of the continental lithosphere. *Geophysical Journal International* **105**, 355–363 (1991).

[13] Hales, A., Muirhead, K., Rynn, J. & Gettrust, J. Upper-mantle travel times in australia—a preliminary report. *Physics of the Earth and Planetary Interiors* **11**, 109–118 (1975).

[14] Leven, J., Jackson, I. & Ringwood, A. Upper mantle seismic anisotropy and lithospheric decoupling. *Nature* **289**, 234–239 (1981).

[15] Drummond, B., Muirhead, K. & Hales, A. Evidence for a seismic discontinuity near 200km depth under a continental margin. *Geophysical Journal International* **70**, 67–77 (1982).

[16] Vidale, J. E. & Benz, H. M. Upper-mantle seismic discontinuities and the thermal structure of subduction zones. *Nature* **356**, 678–683 (1992).

[17] Goncz, J. H. & Cleary, J. R. Variations in the structure of the upper mantle beneath australia, from rayleigh wave observations. *Geophysical Journal International* **44**, 507–516 (1976).

[18] Dalton, C. A., Bao, X. & Ma, Z. The thermal structure of cratonic lithosphere from global rayleigh wave attenuation. *Earth and Planetary Science Letters* **457**, 250–262 (2017).

[19] Vinnik, L. *et al.* The lithosphere, lab, lvz and lehmann discontinuity under central fennoscandia from receiver functions. *Tectonophysics* **667**, 189–198 (2016).

[20] He, C. Upwelling mantle plume and lithospheric delamination beneath the north china craton. *Physics of the Earth and Planetary Interiors* **306**, 106548 (2020).

[21] Kind, R., Yuan, X., Mechie, J. & Sodoudi, F. Structure of the upper mantle in the north-western and central united states from usarray s-receiver functions. *Solid Earth* **6**, 957–970 (2015).

[22] Gaherty, J. B. & Jordan, T. H. Lehmann discontinuity as the base of an anisotropic layer beneath continents. *Science* **268**, 1468–1471 (1995).

[23] Revenaugh, J. & Jordan, T. H. Mantle layering from scs reverberations: 3. the upper mantle. *Journal of Geophysical Research: Solid Earth* **96**, 19781–19810 (1991).

[24] Revenaugh, J. & Sipkin, S. A. Mantle discontinuity structure beneath china. *Journal of Geophysical Research: Solid Earth* **99**, 21911–21927 (1994).

[25] Calò, M., Bodin, T. & Romanowicz, B. Layered structure in the upper mantle across north america from joint inversion of long and short period seismic data. *Earth and Planetary Science Letters* **449**, 164–175 (2016).

[26] Cara, M. Lateral variations of s velocity in the upper mantle from higher rayleigh modes. *Geophysical Journal International* **57**, 649–670 (1979).

[27] Shen, Y., Sheehan, A. F., Dueker, K. G., de Groot-Hedlin, C. & Gilbert, H. Mantle discontinuity structure beneath the southern east pacific rise from p-to-s converted phases. *Science* **280**, 1232–1235 (1998).

[28] Rost, S. & Weber, M. A reflector at 200 km depth beneath the northwest pacific. *Geophysical Journal International* **147**, 12–28 (2001).

[29] Tkalčić, H., Flanagan, M. P. & Cormier, V. F. Observation of near-podal P'P' precursors: Evidence for back scattering from the 150–220 km zone in the earth's upper mantle. *Geophysical research letters* **33** (2006).

[30] Shearer, P. M. Constraints on upper mantle discontinuities from observations of long-period reflected and converted phases. *Journal of Geophysical Research: Solid Earth* **96**, 18147–18182 (1991).

[31] Deuss, A. Global observations of mantle discontinuities using ss and pp precursors. *Surveys in geophysics* **30**, 301–326 (2009).

[32] Gu, Y. J., Dziewonski, A. M. & Ekström, G. Preferential detection of the lehmann discontinuity beneath continents. *Geophysical Research Letters* **28**, 4655–4658 (2001).

[33] Deuss, A. & Woodhouse, J. H. A systematic search for mantle discontinuities using ss-precursors. *Geophysical Research Letters* **29**, 90–1 (2002).

[34] Sun, S. & Zhou, Y. Ss precursor imaging reveals a global oceanic asthenosphere modulated by sea-floor spreading. *In submission* (2023).

[35] Liu, K. & Zhou, Y. Travelling-wave green tensor and near-field rayleigh-wave sensitivity. *Geophysical Supplements to the Monthly Notices of the Royal Astronomical Society* **205**, 134–145 (2016).

[36] Zhou, Y., Dahlen, F., Nolet, G. & Laske, G. Finite-frequency effects in global surface-wave tomography. *Geophysical Journal International* **163**, 1087–1111 (2005).

[37] Zhou, Y. Anomalous mantle transition zone beneath the yellowstone hotspot track. *Nature Geoscience* **11**, 449–453 (2018).

[38] Guo, Z. & Zhou, Y. Stagnant slabs and their return flows from finite-frequency tomography of the 410-km and 660-km discontinuities. *Journal of Geophysical Research: Solid Earth* **126**, e2020JB021099 (2021).

[39] Fang, Y., Zhou, Y. & Yao, Z. Model misfit minimization. *Bulletin of the Seismological Society of America* **109**, 1729–1737 (2019).

[40] Guo, Z. & Zhou, Y. Finite-frequency imaging of the global 410-and 660-km discontinuities using ss precursors. *Geophysical Journal International* **220**, 1978–1994 (2020).

[41] Hansen, P. C. The truncatedsvd as a method for regularization. *BIT Numerical Mathematics* **27**, 534–553 (1987).

[42] Ritsema, J., Deuss, a. A., Van Heijst, H. & Woodhouse, J. S40rts: a degree-40 shear-velocity model for the mantle from new rayleigh wave dispersion, teleseismic traveltime and normal-mode splitting function measurements. *Geophysical Journal International* **184**, 1223–1236 (2011).

[43] Laske, G., Masters, G., Ma, Z. & Pasyanos, M. Update on crust1. 0—a 1-degree global model of earth's crust. In *Geophys. Res. Abstr*, vol. 15, 2658 (2013).

[44] Hua, J., Fischer, K. M., Becker, T. W., Gazel, E. & Hirth, G. Asthenospheric low-velocity zone consistent with globally prevalent partial melting. *Nature Geoscience* **16**, 175–181 (2023).

[45] Deuss, A. & Woodhouse, J. H. The nature of the lehmann discontinuity from its seismological clapeyron slopes. *Earth and Planetary Science Letters* **225**, 295–304 (2004).

[46] Heit, B., Yuan, X., Bianchi, M., Kind, R. & Gossler, J. Study of the lithospheric and upper-mantle discontinuities beneath eastern asia by ss precursors. *Geophysical Journal International* **183**, 252–266 (2010).

[47] Knapmeyer-Endrun, B., Krüger, F., Geissler, W. H., Group, P. W. *et al.* Upper mantle structure across the trans-european suture zone imaged by s-receiver functions. *Earth and Planetary Science Letters* **458**, 429–441 (2017).

[48] Kind, R. & Yuan, X. Perspectives of the s-receiver-function method to image upper mantle discontinuities. *Lithospheric Discontinuities* 139–154 (2018).

[49] Kind, R., Mooney, W. D. & Yuan, X. New insights into the structural elements of the upper mantle beneath the contiguous united states from s-to-p converted seismic waves. *Geophysical Journal International* **222**, 646–659 (2020).

[50] Taira, T. & Yoshizawa, K. Upper-mantle discontinuities beneath australia from trans-dimensional bayesian inversions using multimode surface waves and receiver functions. *Geophysical Journal International* **223**, 2085–2100 (2020).

[51] Pugh, S., Boyce, A., Bastow, I. D., Ebinger, C. & Cottaar, S. Multigenetic origin of the x-discontinuity below continents: Insights from african receiver functions. *Geochemistry, Geophysics, Geosystems* **24**, e2022GC010782 (2023).

[52] Pugh, S., Jenkins, J., Boyce, A. & Cottaar, S. Global receiver function observations of the x-discontinuity reveal recycled basalt beneath hotspots. *Earth and Planetary Science Letters* **561**, 116813 (2021).

[53] Schmerr, N. Imaging mantle heterogeneity with upper mantle seismic discontinuities. *The Earth's heterogeneous mantle: A geophysical, geodynamical, and geochemical perspective* 79–104 (2015).

[54] Bagley, B. & Revenaugh, J. Upper mantle seismic shear discontinuities of the pacific. *Journal of Geophysical Research: Solid Earth* **113** (2008).

[55] Srinu, U. *et al.* X-discontinuity beneath the indian shield—evidence for remnant tethyan oceanic lithosphere in the mantle. *Journal of Geophysical Research: Solid Earth* **126**, e2021JB021890 (2021).

[56] Kemp, M., Jenkins, J., Maclennan, J. & Cottaar, S. X-discontinuity and transition zone structure beneath hawaii suggests a heterogeneous plume. *Earth and Planetary Science Letters* **527**, 115781 (2019).

[57] Molnar, P. & Tapponnier, P. Cenozoic tectonics of asia: Effects of a continental collision: Features of recent continental tectonics in asia can be interpreted as results of the india-eurasia collision. *science* **189**, 419–426 (1975).

[58] Yin, A. Cenozoic tectonic evolution of asia: A preliminary synthesis. *Tectonophysics* **488**, 293–325 (2010).

[59] Ma, J., Bunge, H.-P., Fichtner, A., Chang, S.-J. & Tian, Y. Structure and dynamics of lithosphere and asthenosphere in asia: A seismological perspective. *Geophysical Research Letters* **50**, e2022GL101704 (2023).

[60] Zhao, D., Lei, J., Inoue, T., Yamada, A. & Gao, S. S. Deep structure and origin of the baikal rift zone. *Earth and Planetary Science Letters* **243**, 681–691 (2006).

[61] Bonvalot, S. *et al.* World gravity map (wgm) 2012. [model]. formater. https://doi.org/10.18168/23. *WGM2012* (2012).

[62] Oceanic, N. & Administration, A. 5-minute gridded global relief data (etopo5). doi:10.7289/v5d798bf. *National Geophysical Data Center* (1993).

Appendices

Appendix A

Supplementary Figures Used in Chapter 2

This chapter contains 15 supplementary figures used in Chapter 2.

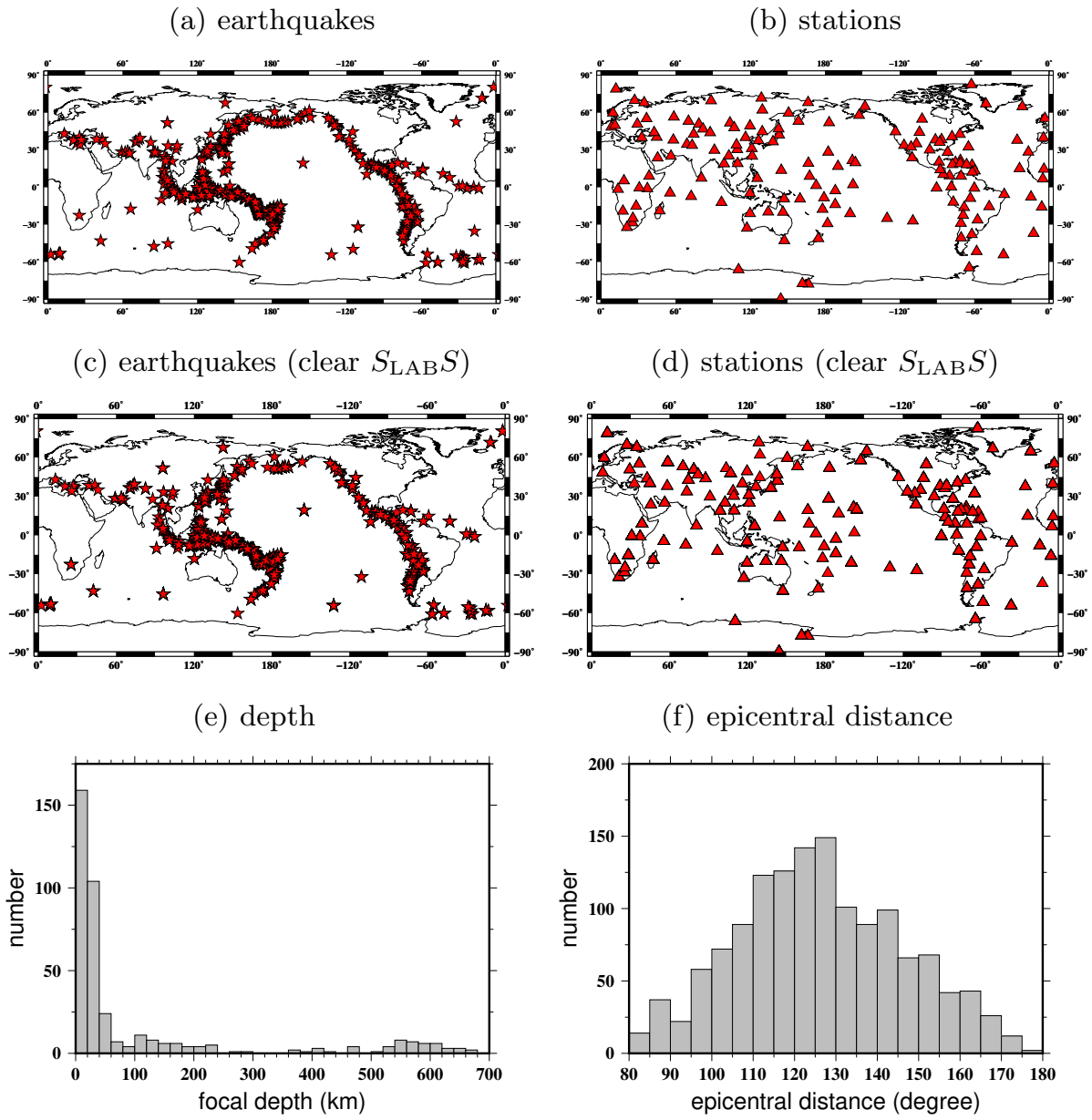

Figure A.1: (a) and (b) are distributions of the 543 earthquakes and 151 GSN stations used in this study. (c) and (d) are distributions of the 395 earthquakes and 144 GSN stations in the subset in which large $S_{\mathrm{LAB}}S$ waves were observed. (e) and (f) are histograms of the focal depths and epicentral distances of the same subset.

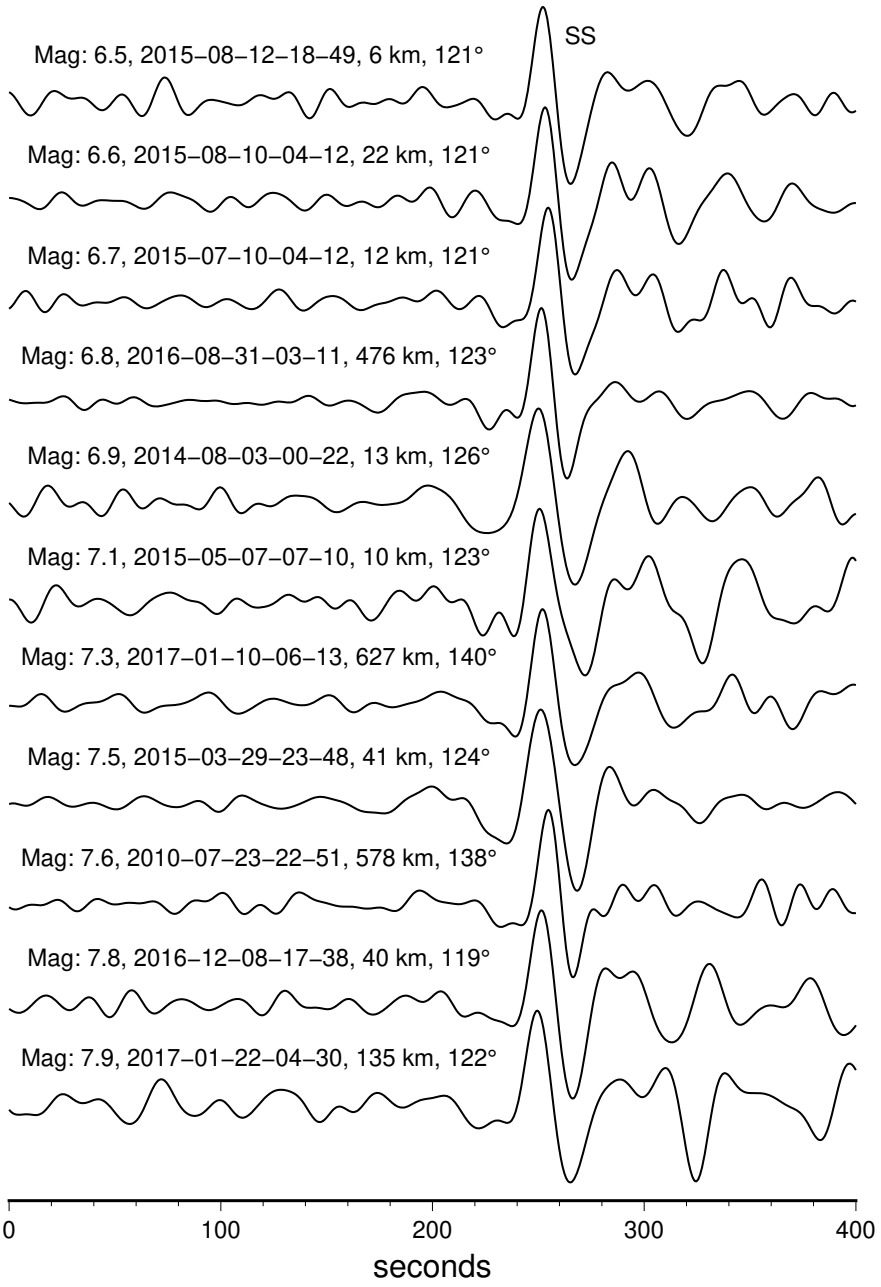

Figure A.2: Example SS seismograms with simple source time functions recorded at a GSN station DWPF (https://doi.org/10.7914/SN/IU) for earthquakes with different magnitudes ranging from 6.5 to 7.9. The event magnitude, date/time, depth and epicentral distance are denoted. The SS waves have been aligned with polarities corrected for better illustration. The dataset used in this study includes 6,143 high-quality SS seismograms with bounce points in oceanic regions.

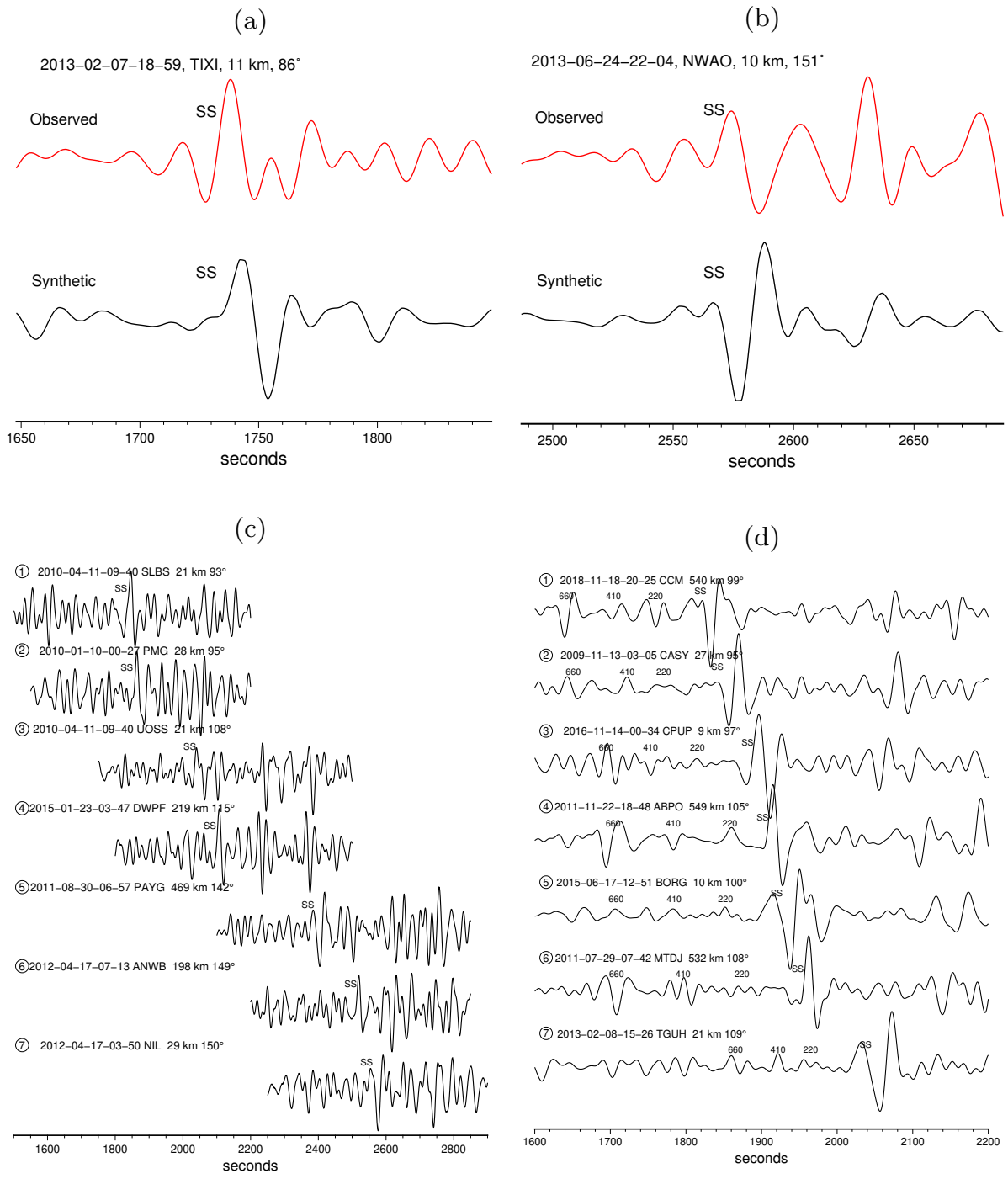

Figure A.3: (a) and (b) are example seismograms with SS waves significantly different from the synthetics. SS precursors on those seismograms are not used in this study. (c) example seismograms with noisy SS waves and precursors, SS precursors on those seismograms are not used in this study. (d) example seismograms with clear SS precursors but weak (or absent) $S_{\mathrm{LAB}}S$ waves, their bounce points are plotted in Figure 2.2.

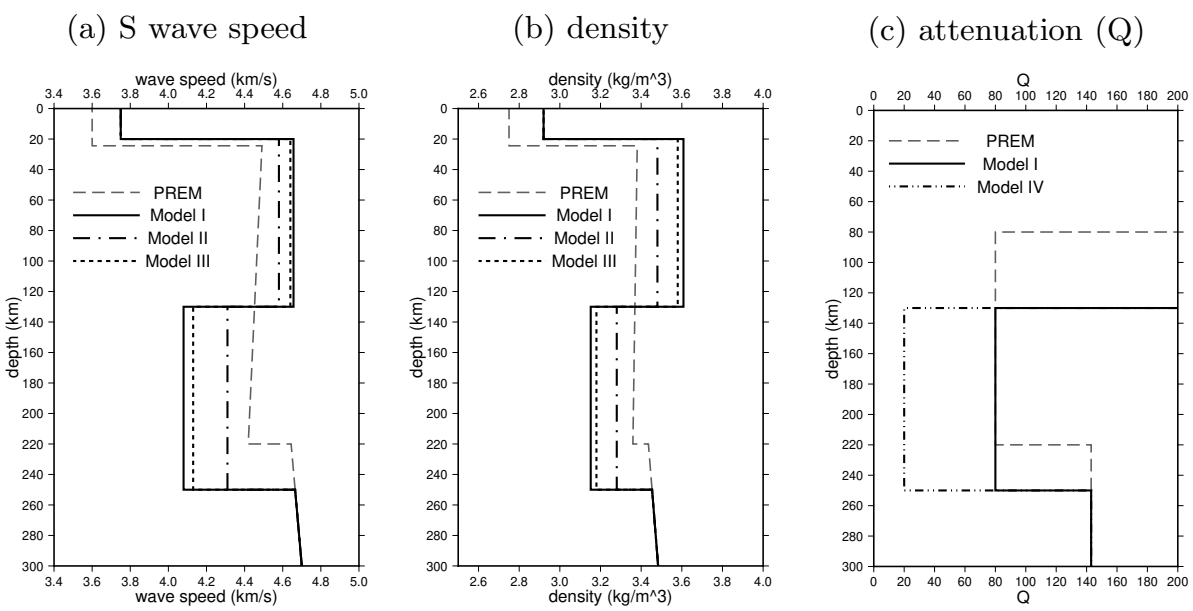

Figure A.4: 1-D reference earth models used in this study: PREM, Models I, II, III and IV. (a) S-wave speed profiles. The velocity contrast across the LAB is 12.5% in Model I, 6% in Model II and 11% in Model III. (b) density profiles of the models. The density is scaled with velocity in the uppermost 250 km in Models I-IV , with a scaling parameter of $\sim$0.77, similar to that in PREM, which varies between 0.75 and 0.78. (c) Seismic Q profiles of the models. $Q = 80$ in Model I at depths between 130 and 250 km and $Q = 20$ in Model IV at those depths. PREM Q values are plotted as the dashed line for reference.

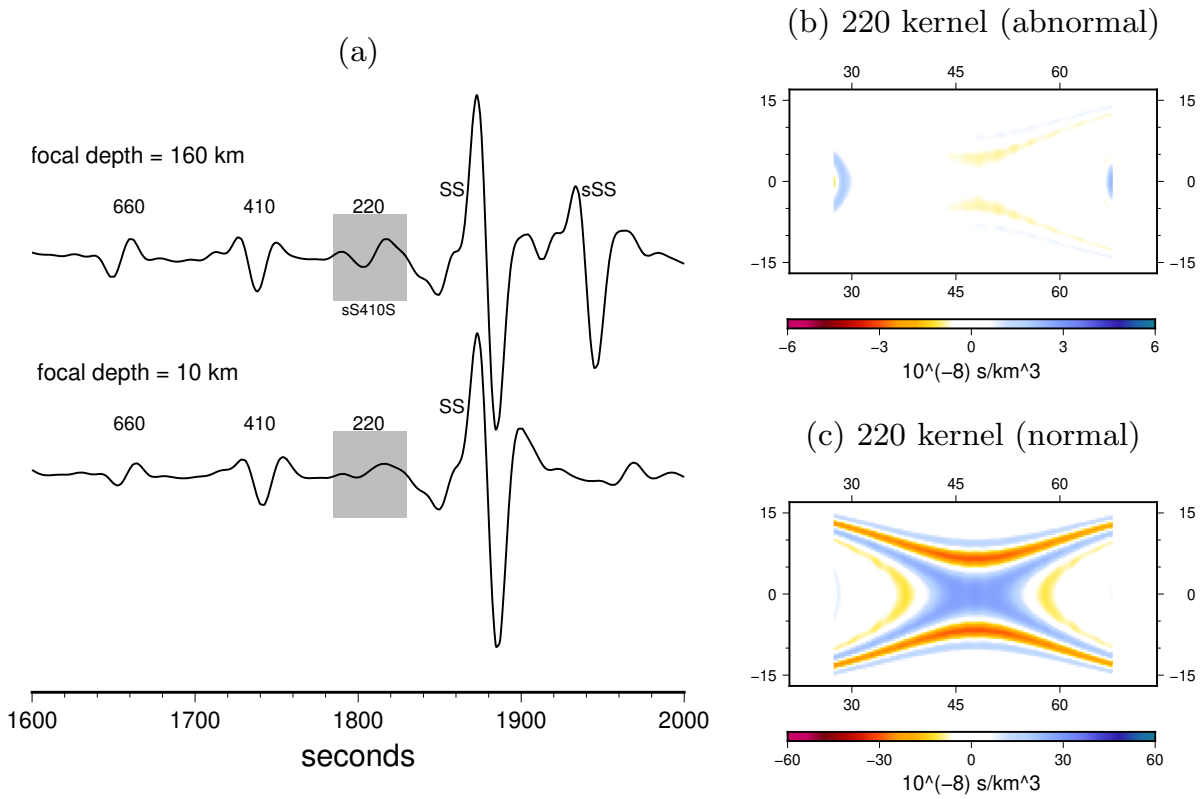

Figure A.5: (a) example seismograms with (top) and without (bottom) an interfering depth phase. The measurement windows (shaded) are centered at the expected arrival of the $S_{220}S$ waves. The epicentral distance is 96° and the depths of the earthquakes are denoted on each seismogram. The SS waves have been aligned and a strong depth phase sSS arrives after the main SS wave for the deep earthquake (depth=160 km). The precursor of the depth phase $sS_{410}S$ arrives about the same time as the the SS precursor $S_{220}S$. The calculated sensitivity kernel is abnormal when there is $sS_{410}S$ interference – the sensitivity is about 10 times smaller than values expected for an $S_{220}S$ wave. This is because the $sS_{410}S$ wave is not reflected at the 220-km discontinuity and therefore it has no sensitivity to depth perturbations of the 220-km discontinuity at the bounce point.

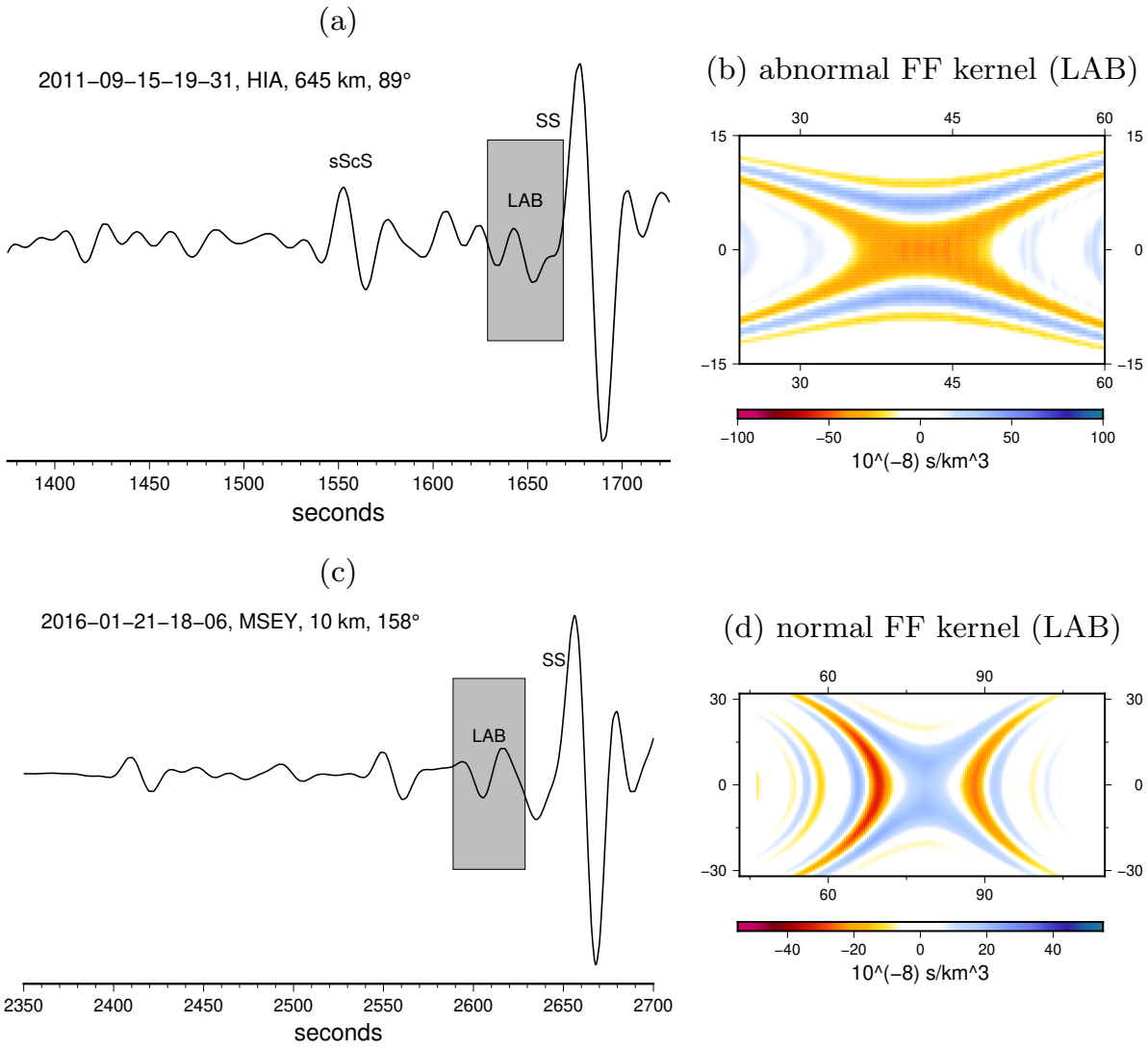

Figure A.6: Example traveltime sensitivity kernels with (top) and without (bottom) phase interference. (a) and (c) are synthetic seismograms with measurement windows (shaded) centered at the expected arrival of the $S_{\mathrm{LAB}}S$ waves, and (b) and (d) are the corresponding traveltime sensitivity kernels. (c) and (d) are the same as in Figure 2.4 (a) and (b). The interferences between the $S_{\mathrm{LAB}}S$ and $sScS$ coda waves (shallow multiples) in the measurement window in (a) result in a polarity change in the traveltime sensitivity in (b). The sensitivity kernels are always associated with measurement time windows not any particular seismic phases, and the kernels are used to identify possible phase interferences in measurement windows.

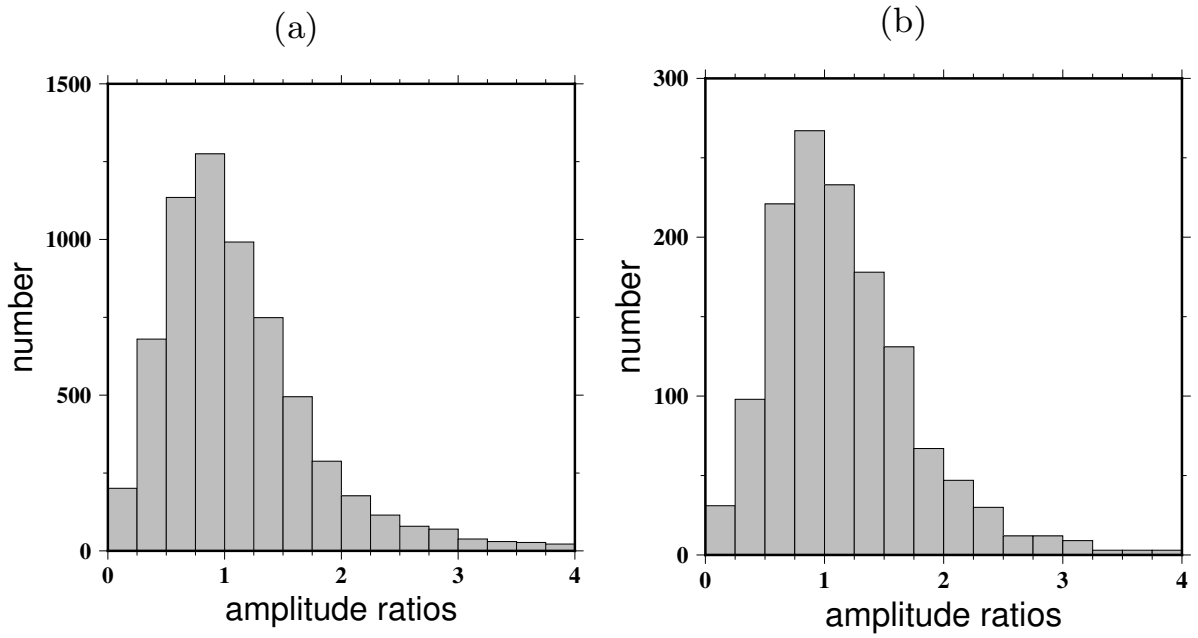

Figure A.7: (a) histogram of amplitude ratios between the observed and the synthetic SS waves for the entire dataset (6143 seismograms). (b) the same as (a) but for the subset (1380 seismograms) in which anomalously large $S_{\rm LAB}S$ were observed. The distribution of the SS amplitude measurements is very similar in (a) and (b), indicating that the observed large amplitudes of the $S_{\rm LAB}S$ waves in the subset are not a result of focusing caused by mantle heterogeneities because the focusing effects (anomalously large amplitudes) are not observed on the SS waves which travel through the same regions in the mantle sampled by the $S_{\rm LAB}S$ waves.

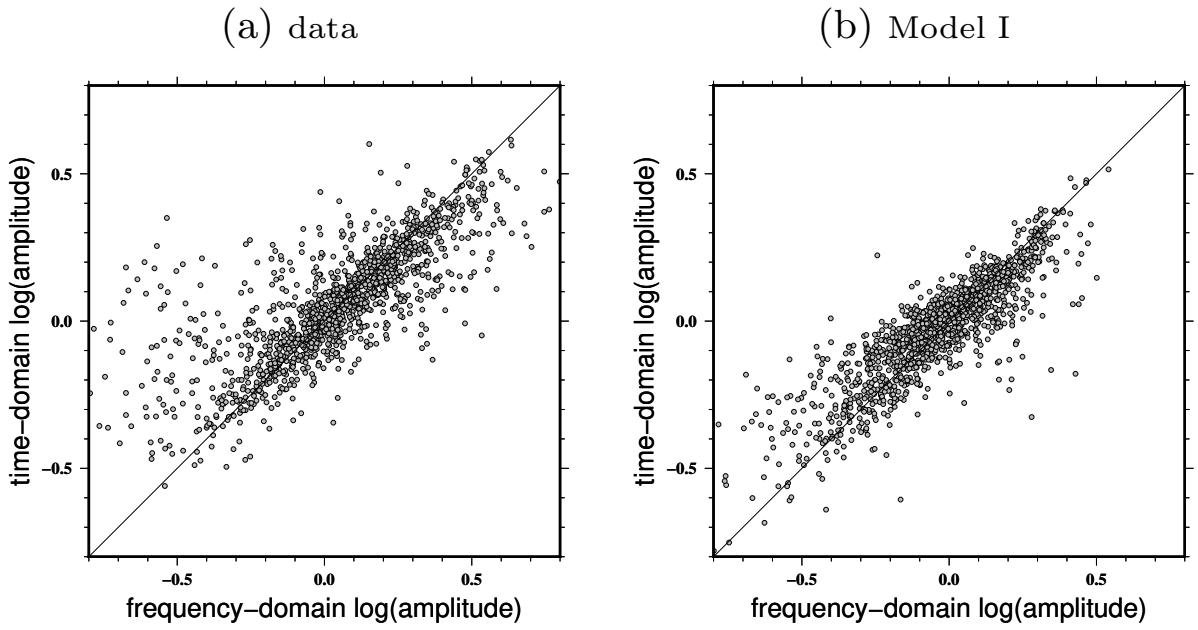

Figure A.8: Scatter plots of the LAB amplitude measurements made in the frequency domain versus those obtained in the time domain using envelope functions of the observed seismograms. (b) is the same as (a) but for measurements made on synthetic seismograms calculated for Model I. It is worth noting that the frequency-domain measurements are made at a period of 25 seconds while the envelope functions include much broader frequency content. In this paper, we focus on measurements at a period of 25 seconds, and the envelope function results are plotted for reference only. The 45° line with a slope of 1.0 is also plotted for reference only, it is not expected to be the best fitting line for the scatter plots.

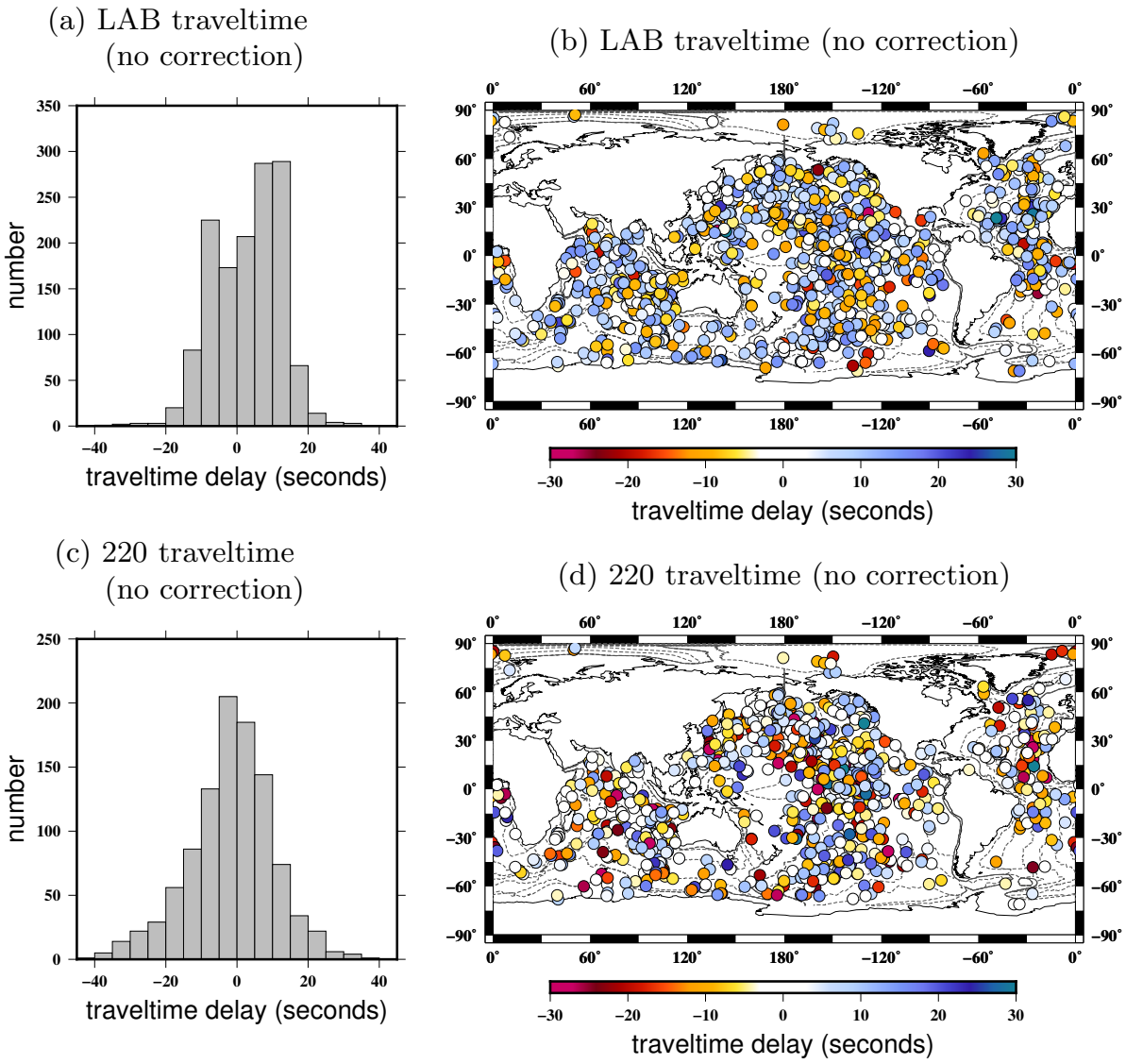

Figure A.9: The same as Figure 2.7 but for traveltime measurements made without 3-D crustal and mantle corrections.

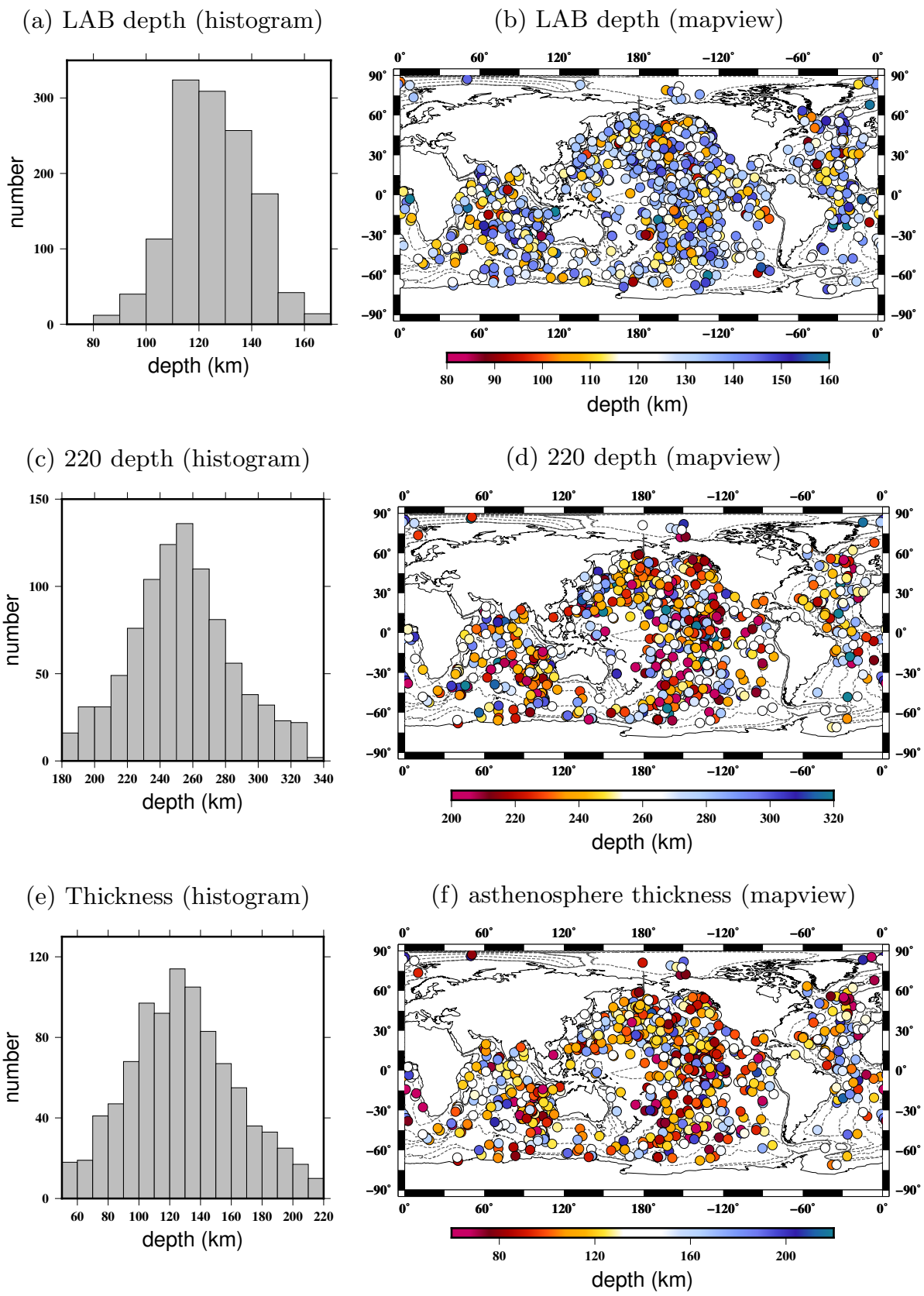

Figure A.10: The same as Figure 2.8 but for depths of the LAB and the 220-km discontinuity obtained using traveltime measurements without 3-D crust and mantle corrections.

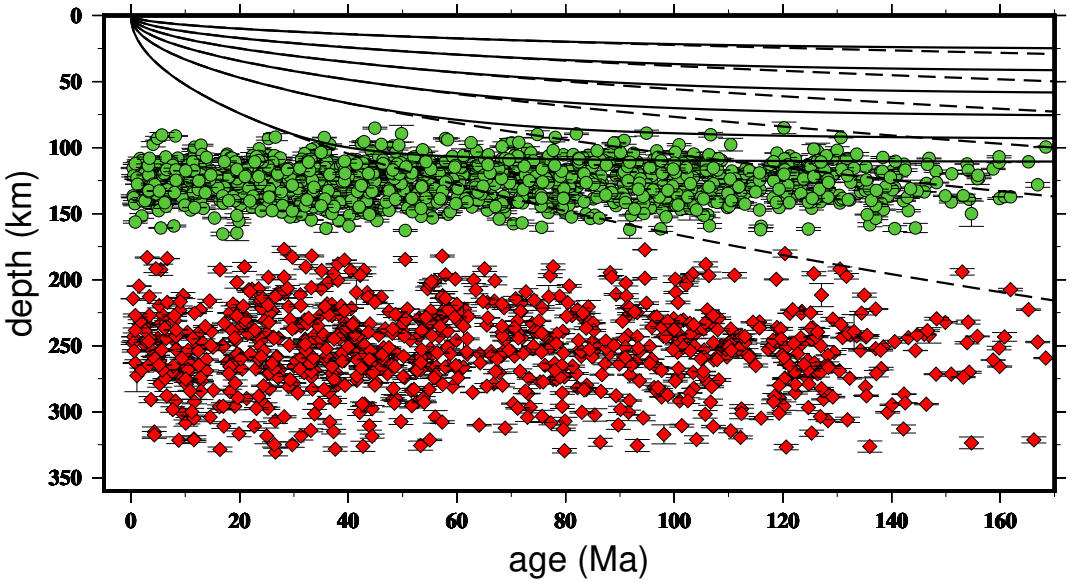

Figure A.11: The same as Figure 2.9 but for depths of the LAB and the 220-km discontinuity obtained using traveltime measurements without 3-D crust and mantle corrections.

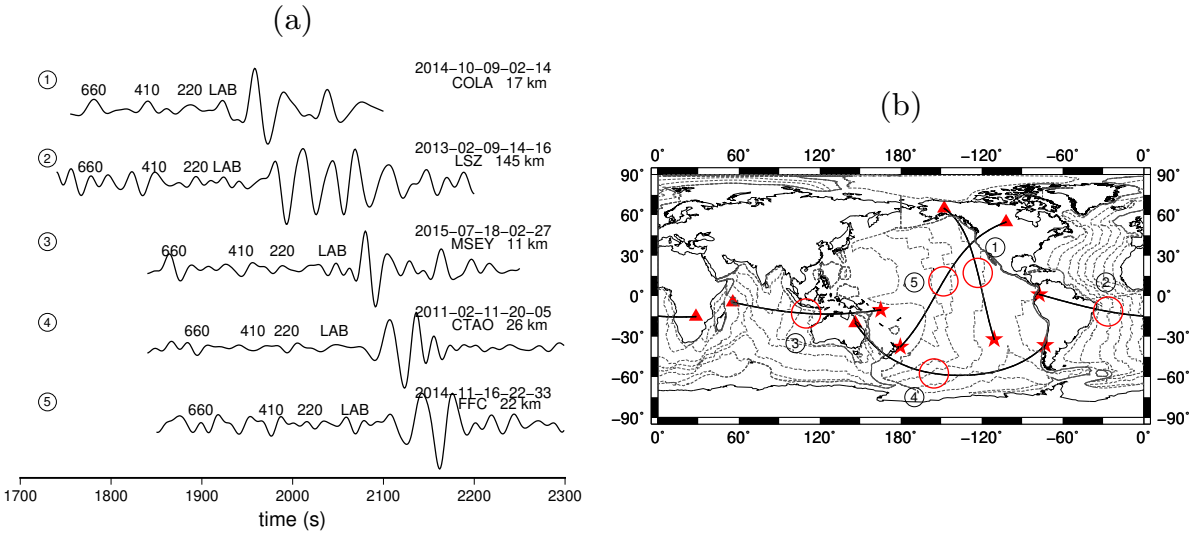

Figure A.12: (a), example radial-component seismograms with large-amplitude SS precursors. The corresponding geographic ray paths are plotted in (b).

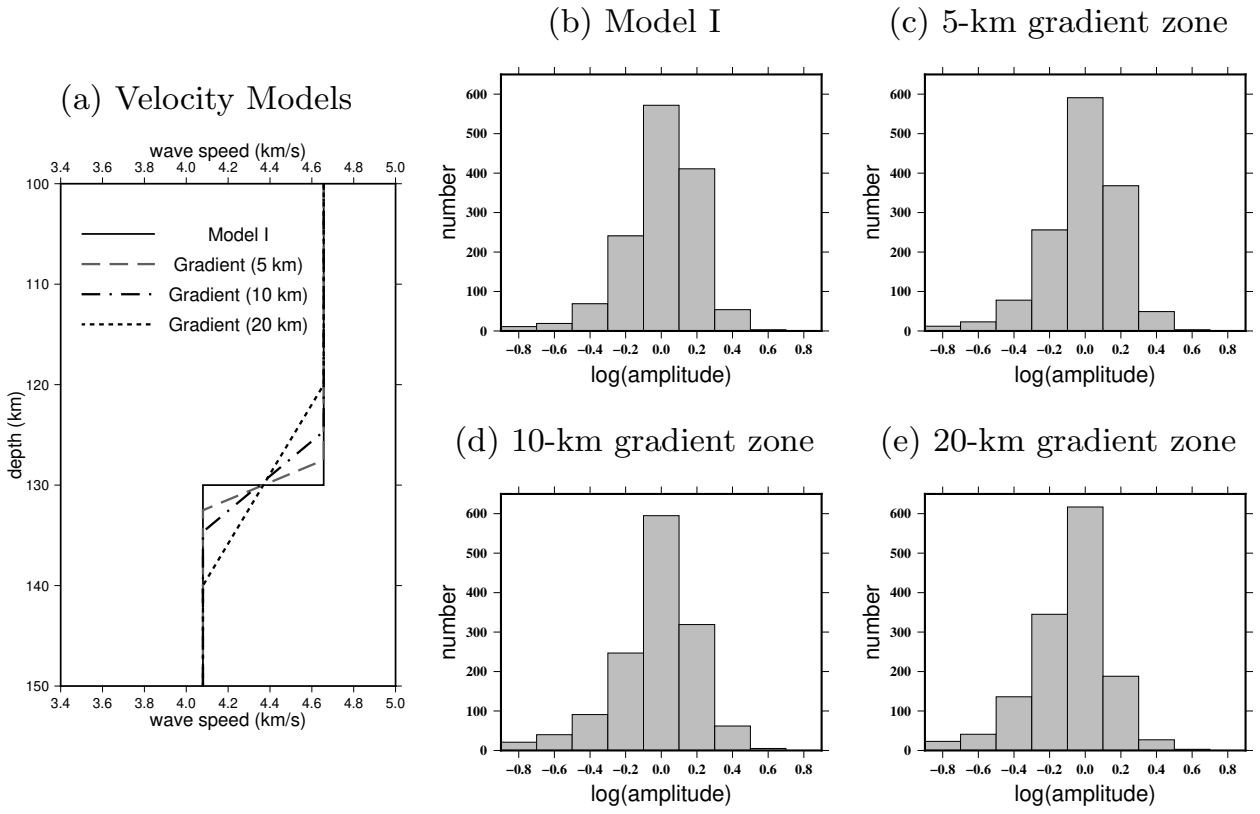

Figure A.13: (a) velocity models with a 12.5% of velocity change across the LAB at a depth of 130 km over a first-order discontinuity (Model I) as well as a gradient zone of 5 km, 10 km and 20 km. (b), (c), (d) and (e) are the corresponding histograms of the amplitude measurements γ= minimum $[\log (A_{S_{\rm LAB}S} / A_{S_{410}S}), \log(A_{S_{\rm LAB}S} / A_{S_{660}S})]$ made on the synthetic seismograms calculated for the four reference models as in Figure 2.6. The $S_{\rm LAB}S$ amplitudes become smaller when the velocity change occurs over a gradient zone. The average amplitude difference between a first-order discontinuity and a 5-km gradient zone for this dataset is about 2%, and it is about 6% if the velocity change occurs over a 10-km gradient zone. For a gradient zone over a depth range of 20 km, the mean $S_{\rm LAB}S$ amplitude is about 17% smaller than that for a first-order discontinuity, and the overall amplitude distribution also becomes significantly different. The calculations suggest that a 12.5% velocity change over a gradient zone of 5 km or less can explain the observed amplitude data in Figure 2.6.

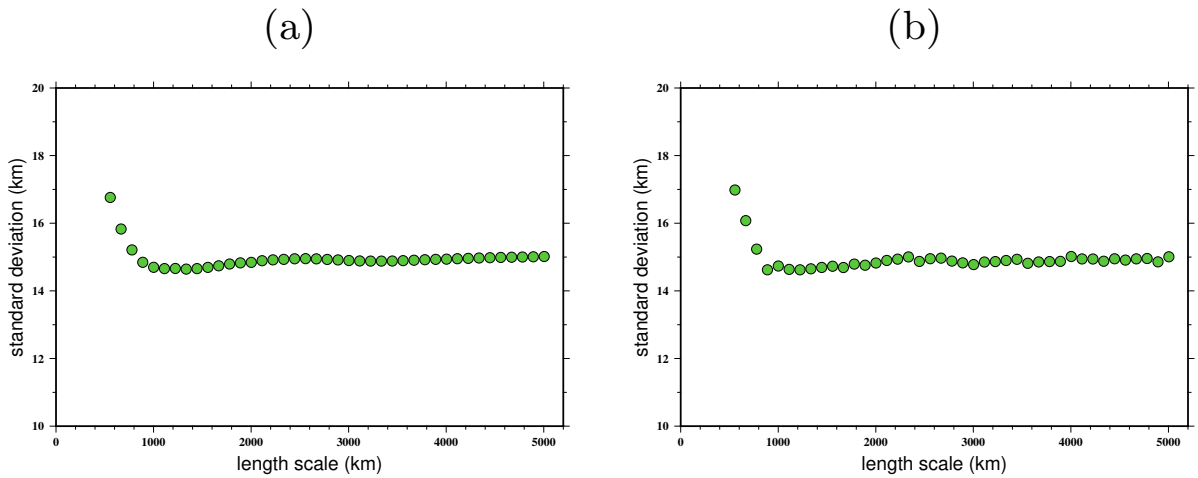

Figure A.14: (a) standard deviation at different length scales calculated for the LAB depths obtained in this study. The LAB depths are plotted in histogram and mapview in Figure 2.8 (a) and (b). The average standard deviations of the LAB depth are calculated for moving square cells over the global surface, plotted as a function of the length of the cell. The center of the cell moves at a one degree interval in latitude and longitude directions. Only cells that contain more than 30 data points are used in the calculation. (b) same as (a) but calculated for moving cells that are not overlapping.

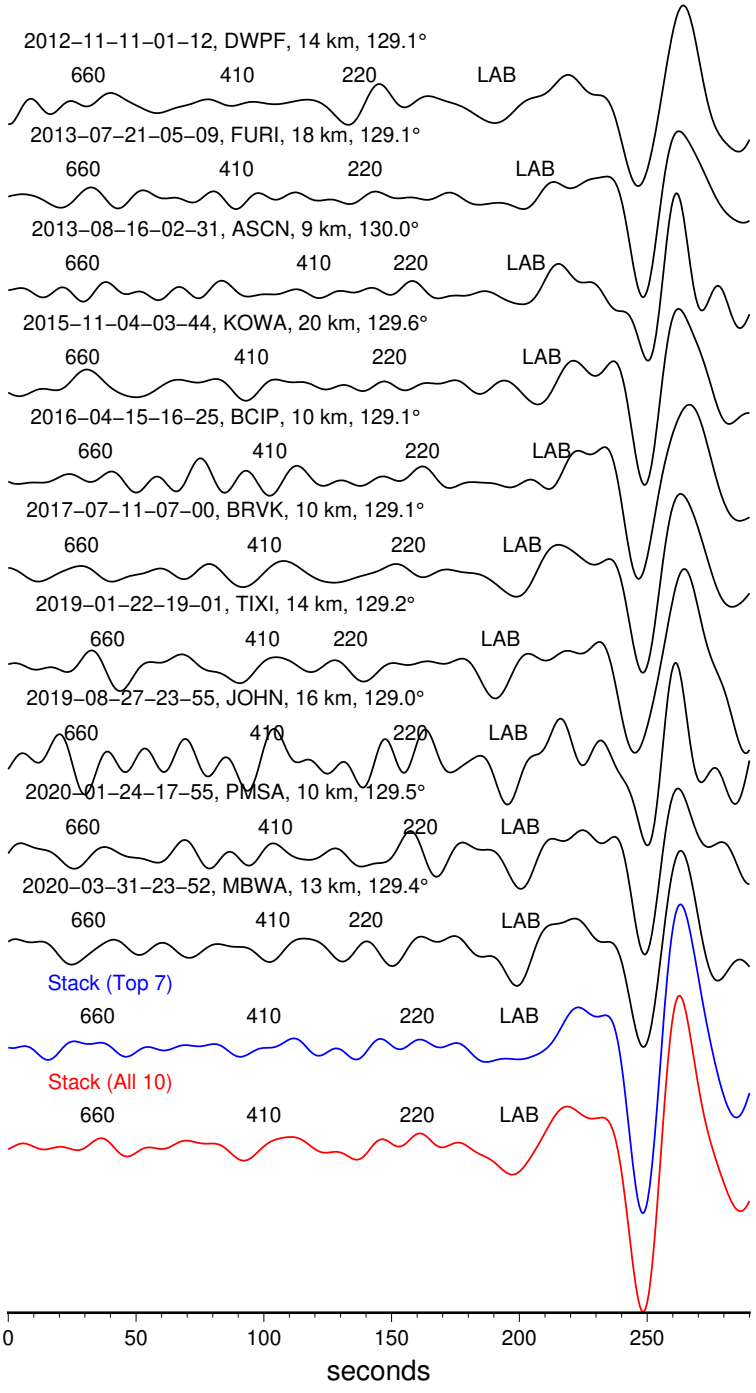

Figure A.15: A simple example illustrating the concept the large amplitudes of SS precursors may not be picked up in stacking results when large variations in SS precursor amplitudes and arrival times are present. The black seismograms are observed data with close epicentral distances between 129° and 130°. In a 1-D earth model, the SS precursors arrive at about the same time when the SS waves are aligned (with arrival time differences less than 0.2 seconds). We align the SS waves and produce a stack using only the top seven seismograms (blue) and a second stack using all ten seismograms (red). The SS precursors on the two stacked seismograms are significantly different.

Appendix B

Supplementary Figures Used in Chapter 3

This chapter contains 13 supplementary figures used in Chapter 3.

(a) All data

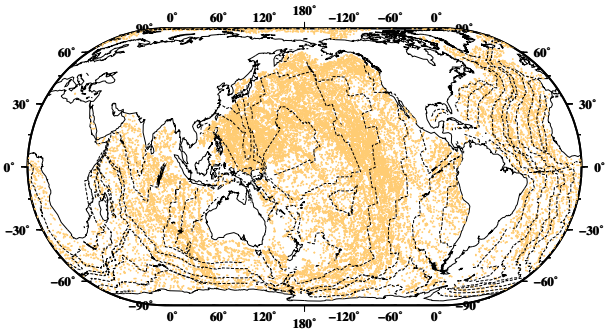

(b) Data with good SS

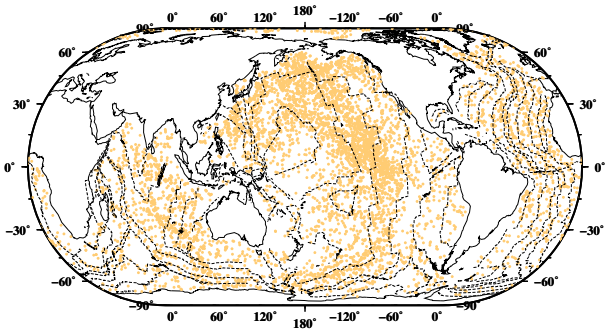

(c) Data with good $S_{220}S$

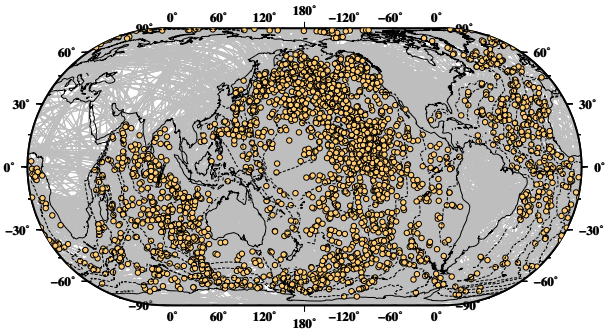

(d) Earthquakes and stations

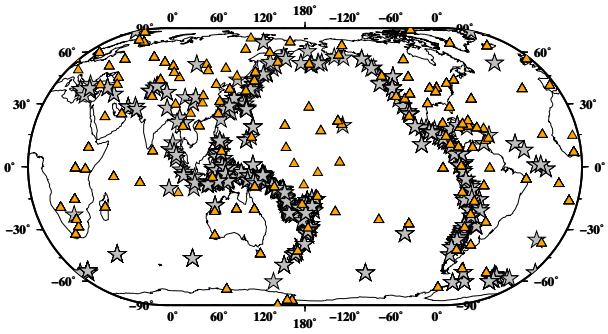

Figure B.1: (a) distribution of the bouncepoints of all 32,369 sets of SS data (orange dots) in the global oceans. Seafloor age countours are plotted in dash, black lines at 10, 50, 90, 130 and 170 Ma. (b) distribution of 6506 sets of data (orange dots) with good SS waves. (c) distribution of 2754 sets of data (orange dots) with good $S_{220}S$ waves plotted on top of the traveling paths (grey lines), same with Figure 3.1(a). The data set has a good coverage on all oceanic regions. (d) distribution of 459 earthquakes (gray stars) and 144 stations (orange triangles) for the 2754 sets of good $S_{220}S$ data used in this study.

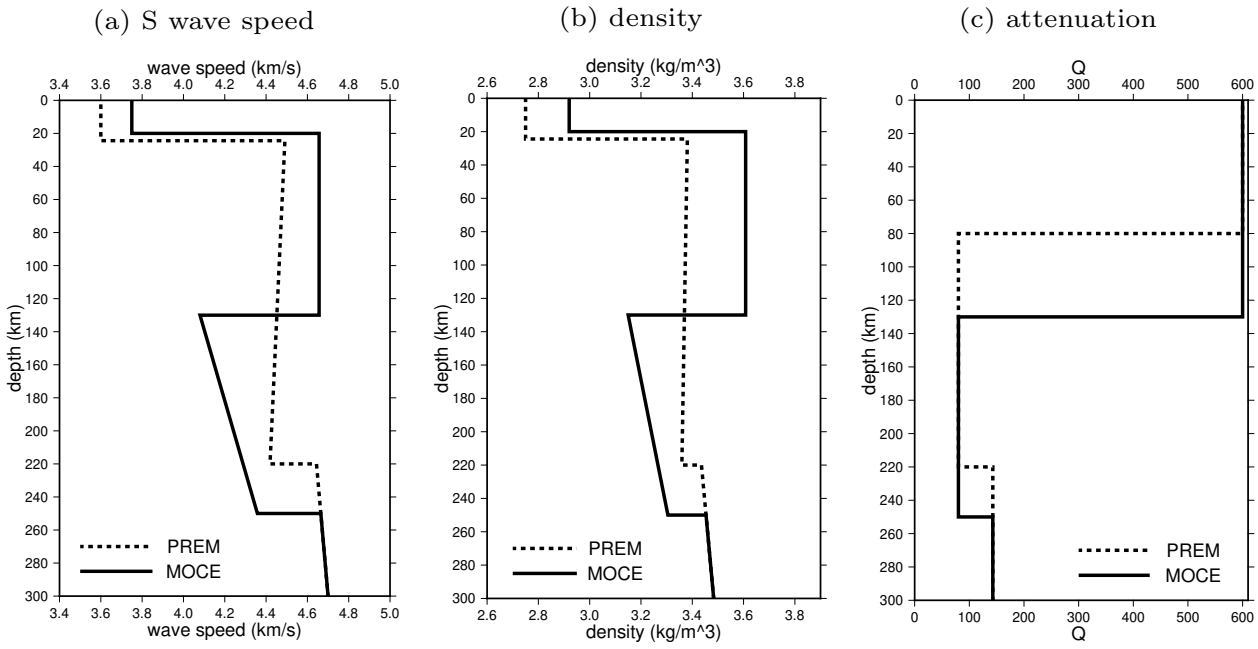

Figure B.2: **1-D reference earth model MOCE used in this study.** (a), S-wave speed profiles in model MOCE (solid black line) and model PREM (dotted black line). The velocity contrasts across the 220-km discontinuity and the LAB are 7% and 12%, respectively, in model MOCE. (b), density profiles of model MOCE and model PREM. (c), seismic Q profiles of model MOCE and model PREM.

(a) Traveltime (MOCE)

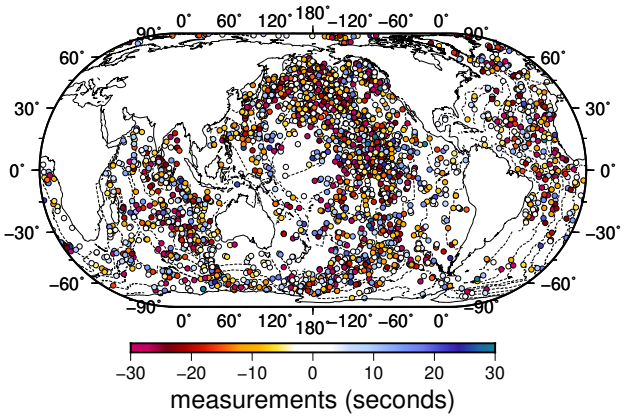

(b) Histogram (MOCE)

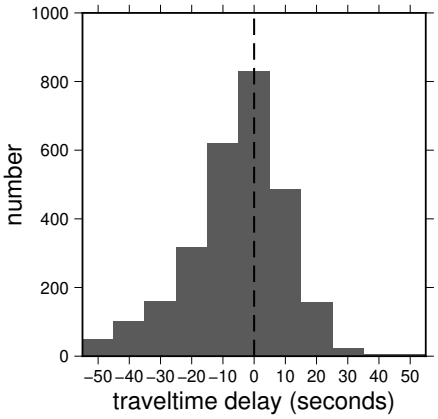

(c) Traveltime (PREM)

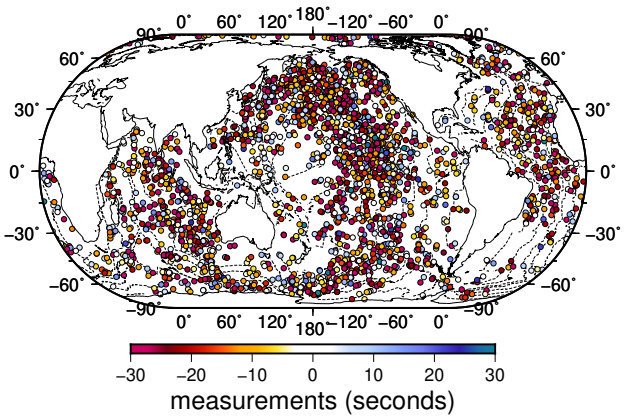

(d) Histogram (PREM)

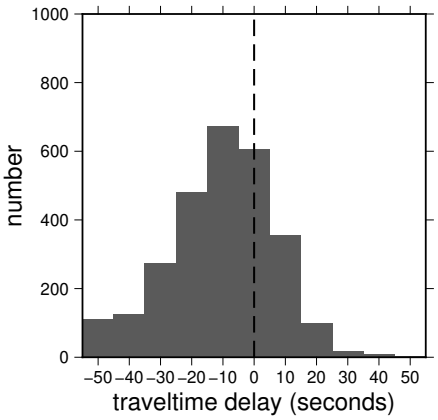

(e) 220 depth

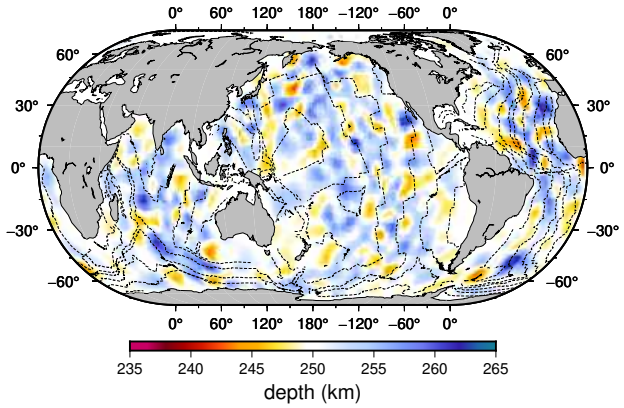

(f) 220 roughness

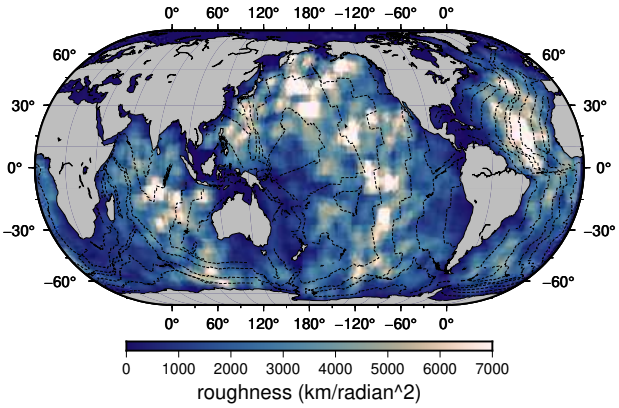

Figure B.3: (a) and (b), similar to Figure 3.2b and 3.2c, respectively, but are $\delta t|_{S_{220}S} - \delta t|_{SS}$ traveltimes of the 2754 data calculated for model MOCE before crustal and mantle wavespeed corrections plotted in mapview and histogram. (c) and (d), similar to Figure 3.2d and 3.2e, respectively, but are $\delta t|_{S_{220}S} - \delta t|_{SS}$ traveltimes of the 2754 data calculated for model PREM before crustal and mantle corrections. (e), similar to Figure 3.4a, but is 220-km depth before crustal and mantle corrections. (f), similar to Figure 3.5a, but is 220-km roughness before crustal and mantle wavespeed corrections.

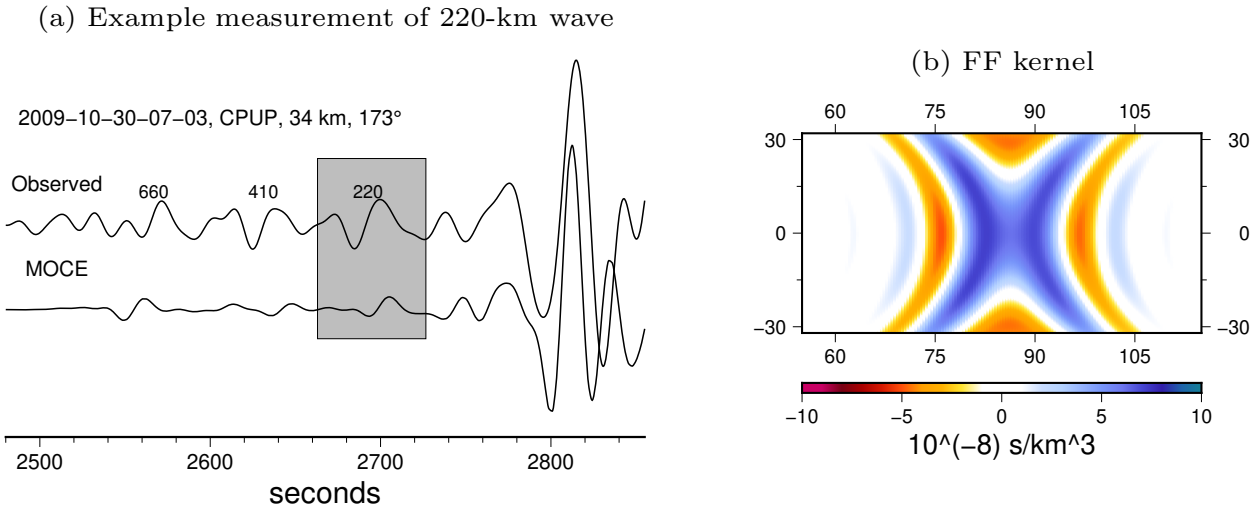

Figure B.4: **a**, example traveltime measurement of $\delta t|_{S_{220}S} - \delta t|_{SS}$ and the SS waves have been aligned. The shaded area indicates the measurement window of $\delta t|_{S_{220}S} - \delta t|_{SS}$. The observed seismogram was recorded at a GSN station CPUP (https://doi.org/10.7914/SN/GT) for a magnitude 6.8 earthquake in Japan in October 2009. The seismograms have been band-pass filtered between 10 and 80 mHz. The seismic event data/time, station, depth and epicentral distance is denoted above. **b**, finite-frequency traveltime boundary sensitivity kernel for the shaded measurement window in **a**.

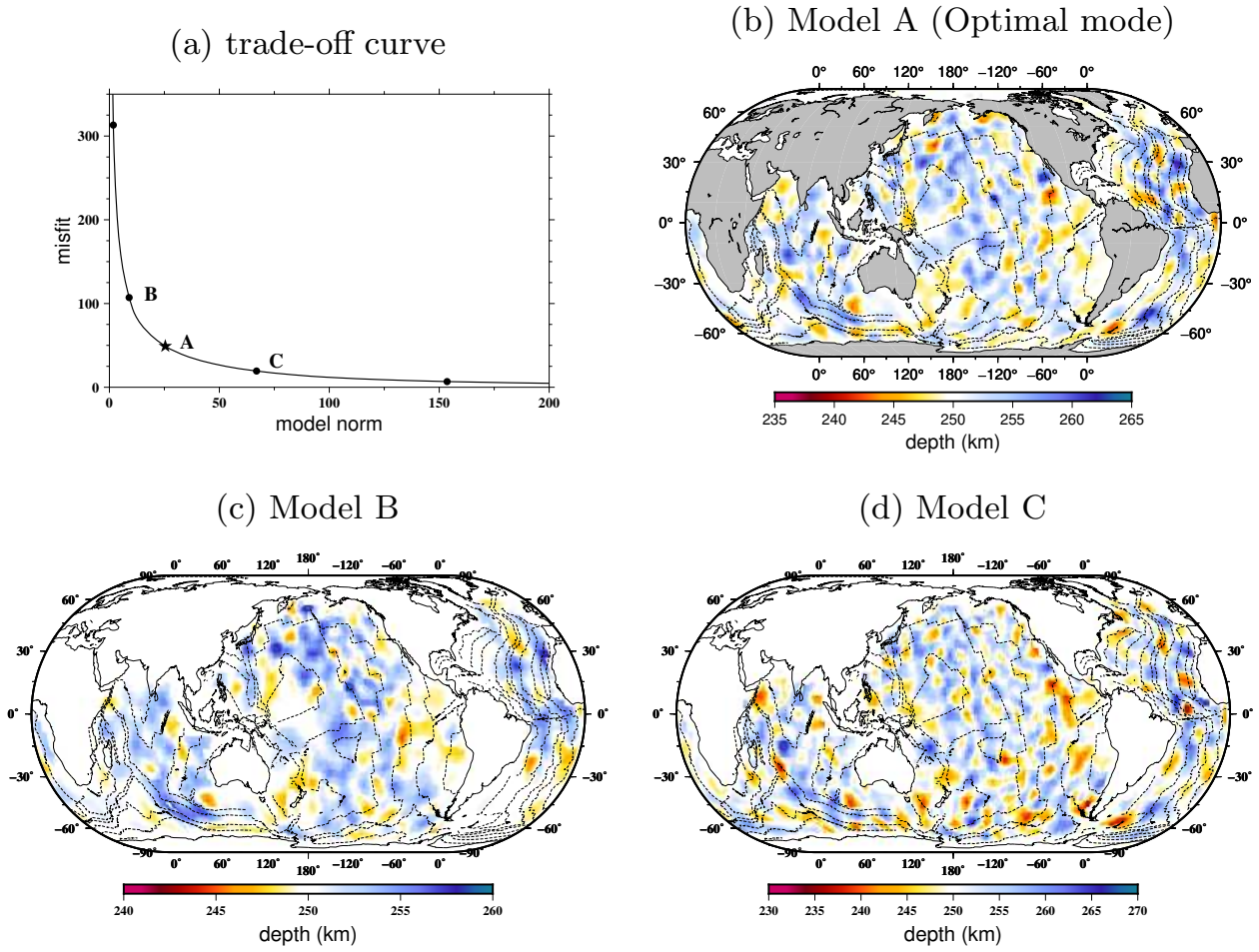

Figure B.5: (a), trade-off curve of TSVD solution to the inverse problem $\boldsymbol{Ax} = \boldsymbol{b}$ truncated to varying parameters k. The horizontal axis is $\|\boldsymbol{x}\|$ and the vertical axis is $\|\boldsymbol{A}^T\boldsymbol{Ax} - \boldsymbol{A}^T\boldsymbol{b}\|$. The optimal Model A plotted in (b) is obtained by using truncation parameter of 500, which is indicated by the star. TSVD solutions truncated to 100, 300, 700 and 900 are denoted by the black dots from left to right on the curve. Models truncated to 300 and 700 are labelled as Models B (c) and C (d), respectively. Insufficient eigenvectors are used in Model B which could not fully recover the 220-km depth structure, while excess eigenvectors are used in Model C which contains additional noise. Model A calculated using 500 eigenvectors best represents the depth structure of the 220-km discontinuity in the global oceans.

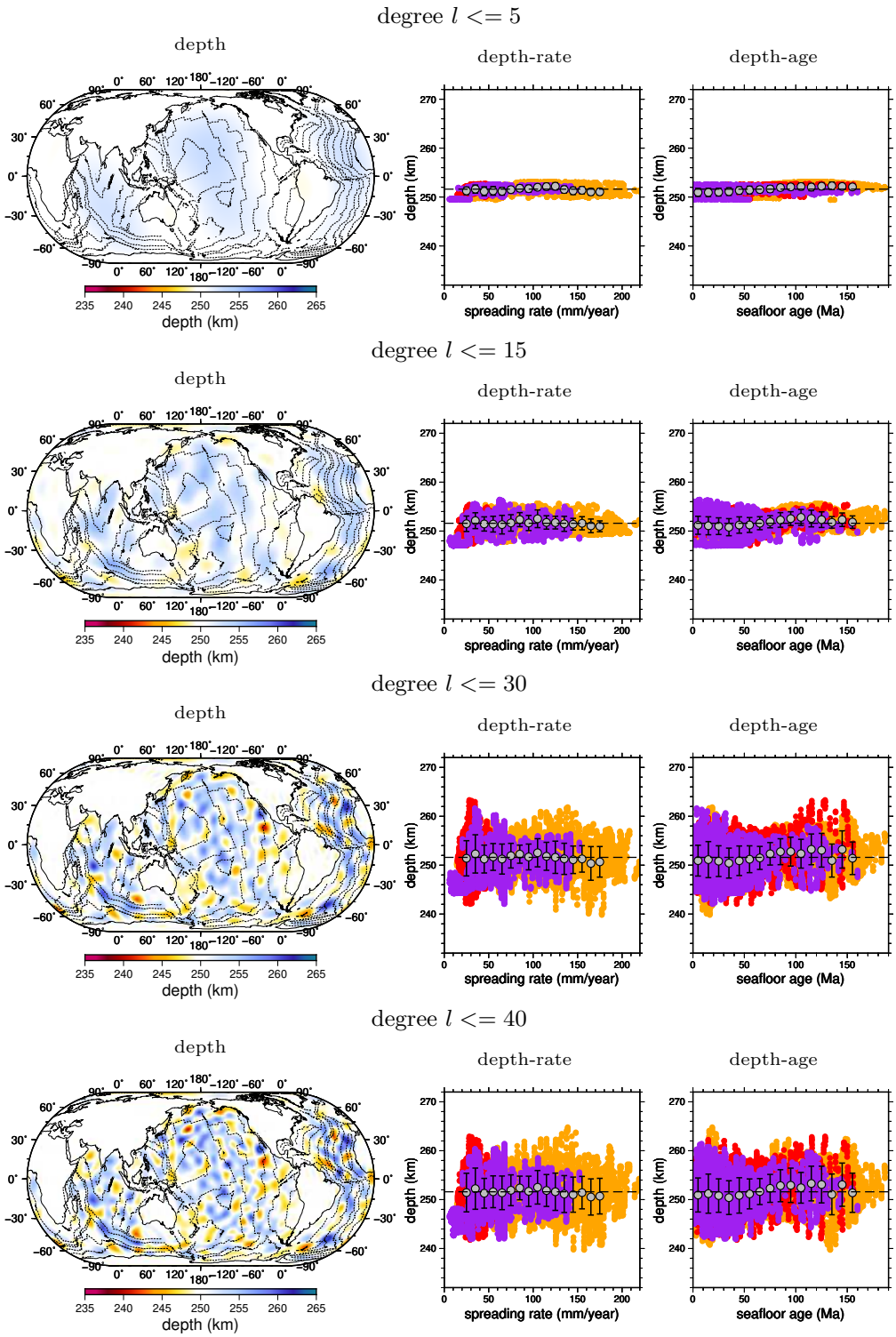

Figure B.6: **Correlation of 220-km depth filtered at different length scales with respect to seafloor spreading rate and seafloor age.** In top row, the left figure shows the 220-km depth filtered at degrees of 0-5. The middle figure, similar to Figure 4.4e, is the scatter plot of 220-km depth with respect to the seafloor spreading rate in all oceans (Pacific Ocean in orange, Atlantic Ocean in red and Indian Ocean in purple). Mean 220-km depth is plotted on the top in gray dots with one standard deviation. The right figure, similar to Figure 4.4f, is the scatter plot of 220-km depth and mean 220-km depth against the seafloor age in all oceans. The second, third and fourth rows are the same but for 220-km depth filtered at degrees of 0-15, 0-30 and 0-40, respectively. The 220-km depth at all length scales remains roughly constant at different seafloor spreading rates and seafloor ages.

(a) 220-km depth

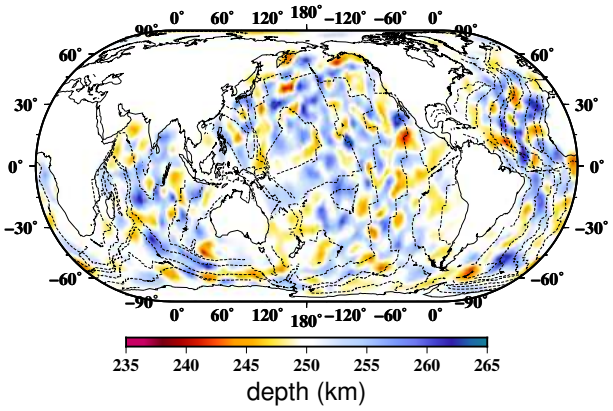

(b) model resolution

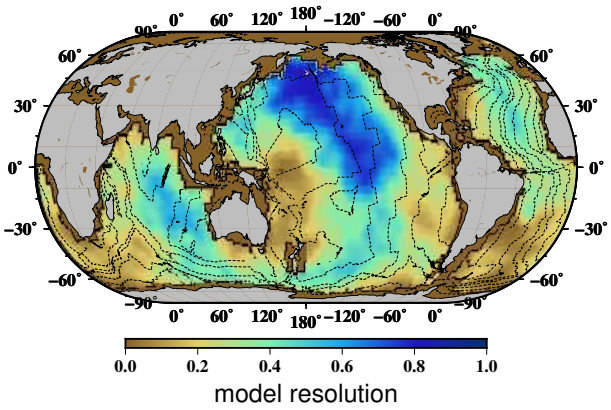

(c) 220-km depth (resolution>0.1)

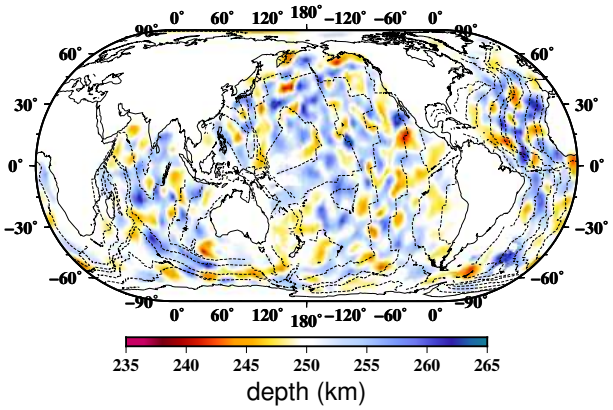

(d) 220-km depth (resolution>0.25)

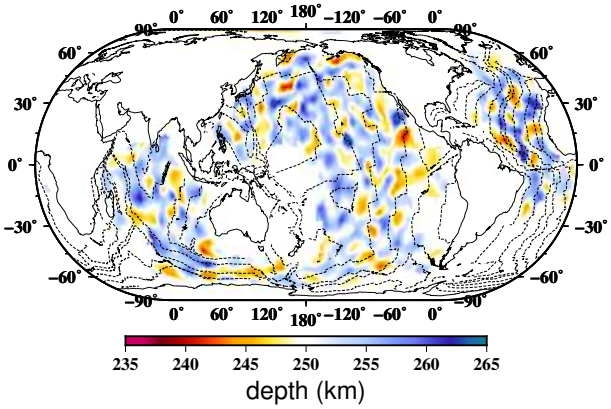

Figure B.7: (a), 220-km depth model in global oceans. (b), resolution of the 220-km depth model (a). The 220-km depth is well recovered in regions where the resolution is large. (c), 220-km depth model with resolution > 0.1. (c), 220-km depth model with resolution > 0.25.

(a) Atlantic roughness
(rate <= 40 $mm/year$ & resolution > 0.1)

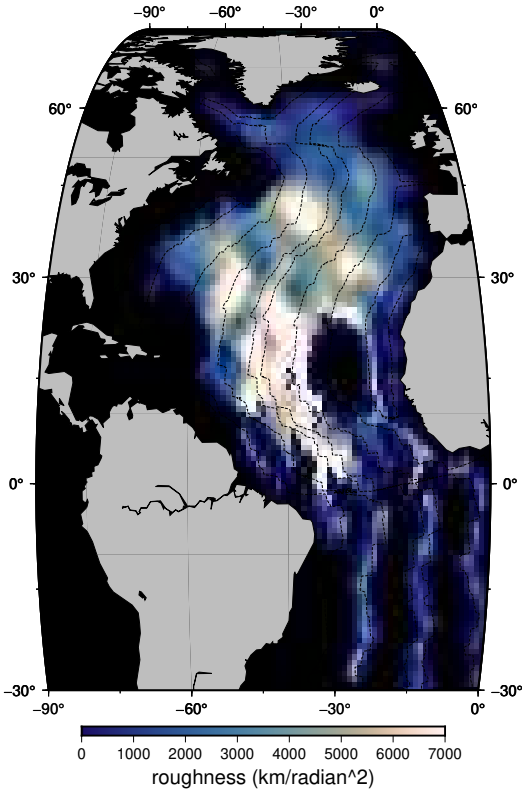

(b) Atlantic spreading rates
(rate <= 40 $mm/year$ & resolution > 0.1)

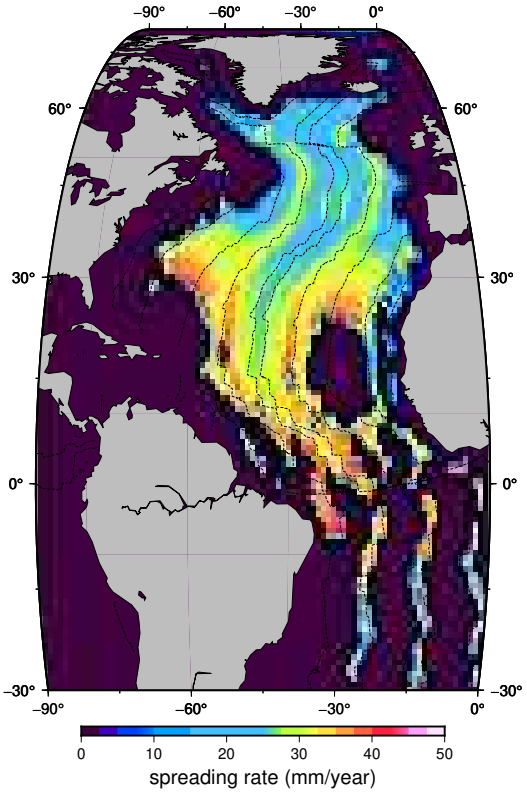

Figure B.8: (a), 220-km roughness in the Atlantic Ocean with spreading rate <= 40 mm/year and resolution > 0.1. (b) spreading rate <= 40 mm/year in the Atlantic Ocean with resolution > 0.1. There is a strong correlation between the 220-km roughness and spreading rate in the Atlantic Ocean. Specifically, roughness is generally small in North Atlantic where spreading rate is slow in general. In the middle Atlantic, roughness becomes large and the spreading rate turns fast.

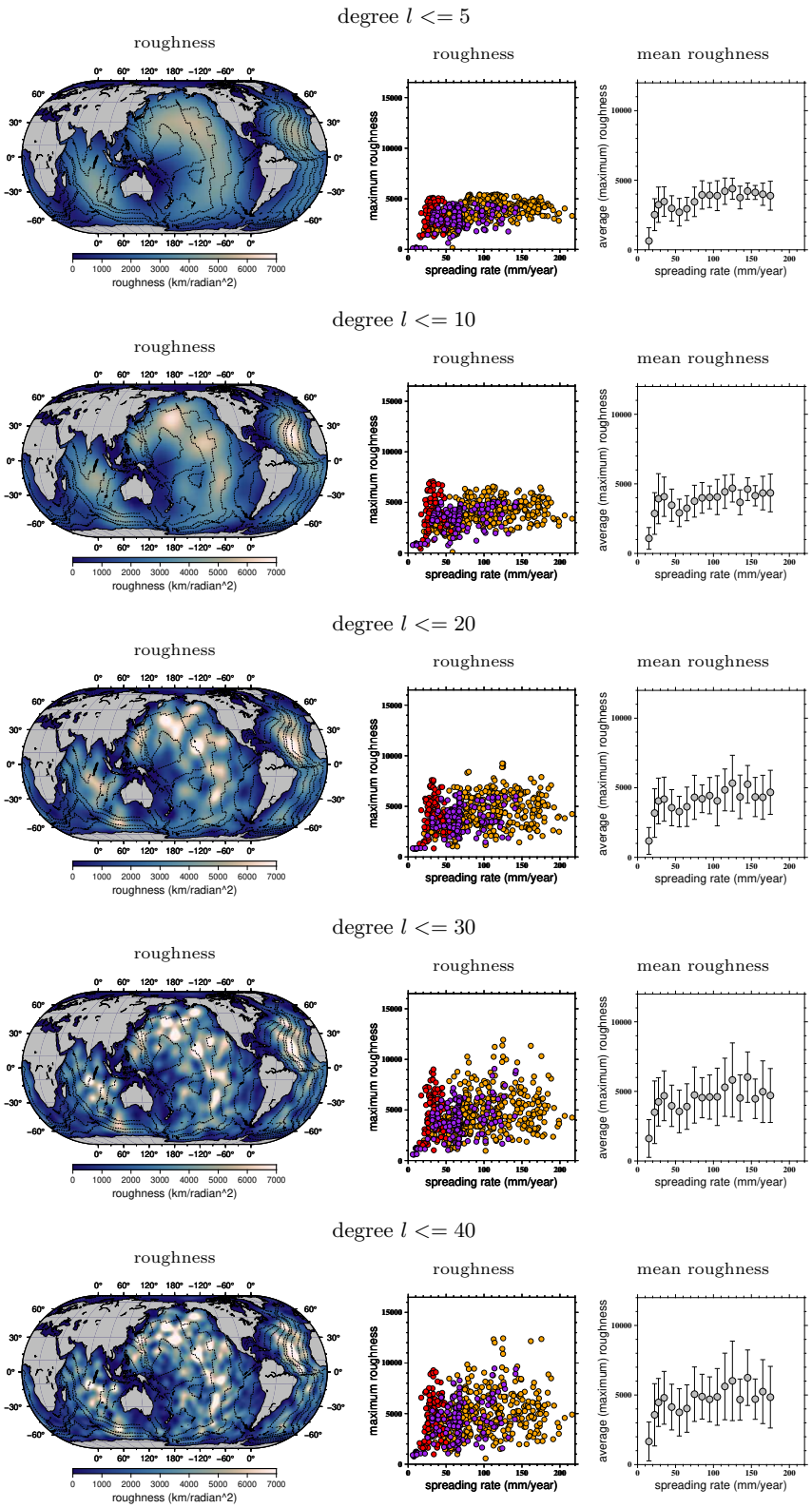

Figure B.9: **Correlation between 220-km roughness filtered at different length scales and seafloor spreading rate.** In top row, the left figure shows the 220-km roughness filtered at degrees of 0-5. The middle figure is the scatter plot of maximum 220-km roughness with respect to the seafloor spreading rate in $5° \times 5°$ degree cells in all oceans (Pacific Ocean in orange, Atlantic Ocean in red and Indian Ocean in purple), similar to Figure 5.5c. The right figure presents the scatter plot of mean (maximum) 220-km roughness against the seafloor spreading rate, similar to Figure 5.5d. The second, third, and fourth rows are the same but for 220-km roughness filtered at degrees of 0-15, 0-30 and 0-40, respectively. The positive correlation between 220-km roughness and seafloor spreading rate holds at different length scales.

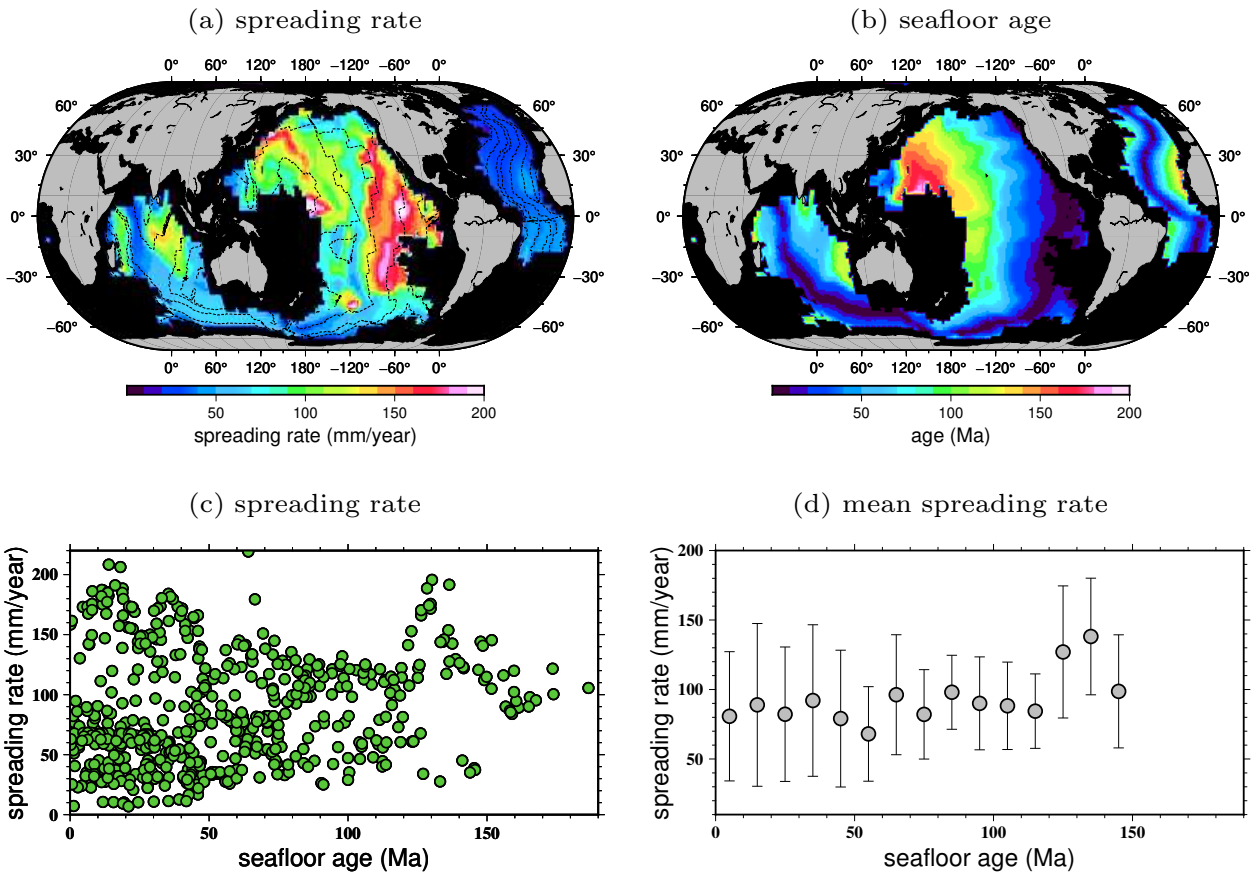

Figure B.10: **Correlation between seafloor spreading rate and seafloor age.** (a), seafloor spreading rate in oceanic regions with large resolution (> 0.25). (b), seafloor age in oceanic regions with large resolution (> 0.25). (c) and (d), scatter plot of maximum and mean (maximum) seafloor spreading rate with respect to the seafloor age in $5° \times 5°$ degree cells in global oceans. The mean (maximum) seafloor spreading rate is obtained by averaging the maximum seafloor spreading rate at seafloor age ranges of every 10 Ma. The seafloor spreading rate generally remains constant at different seafloor ages except at 120 - 150 Ma at which there are abnormally fast rates. This sharp increase in rate may reflect potential timescale miscalibration.

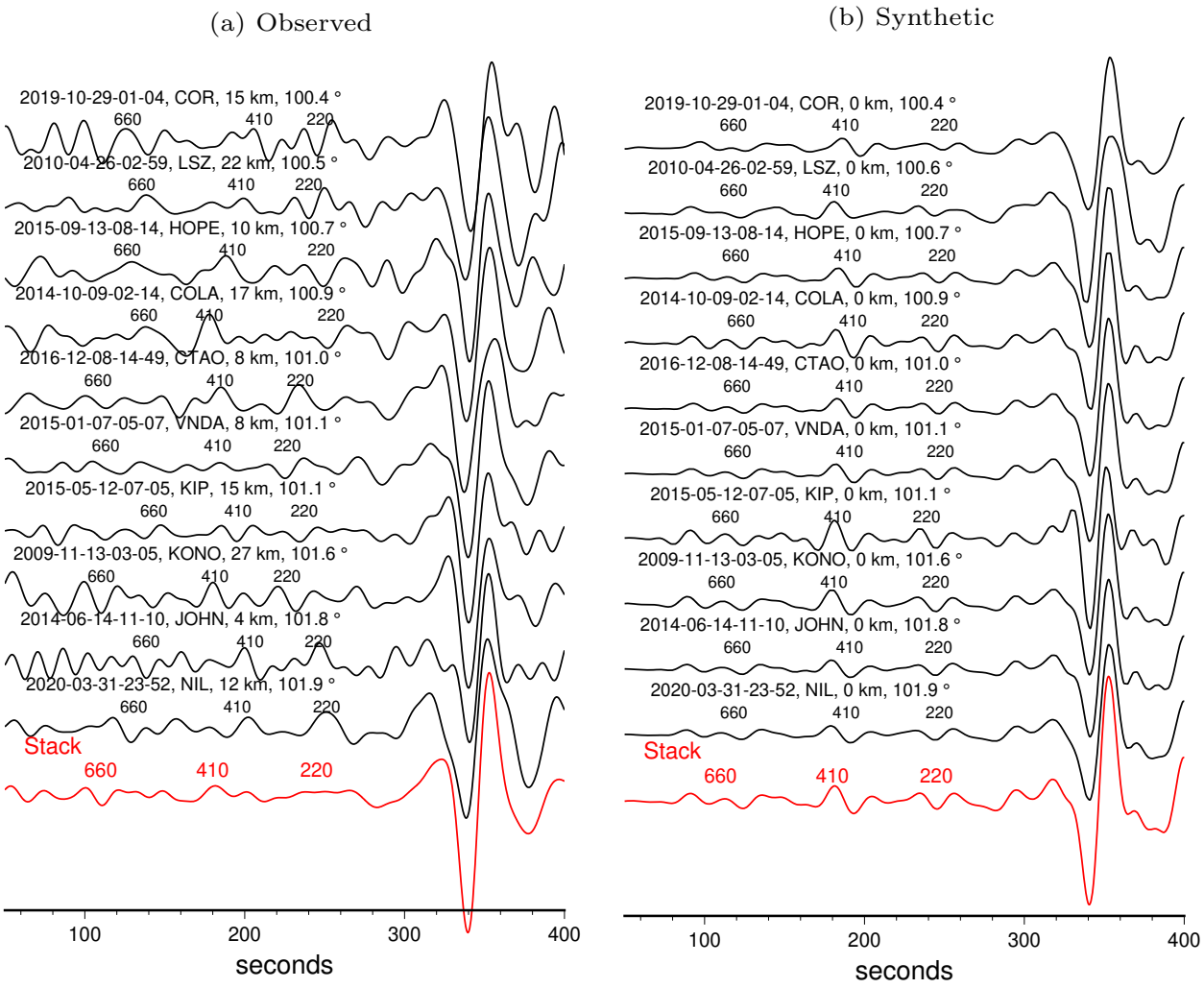

Figure B.11: **Stacking of observed seismograms shows weak 220-km signal.** **a** and **b**, example observed and synthetic seismograms with epicentral distance of 124-125 degrees. The synthetic seismograms are calculated in the reference model MOCE. The event date/time, station and depth are denoted above. 10 observed seismograms where clear 220-km waves can be observed in **a**. But they present large variations in arrival time and polarities. The corresponding synthetic seismograms calculated using Model MOCE are in **b**. **c**, stacking result of the observed seismograms in **a** (top, red seismogram) and the synthetic seismograms in **b** (bottom, black seismogram). The main SS waves are aligned and the polarities are corrected to be the same.The arrivals of SS precursors are labeled.

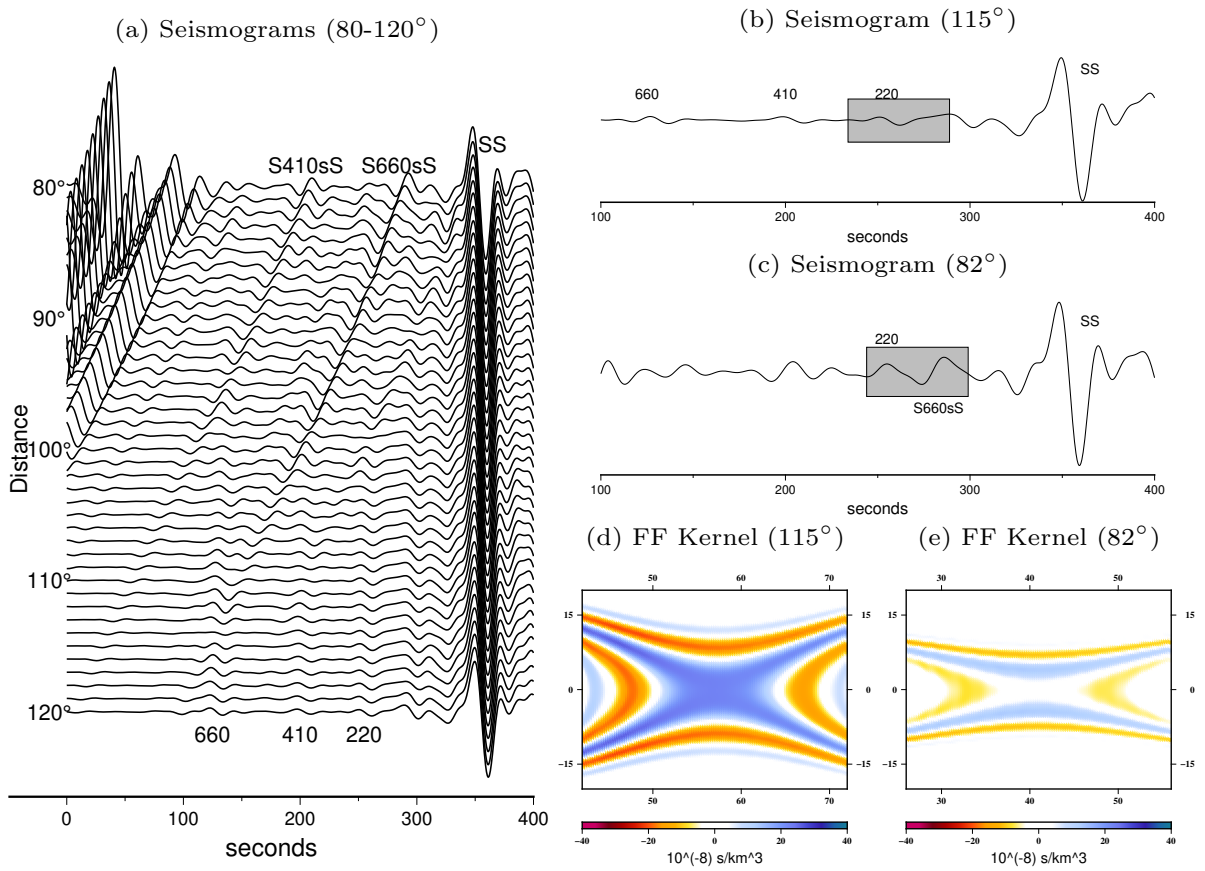

Figure B.12: Example traveltime sensitivity kernels of $S_{220}S$ with and without phase interference of $S_{660}sS$. (a) SS wavefield at epicentral distance 80° - 120° for a earthquake event source of 0 km. The SS waves are aligned. The arrivals of the SS precursors $S_{660}S$, $S_{410}S$ and $S_{220}S$ as well as two large-amplitude phases $S410sS$ and $S660sS$ are labeled. $S660sS$ wave strongly interfere with $S_{220}S$ when epicentral distance is smaller than $\sim 90°$. (b) and (c) are the zoom in views of the seismogram at 115° and 82°, respectively , from (a). The kernel measurement windows (shaded) are centered at the expected arrival of the $S_{220}S$ waves. There is no phase interference for $S_{220}S$ wave at epicentral distance of 115° while a strong $S660sS$ wave arrives about the same time as the $S_{220}S$ wave at 82°. As a result, the calculated sensitivity kernel values under the impact of $S660sS$ wave for 82° (e) are abnormal which are an order of magnitude smaller than that for 115° (d). The strong $S660sS$ wave is dominating in the expected arrival time window of $S_{220}S$. This phase is not reflected at the 220-km discontinuity and therefore it has no sensitivity to depth perturbations of the 220-km discontinuity at the reflection point.

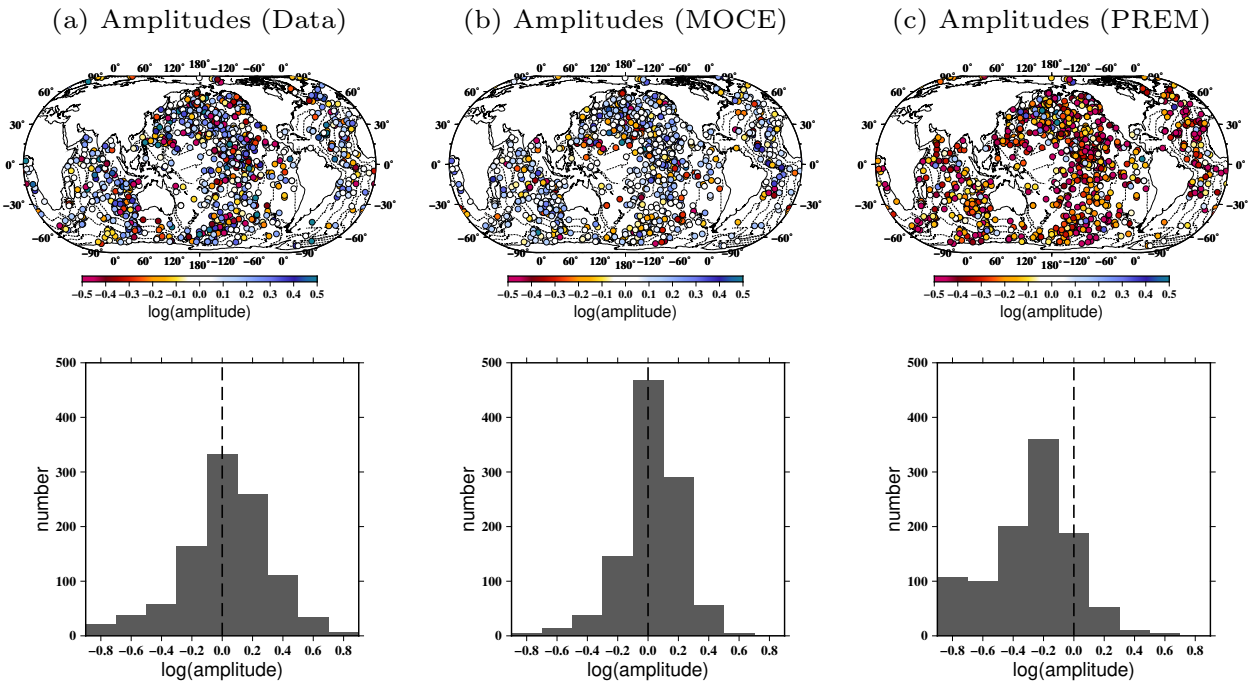

Figure B.13: **Amplitude measurements of $S_{LAB}S$ waves.** Similar to Figure 3.3, but for the amplitude measurements of 1021 sets of $S_{LAB}S$ waves in data, model MOCE and model PREM calculated as γ= minimum $[\log(A_{S_{\mathrm{LAB}}S}/A_{S_{410}S}), \log(A_{S_{\mathrm{LAB}}S}/A_{S_{660}S})]$ plotted in mapviews and histograms.

Appendix C

Supplementary Figures Used in Chapter 4

This chapter contains 1 supplementary figures used in Chapter 4.

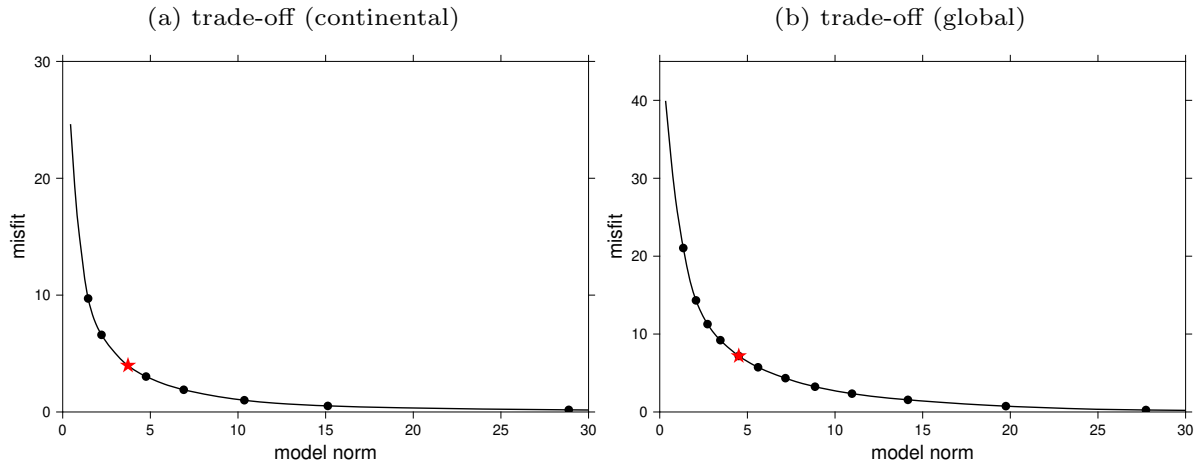

Figure C.1: (a) trade-off curve of finite-frequency tomography using continental $S_{220}S$ measurements only. The horizontal axis is model norm $\|\boldsymbol{m}\|$ and the vertical axis is data misfit $\|\boldsymbol{G}^T\boldsymbol{G}\boldsymbol{m} - \boldsymbol{G}^T\boldsymbol{d}\|$. Dots are models obtained using different regularization parameter N and the red star denotes the optimal solution. (b) trade-off curve of finite-frequency global tomography using both the continental and oceanic $S_{220}S$ measurements.